![KIT – Karlsruhe Institute of Technology]

Measurement of the Production of Boron from the Fragmentation of Cosmic Ray Carbon with NA61/SHINE

Zur Erlangung des akademischen Grades eines

Doktors der Naturwissenschaften (Dr. rer. nat)

von der KIT-Fakultät für Physik des Karlsruher Instituts für Technologie (KIT)

genehmigte

Dissertation

von

Dr. rer. nat. Neeraj Amin

aus Mumbai, Indien

Tag der mündlichen Prüfung:	21/06/2024
Referent:	Prof. Dr. Ralph Engel
Korreferent:	Prof. Dr. Ulrich Husemann
Betreuer:	Dr. Michael Unger

I declare that I have developed and written the enclosed thesis completely by myself, and have not used sources or means without declaration in the text.

KARLSRUHE, 17/05/2024

. . . .

Neeraj Amin

Acknowledgement

Although it may appear to be an individual endeavor, the completion of this singular job would be incomplete without acknowledging the efforts of those around me, as I worked on the monolithic project that is my PhD. My experience at the Institute for Astroparticle Physics at the Karlsruhe Institute of Technology was truly invaluable. I extend my sincerest gratitude to Prof. Dr. Ralph Engel for offering me the opportunity to delve into such an interesting and unique topic of measuring nuclear fragmentation cross sections. Additionally, I am thankful to Prof. Ulrich Husemann for permitting me to collaborate with him on a short-term project, which served as a crucial bridge for my research, and gladly accepting the role as my second referee.

I offer my deepest thanks to my supervisor, Dr. Michael Unger, for his invaluable suggestions, efficient assistance, and expert guidance at every stage of my thesis. His profound knowledge across scientific domains, coupled with his insatiable curiosity and engaging discussions, greatly enriched my analytical insights. I aspire to embody these qualities in my own scientific pursuits. Furthermore, I extend my appreciation to Dr. Darko Veberic for meticulously proofreading my documents and offering insightful suggestions. My heartfelt regards go out to everyone at IAP for consistently making me feel welcome, especially Olena, for her prompt help with administration-related information.

My time at CERN, in pursuit of my research, was a fortunate opportunity during which I had the pleasure of meeting remarkable individuals from the NA61 collaboration. I extend my gratitude to the esteemed "bloody knucklers," Brant Rumberger, Simona Ilieva, and Antoni Marcinek, for their invaluable assistance in navigating the intricacies of the NA61 experimental facility, software, and the CERN environment as a whole, particularly during hardware shifts. The camaraderie fostered during our time together transformed shifts into enjoyable experiences with regular game and wine nights.

Throughout my journey as a PhD student, my friends in Karlsruhe have been an unwavering source of support. I extend my deepest gratitude to my chosen family, Mrunal

Abstract

This thesis discusses the measurement of the production cross sections of nuclear fragments in carbon-proton interactions at $13.5A$ GeV/c momentum, using data from a pilot run conducted in 2018 at the NA61/SHINE facility at CERN. Cross section measurements with improved uncertainties are key inputs for accurately predicting secondary-to-primary cosmic ray flux ratios, and determining their propagation characteristics in the Galaxy. In this study, the mass-changing, charge-changing, and isotope production cross sections of the ^{11}B, ^{10}B, and ^{11}C nuclei from fragmentation of ^{12}C have been measured. Two targets, namely polyethylene and graphite, are used to derive the cross section on protons. The primary outcome is the total boron production cross section on the proton target $\sigma^{\text{tot.B}} = (77 \pm 5)$ mb. It aligns closely with previous studies and theoretical predictions achieving a significant reduction in the measured uncertainty compared to prior measurements. Furthermore, this thesis validates the feasibility of measuring low mass fragments at NA61/SHINE. The recent hardware upgrade of the detector electronics have enhanced data acquisition rates. With these improvements and the analysis techniques developed in this thesis, a future high-statistics data taking with NA61/SHINE will be able to provide the precise cross sections needed to exploit the full potential of the recent data from space-based cosmic ray experiments.

Contents

Contents

1. Introduction

The study of extra-terrestrial high energy radiation has been a matter of interest for more than a century, beginning with the discovery of charged particles called cosmic rays (CR), by Viktor Hess in 1912. They are primarily composed of protons and helium nuclei, with small abundances of heavier nuclei from lithium up to iron, and beyond. The measured flux of these particles covers a wide range of energies from a few MeV up to as high as hundreds of EeV. Various theories have been put forth explaining the Galactic and extra-galactic origin of cosmic rays, nevertheless the exact nature of the astrophysical sources and the physical processes responsible for accelerating cosmic rays to high and ultrahigh energies is still an open question. An important piece of the puzzle for Galactic cosmic rays is the understanding of their propagation in the Galaxy.

Galactic cosmic rays can be categorized as primary and secondary, based on their point of origin. The primary cosmic ray nuclei are accelerated in the source regions (e.g. p, He, C, N, O, Fe), whereas the secondary nuclei are a product of the nuclear interactions of the primary species with the protons and helium of the interstellar medium (e.g. e^+, $\bar{p}$, Li, Be, B, F). Two key requirements for modeling the propagation of Galactic cosmic rays are the secondary-to-primary flux ratios arriving at Earth and the corresponding nuclear fragmentation cross sections. Secondary-to-primary flux ratios are important parameters to determine astrophysical quantities such as the amount of traversed material referred to as the grammage, the size of the Galactic halo, and the diffusion coefficient. Recent measurements by space-based cosmic ray detectors, like PAMELA, AMS-02, CALET and DAMPE provide flux values with unprecedented precision, with uncertainties reaching levels of a few percent. On the other hand, the current uncertainties on the measurements of nuclear fragmentation cross sections are at $\sim 20\%$. Regrettably, these uncertainties propagate directly to the prediction of secondary CR fluxes and dominate the uncertainties in the CR propagation models. Furthermore, cross section uncertainties also induce equivalently large uncertainties in the flux prediction of astrophysical anti-matter, which

constitute an important background in the searches for products of astrophysical dark matter annihilation in the Galaxy. In addition, since fluorine is assumed to be mostly of secondary origin, recent excesses as measured in the F/Si and Li/C flux ratio by AMS-02 suggest a primary component of the two elements. The interpretation of these discrepancies is difficult, since they are at the same level as the uncertainties related to the cross sections.

Therefore, it it crucial to measure fragmentation cross sections of specific reactions with a level of precision equivalent to the measured CR fluxes. It is theoretically expected that nuclear fragmentation cross sections above energies $10A\,\text{GeV}/c$ reach asymptotic energy, independent values. Therefore, precise cross section measurements performed in this energy range can improve the precision of modeling Galactic CR propagation for the full energy range relevant to the recent satellite measurements of CR fluxes.

Out of all the possible light secondary nuclei produced in the Galaxy, the most studied flux ratio is the that of boron to carbon (B/C). The B/C flux ratio is an extensively used observable to determine the total column depth of matter density traversed by the cosmic rays. Cosmic boron is produced in spallation reactions of the primary cosmic ray nuclei like C, N and O interacting mainly with interstellar hydrogen. Moreover, the spallation of primary cosmic ray nuclei also produces short-lived radionuclides, like ^{11}C, which decays to the stable ^{11}B via β^+ decay with a half-life of ~20 min, and adds to the total boron (^{10}B+^{11}B) production in the galaxy.

The aim of this thesis is the measurement of the direct and indirect production of boron fragments in carbon-proton interactions at a beam momentum of $13.5A\,\text{GeV}/c$. The data was collected in a pilot run performed in 2018 at the NA61/SHINE facility at CERN with a ^{12}C beam and two targets namely polyethylene and graphite. In the following, an introduction to Galactic cosmic rays and their propagation, the abrasion-ablation model of nuclear fragmentation, and quantitative reasoning for the need to measure precise nuclear fragmentation is given in Ch. 2. The experimental setup of the NA61/SHINE facility, including the description of the detectors, and the recent hardware upgrade is described in Ch. 3. The details of the pilot run, with the production of ^{12}C beam, trigger settings, and target parameters are given in Ch. 4. Quality cuts pertaining to data selection and the actual measurement are described in Ch. 5. The mathematical formalism used and developed for this analysis is given in Ch. 6. It also addresses the corrections and systematic uncertainties of the measurement. Finally, the cross section results are summarized in Ch. 7,

with concluding statements and an outlook of possible future fragmentation measurements as given in Ch. 8.

2. Galactic Cosmic Rays and their Interactions

Since the discovery of cosmic rays, advancements in detection techniques, including ground-based observatories and satellite missions, have enabled scientists to map out the energy distribution of cosmic rays across a large range of energies, from 10^7 eV to ultra-high energies exceeding 10^{20} eV. Cosmic ray fluxes measured recently up to TeV energies by various space based particle detectors such as PAMELA [1], AMS-02 [2], DAMPE [3], CALET [4], ACE-CRIS [5] provide a wealth of precise CR data with flux uncertainties < 5%. In this chapter, we start with a discussion on the measured the all-particle energy spectrum of cosmic rays and a comparison of the elemental composition in the solar system and in cosmic rays. Next, we give a description of the two well-known mechanisms to accelerate cosmic rays to high energy. The transport equation pertaining to the propagation of cosmic rays with implications of the secondary-to-primary flux ratios is discussed in details. Following which, an overview of the abrasion-ablation model to explain nuclear fragmentation in heavy ion reactions is discussed, finally motivating the need to measure boron production cross sections to understand CR propagation in the Galaxy.

2.1. Cosmic Ray Spectrum

The energy spectrum of cosmic rays provides insights into the processes governing particle acceleration, propagation, and interactions within astrophysical environments. The energy spectrum of cosmic rays follows a power-law distribution, characterized by a rapid decrease in particle flux with increasing energy,

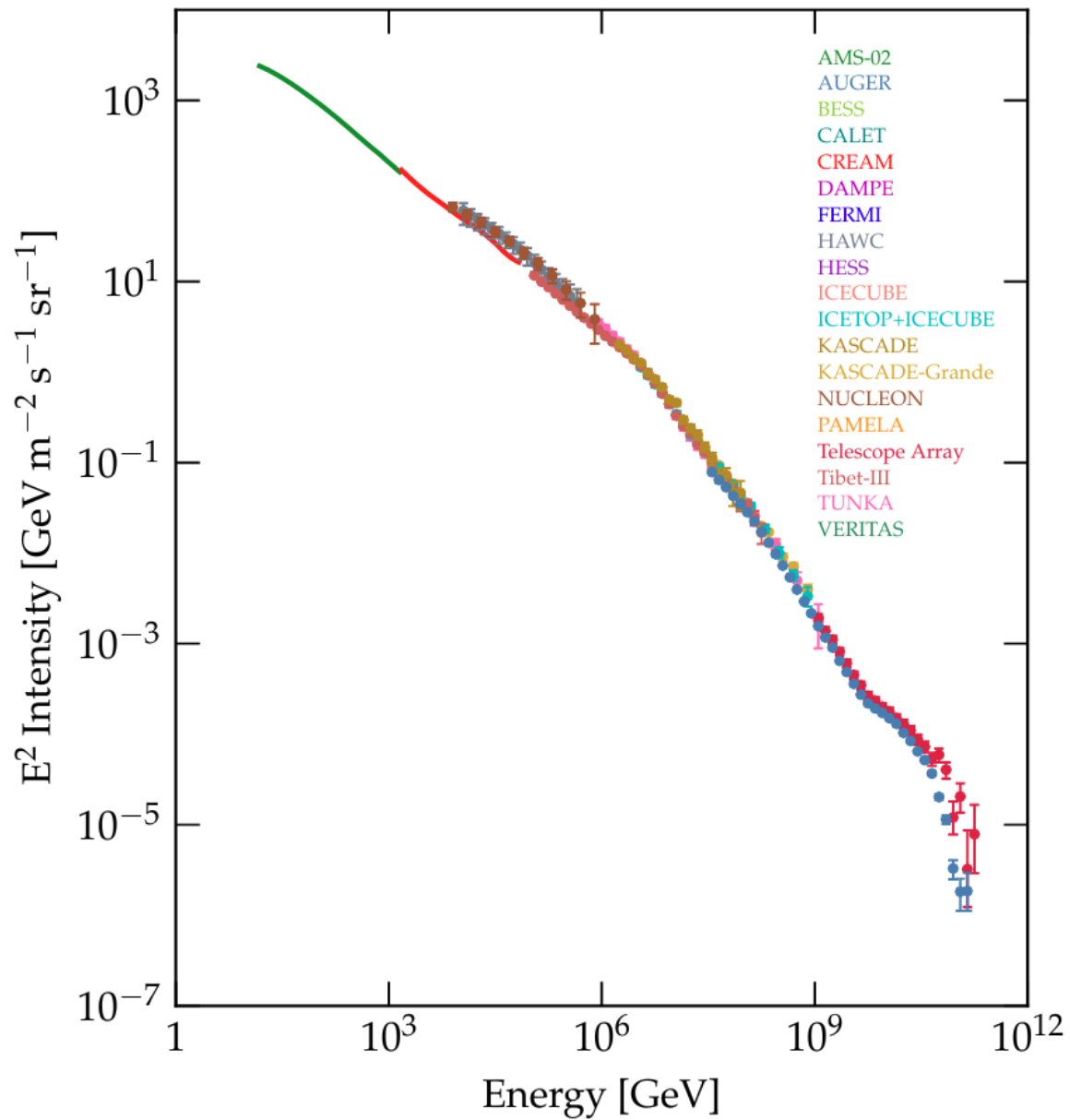$$\frac{\mathrm{d}N}{\mathrm{d}E} \propto E^{-\gamma}, \tag{2.1}$$

Figure 2.1.: Spectrum of cosmic rays as measured by the enlisted experiments (adapted by [6] from [7]).

The all-particle cosmic-ray spectrum as measured at Earth by the various ground-based, balloon borne, and space-based experiments, is shown in Fig. 2.1. Empirical observations reveal an overall spectral index in the range of $2.7 \leqslant \gamma \leqslant 3.1$, in the energy range spanning from approximately 10^9 eV up to 10^{15} eV. Cosmic rays below 10 GeV entering the solar system encounter a magnetized plasma called the solar wind. The plasma generates turbulent magnetic field, changing the energy and trajectory of cosmic rays suppressing their flux at low energies. Three major features have been observed in spectrum that deviate from the simple power-law. The first feature is a steeping of the spectrum from $\gamma \approx 2.7$ to $\gamma \approx 3.1$ at $E \approx 3 \times 10^{15}$ eV called the "knee" [8].

There is evidence indicating a change in the chemical composition of cosmic rays around the knee region, where heavier particles are observed to dominate the composition region at energies up to $E \approx 10^{17}$ eV [9, 10]. With increasing energies above 10^{18} eV, the steeper spectrum flattens back again to $\gamma \approx 2.7$, adding a new aspect to the spectrum, called the "ankle" [11–13]. Energy range spanning from the knee to the ankle, marks an important transition region for origin of cosmic rays from Galactic to extra-galactic sources. Additionally, the knee may be associated with the onset of limitations imposed by the confinement and escape mechanisms governing cosmic ray propagation within the Galaxy. One of the most compelling and extensively researched explanations for the emergence of the knee is grounded in the maximum energy attainable through diffusive shock acceleration within supernova remnants. This process is widely regarded as the primary mechanism for accelerating Galactic cosmic rays [14].

Finally, a sharp cutoff in the spectrum is observed at $E \geqslant 5 \times 10^{19}$ eV [12, 15], resulting in a change of the spectral index from $\gamma \approx 3.3$ to $\gamma \approx 2.6$ above the ankle energy [13]. This theoretical upper limit was discovered independently in the works of K. Greisen [16], and G. Zatsepin and V. Kuzmin [17] for propagation of ultrahigh energy cosmic protons of extraGalactic origin. In the rest frame of the cosmic protons, the energy of $\gamma_{CMB} \approx 200$ meV, exceeding the threshold for pion production through Δ resonance The charged and neutral pions further decay into high-energy leptons (positrons and neutrinos) and photons respectively. For heavier CR nuclei, the energy threshold for photo-disintegration by γ_{CMB} with an average energy per photon of ~ 10 meV, is $E \approx 10^{18}$ eV, thereby exciting the giant dipole resonance. In this case too, the mean free path for thee $\gamma - p$ interactions is $O(2)$ kpc, much less than the size of the Galaxy.
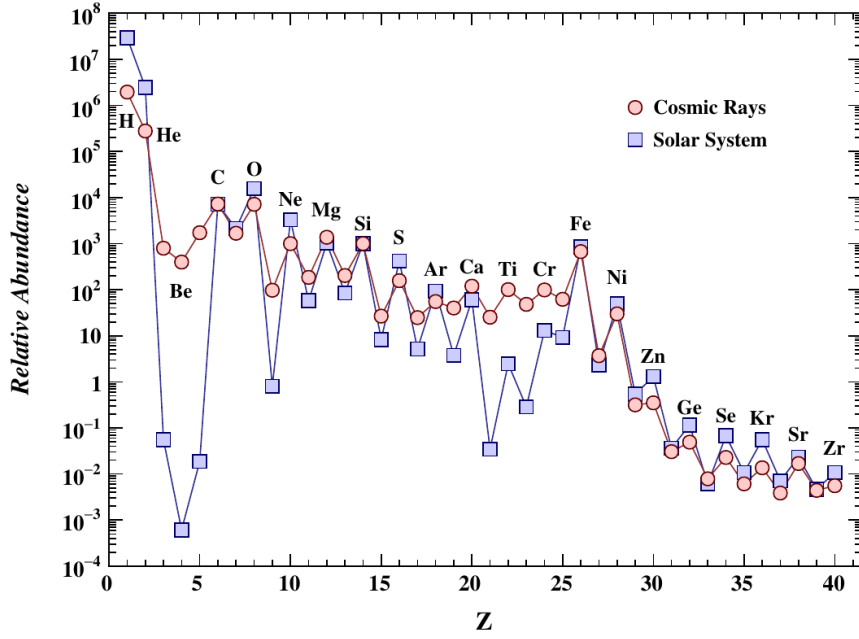
Figure 2.2.: Relative elemental abundance of cosmic rays and the solar system, normalized to Si=10^3. Data is from Refs. [18–23]. Figure is taken from Ref. [24].

2.2. Chemical Composition of CR Flux

Measurements reveal that cosmic rays consists of 98% hadrons and 2% electrons and photons. The hadronic component is dominated by the protons (~89%) and helium nuclei (~ 10%), with a trace amount of contribution from the heavier elements (~ 1%). The heavier elements mainly include the nuclei carbon, nitrogen, oxygen (collectively called CNO), silicon and iron, produced in the stellar nucleosynthesis processes. The relative elemental abundance of cosmic radiation compared to that of the solar system is shown in Fig. 2.2.

A strong correlation is seen between the two distributions for most of the elements, indicating that cosmic ray sources are capable of nucleosynthesis. Apart from the obvious discrepancy for underabundance of cosmic hydrogen and helium, (further discussed in Ref. [25]), there are clear deviations as seen particularly for two groups of elements. The first is the light group Li, Be and B, and the second is the heavier group consisting of sub-Fe elements like Sc, Ti, V, Cr and Mn. These two groups have much larger abundance in cosmic rays than in the solar system, suggesting that their origin lies in the propagation medium than the source. They are products of the nuclear fragmentation reactions of their progenitors, which is the CNO group for the Li, Be and B, and Fe for the elements

in the second group. Therefore, cosmic rays can be grouped into two species based on their point of origin, namely the primary and the secondary cosmic rays (see Sec. 2.4 for further details.) Therefore, to extract information about the origin of the measured cosmic ray spectra for various elements, it is crucial to understand the propagation of cosmic rays in the Galaxy, and will be discussed in the next section.

2.3. Propagation and Acceleration of Galactic Cosmic Rays

It is evidently clear from the CR energy spectrum that its source is not a thermal distribution of hot gas, and requires a powerful physical process to accelerate cosmic rays to such high energies. This section gives an overview of the different acceleration mechanisms and the transport of CR nuclei in the galaxy.

2.3.1. Acceleration Mechanisms

The origin of the power law energy spectrum of cosmic radiation is in the physical processes that CR particles are accelerated to such high energies. For an astrophysical object to be considered as a possible CR source supporting powerful accelerating mechanisms such that it can reproduce the CR spectrum, it has to satisfy the a few constraints such as the following [26]:

1. The accelerated particle is contained in the source volume during acceleration.

2. The source posses the required power to accelerate the particles to maintain the observed energy density.

3. Radiation loss by particle should not exceed its gain in energy.

4. Energy loss in interactions should not exceed the gain in energy by the particle

Magnetic fields are key in understanding the propagation and acceleration of cosmic rays to high energies. It also sets a limit on the maximum energy obtained by CR particles in the acceleration sites. A particle of charge Z and energy E moving orthogonal to a magnetic field B will deflect in a circular path of radius r_{L}. It is called gyroradius or the Larmor radius and is the ratio of the rigidity $R = p/Z$, where p is the momentum of the
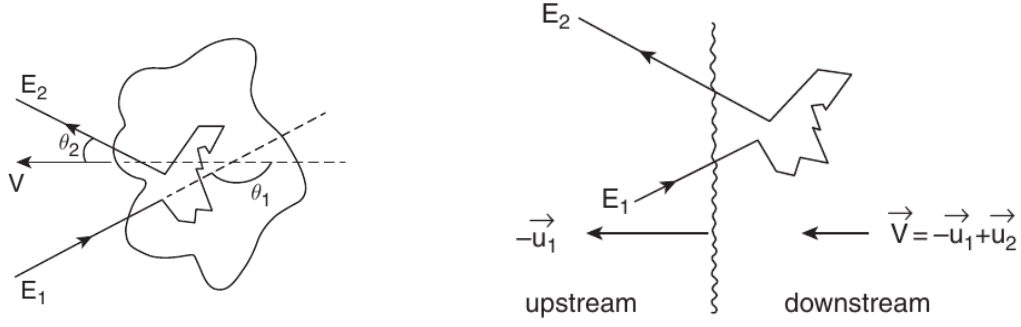
Figure 2.3.: Illustrations of the second-order (left) and first-order Fermi acceleration mechanisms, adopted from [28]. E_1 and E_2 are the energies of the particle before (upstream) and after entering (downstream) the plasma (shock).

particle, to the magnetic field as, $r_L = R/B \approx E/(ZB)$[1]. For an acceleration region of size D, if $r_L > D$, then the particle escapes from the region. This condition sets the maximum attainable energy by the particle, and is given by,

$$E_{\text{max}} = ZRB = 10^{18} Z \left(\frac{D}{\text{kpc}} \right) \left(\frac{B}{\mu G} \right) \text{ eV}. \tag{2.2}$$

where the size of accelerator is measured in kiloparsec (kpc) and the magnetic field in μG. This relation is slightly altered by a factor β_S when taking into account the velocity of the shock front accelerating the particles (see Sec. 2.3.1.2 below), which then leads to the well known Hillas criterion [27]. It can be used to identify and classify various astrophysical sources as CR accelerators. In the standard paradigm of Galactic cosmic rays, the sources are SNRs as they full all the conditions. In the following subsections, two well known mechanisms for accelerating CR particles to relativistic energies are described.

2.3.1.1. Second Order Fermi Acceleration

The idea that cosmic rays are primarily accelerated due to their interactions with randomly moving magnetized clouds was first put forth in the works of E. Fermi [29]. In this process, the particles entering the plasma clouds reflect on its inhomogenous magnetic field, changing it final energy. It was shown that multiple stochastic interactions with the clouds will increase the energy of the incident particle, resulting in a power law energy

---

[1]Since the total energy of a particle $E = \sqrt{p^2 + m^2}$, where m is its rest mass. For a relativistic particle $p \gg m$,therefore $E \approx p$.

spectrum. A particle starting with initial energy E_0, undergoing n interactions, will have the final energy, given by,

$$E_n = E_0 \left(1 + \epsilon\right)^n,\tag{2.3}$$

where $\epsilon = \Delta E/E$ is the fractional gain in energy per interaction. For a magnetic cloud moving with a velocity $V = \beta c$, the fractional gain in energy is given by,

$$\epsilon = \frac{\Delta E}{E} \approx \frac{4}{3}\beta^2.\tag{2.4}$$

Since the energy gain is proportional to square of β, it is called second-order Fermi acceleration. Since cloud velocities are typically $10 - 15\,\text{km/s}$ ($\beta < 1 \implies \beta \ll 1$). Therefore, the rise in energy is very slow because of β^2 dependence which makes it an inefficient process for CR acceleration,

2.3.1.2. Diffusive Shock Acceleration

Several improvements were incorporated to the second-order Fermi mechanism over the course of two decades [30–33]. The diffusive shock acceleration mechanism scales the gain in energy linearly with β as opposed to its older counterpart, and hence is also called first-order Fermi acceleration. It was initially developed for accelerators such as the supernoave (SNe), where the particles can scatter from a large plane shock front, as illustrated in Fig. 2.3. In a fluid medium, a shock is formed when velocity of the an object exceeds the speed of sound in the medium.

A shock front moving towards left with a velocity $-\vec{u}_1$, into a gas moving towards the right with velocity $\vec{u}_2$ relative to the shock front, will impart a velocity to the gas equal $\vec{V} = -\vec{u}_1 + \vec{u}_2$, moving the gas to the left in the lab frame. The relative energy gain by the gas particles is then given by,

$$\frac{\Delta E}{E} \approx \frac{4}{3}\beta,\tag{2.5}$$

where $\beta = |\vec{u}_1 - \vec{u}_1|$. Unlike the first-order Fermi acceleration due to plasma clouds, each interaction of particles with the plane shock front results in a positive energy gain, resulting in a spectral index $\gamma \approx -2.0$. The discrepancy in the observed and predicted value of γ is based in the propagation of cosmic rays in the Galaxy, and will be discussed in the following sections.

2.3.2. Transport Equation of CR nuclei

Once accelerated as per the various mechanism described in the previous section, cosmic rays have to propagate through the interstellar medium before they are measured at Earth. The interstellar medium contains matter, magnetic fields and radiation fields, all of which are targets for cosmic ray interactions.

In the interest of this analysis, let us consider the propagation of a cosmic ray nuclear species 'i' in the interstellar medium (ISM). Then, the general equation describing its diffusive transport is written as[2],

$$\frac{\partial N_i}{\partial t} = Q_i - V \cdot \nabla N_i + \nabla \cdot [D \nabla N_i] - \left(\frac{1}{\tau_{\text{int}}} + \frac{1}{\tau_{\text{rad}}} \right) N_i + \sum_{j \neq i} \frac{P_{\text{j} \rightarrow \text{i}}}{\tau_{\text{j} \rightarrow \text{i}}} N_j. \tag{2.6}$$

where N_i is the number density of nucleus 'i' at a given an energy per nucleon E, position x, and time t. The first term on the right side of Eq. (2.6), Q_i is the source or the injection term. The second term depicts the convection of particles in a fluid with a velocity field V, whereas the third term is the spatial diffusion of the particles with a diffusion coefficient D. The fourth term collectively denotes the loss of the nucleus 'i' by fragmentation on the ISM or by decay for a radionuclide, characterized by the time-scales τ_{int} and τ_{rad}, respectively. Finally, the last term is the sum over the feed down from the reaction channels 'j' →'i'. It accounts for the fragmentation of all the heavier nucleus of type 'j' on the ISM protons, resulting in the production of nucleus 'i', and is described by the interaction probability $P_{\text{j} \rightarrow \text{i}}$. The denominator in this term $\tau_{\text{j} \rightarrow \text{i}}$ is the characteristic time-scale for the interaction.

One of the simplest models of CR propagation is called the "leaky box" model. This model assumes a flat cylindrical geometry, with CR sources embedded in the disc galaxy at the centre along the cylindrical length. It is convenient to introduce the half length of the cylinder, as h. Cosmic rays are contained within the cylindrical volume, within which they propagate freely. In addition there is a finite constant probability per unit time to escape the containment volume, such that $c\tau_{\text{esc}} \gg h$, where c is the speed of light in vacuum and τ_{esc} is the mean time in the containment volume. Under this approximation, the convection and diffusion terms in Eq. (2.6) can be replaced as,

$$V \cdot \nabla N_{\text{i}} - \nabla \cdot [D \nabla N_{\text{i}}] \rightarrow \frac{N_{\text{i}}}{\tau_{\text{esc}}}. \tag{2.7}$$

---

[2]The equations in the following sections are based on the derivations in Refs. [28, 34].

The mean amount of matter traversed by the cosmic rays called the grammage is denoted as X and is measured in g/cm^2. It can be expressed in terms of the escape time as,

$$X_{\text{esc}} = \rho v \tau_{\text{esc}}, \tag{2.8}$$

where ρ is the mass density of the Galactic matter[3], and v is the relativistic velocity of nucleus 'i'. On similar lines, the characteristic rate of loss due to inelastic interaction of 'i' on the ISM can be expressed in terms of the corresponding grammage before undergoing the interation, andis written in the form of Eq. (2.8), as,

$$X_{\text{int}} = \rho v \tau_{\text{int}}, \tag{2.9}$$

The last term in Eq. (2.6) related to the production of 'i' from the heavier progenitor nuclei 'j' is related to it the production cross section $\sigma_{j \to i}$ via the interaction probability as $P_{j \to i} \approx \left(\frac{X_{j \to i}}{m_{\text{p}}} \right) \sigma_{j \to i}$, and the characteristic spallation time $\tau_{j \to i}$ is written in the form of Eq. (2.9). Therefore, the ratio of the probability to the spallation time is written as,

$$\frac{P_{j \to i}}{\tau_{j \to i}} = \frac{\rho v \sigma_{j \to i}}{m_{\text{p}}}. \tag{2.10}$$

In a state of equilibrium, the number of particles inside the confinement volume is constant with respect to time i.e., $\partial N / \partial t = 0$. Therefore, the final expression derived after making the necessary substitutions from Eqs. (2.8) to (2.10) into the diffusion equation Eq. (2.6), is given as,

$$\left(\frac{\rho v}{X_{\text{esc}}} \right) N_i = Q_i - \left(\frac{\rho v}{X_{\text{int}}} + \frac{1}{\tau_{\text{rad}}} \right) N_i + \sum_{j \neq i} \left(\frac{\rho v \sigma_{j \to i}}{m_{\text{p}}} \right) N_j. \tag{2.11}$$

Eq. (2.11) represents a simplified version of the steady state equation of CR transport in the Galaxy for a nucleus 'i', wherein the system of process of creation and destruction of cosmic rays is in a state of equilibrium. Various important quantities of astrophysical interest, for instance the total grammage traversed by the Galactic CRs along their diffusive path towards the Earth, the time spent by the CRs in the Galaxy, can be estimated by plugging in the required inputs in Eq. (2.11), and will be discussed in the next section.

---

[3]For simplicity, the ISM is assumed to be composed of pure hydrogen of mass m_{p}. Therefore, the number density is $n_{\text{ISM}} = \rho_{\text{ISM}} / m_{\text{p}}$
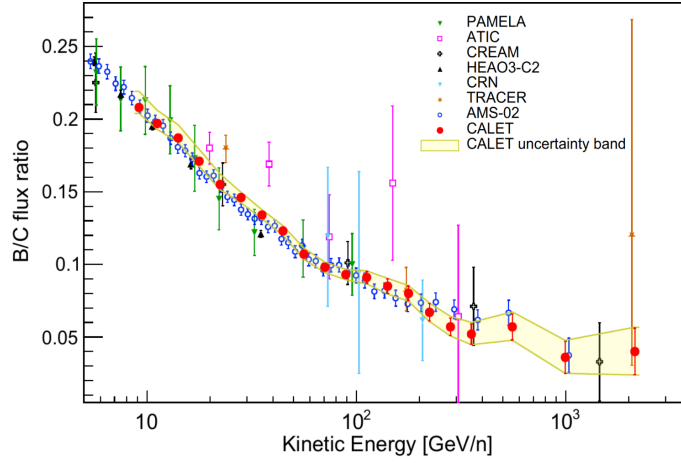
Figure 2.4.: Boron-to-carbon flux ratio measured by the CALET detector. Figure is taken from Ref. [4].

2.4. Secondary-to-Primary Flux Ratios

As mentioned above, cosmic rays can be broadly classified into two categories: first, primary cosmic rays, that are produced and accelerated from the sources e.g. Supernova Remnants (SNR) diffusing in the Galactic magnetic field, and second, the secondary cosmic rays produced by hadronic and nuclear interactions of the primary species on the interstellar medium (ISM).

The primary CR nuclei like C, N, O are accelerated in SNRs and propagate in the Galactic medium (ISM), composing mostly of neutral and ionized hydrogen ($\sim 90\%$), and helium gas ($\sim 10\%$). They interact with the ISM resulting in lighter fragments like Li, Be, and B. The measured flux ratios of the stable secondary-to-primary species are used to infer astrophysical quantities such as the traversed grammage [35], while the flux ratios of unstable-to-stable secondary nuclei are used as cosmic radioactive clocks to determine the residence times of CRs in the Galaxy, and calculate the density of the ISM gas encountered by the cosmic rays. Routinely, the B-to-C flux ratio is the most widely used quantity to determine the grammage X, owing to the entirely secondary nature of boron, and the relatively high cosmic abundance of the two elements. Secondary-to-Primary flux ratios as recently measured by CALET [4] is shown as a function of energy/nucleon in Fig. 2.4, superimposed with model lines for various propagation scenarios. To begin with, let us consider the propagation of B in the Galaxy. Since boron is not produced in the CR sources, the injection term $Q_B = 0$. Also, since boron is a stable nucleus, the rate of loss of boron due to radioactive decay term can be neglected. Therefore, in the steady state scenario, the

number of boron at any given instant of time t can be written in the form of Eq. (2.11) as,

$$\left(\frac{\rho v}{X_{\text{esc}}}\right) N_{\text{B}} = -\left(\frac{\rho v}{X_{\text{int}}^{\text{B}}}\right) N_{\text{B}} + \left(\frac{\rho v \sigma_{\text{C}\rightarrow\text{B}}}{m_{\text{p}}}\right) N_{\text{C}}. \tag{2.12}$$

For the purpose of simplifying the formulation, only fragmentation of C$\rightarrow$B is considered in Eq. (2.12). In principle, all fragmentation channels of boron production, such as O$\rightarrow$B should be considered for a more precise estimation of the grammage. It is straightforward to obtain the following final expression for the Boron-to-Carbon flux ratio from Eq. (2.12) and is similar to Eq.(9.11) from [28]:

$$\text{B/C} = \frac{N_{\text{B}}}{N_{\text{C}}} = \frac{X_{\text{esc}}}{1 + X_{\text{esc}}/X_{\text{frag.}}^{\text{B}}} \frac{\sigma_{\text{C}\rightarrow\text{B}}}{m_{\text{p}}}. \tag{2.13}$$

It is immediately clear from Eq. (2.13) precise fragmentation cross section characterized by the quantities $\sigma_{\text{C}\rightarrow\text{B}}$ and $X_{\text{int.}}$ are required to accurately predict the fluxes of B and C. The energy dependence of the B/C ratio as seen in Fig. 2.4 can be fit with a single power law as $E^{-\delta}$, where E is the kinetic energy per nucleon. In fragmentation reactions, E is conserved, hence the spectrum of the primary CRs should be inherited by the secondary CRs as well. Therefore at the source the flux ratio will be flat. The energy dependence can be understood as a propagation effect as follows: in turbulent magnetic fields, the diffusion coefficient $D \propto E^{\delta}$, where $0.3 \leqslant \delta \leqslant 0.5$ (from standard theoretical models of turbulence in magnetized plasmas). Therefore, the traversed mass density $X_{\text{esc}} \propto E^{-\delta}$. If the flux of primaries at the source is $N_{\text{p}} \propto E^{-\alpha}$, then after propagation it is modified to $N_{\text{p}} \propto E^{-\alpha-\delta}$ as measured at Earth, where $\alpha + \delta = \gamma_{\text{obs}} \approx 2.7$. And for secondary nuclei $N_{\text{s}} \sim X_{\text{esc}} N_{\text{p}}$. Hence the secondary to primary ratio such as the B/C is characterized by a single power law as $B/C = N_{\text{s}}/N_{\text{p}} \sim E^{-\delta}$.

Additionally, primary CR interactions also produce unstable secondary nuclei, which decay to stable nuclei. A few prominent examples of such secondary CR species is ^{10}Be, ^{26}Al, ^{36}Cl and ^{54}Mn are useful probes for investigating Galactic CR propagation [36–38]. The ratio of the unstable to stable secondary isotope allows to calculate the average density of matter ρ encountered by the primary cosmic rays. The secondary nuclei ^{10}Be is the best measured isotope. It converts to the stable ^{10}B via β^- decay with a half life 1×10^6 y. Since Eq. (2.11) determines the grammage as expressed in Eq. (2.8), the escape time τ_{esc} is required to compute the matter density ρ. Measurement of the unstable-to-stable isotope
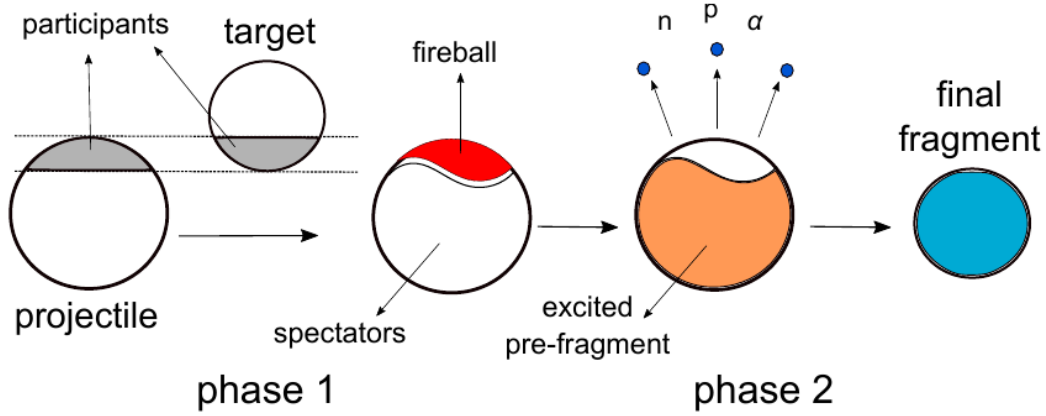
Figure 2.5.: An illustration of the two phases of the abrasion-ablation model of nuclear fragmentation as described in the text. Figure is taken from [39].

ratio breaks this degeneracy. An equation of the form of Eq. (2.11) can written for the nuclei ^{10}Be and ^{9}Be individually, the ratio of which then can be written as,

$$\frac{N_{10\text{Be}}}{N_{9\text{Be}}} = \left(\frac{1 + X_{\text{esc}}/X_{\text{int}}^{9\text{Be}}}{1 + X_{\text{esc}}/X_{\text{int}}^{10\text{Be}} + \tau_{\text{esc}}/X_{\text{int}}^{10\text{Be}}} \right) \frac{\sigma_{\text{C}\to10\text{Be}}}{\sigma_{\text{C}\to9\text{Be}}}. \tag{2.14}$$

A calculation of ρ from the estimation of the inputs to Eq. (2.14) is presented in Ref. [28]. It shows that the derived value of the matter density is significantly lower than the gas density in the disk, suggesting that a large fraction of residence time of primary nuclei is spent outside the disk, in the Galactic halo. The dependence on the production cross section of ^{10}Be and ^{9}Be is evident from Eq. (2.14).

2.5. Nuclear Interactions of Cosmic Rays

As can be seen explicitly from Eqs. (2.13) and (2.14), nuclear interactions play a key role in formation of spallation products of primary cosmic rays as discussed in Sec. 2.4. This section presents a brief introduction to the theory of nuclear fragmentation. The short range of strong forces responsible for holding the nucleus together implies that nuclear reactions are contact interactions and are relevant only when the radii of the colliding nuclei overlap. The distance between the centers of the projectile and the target nucleus is called the impact parameter b.

The theory of fragmentation is based on the *abrasion-ablation* model for heavy ion collisions (see e.g. [40]). It is a theoretical framework used to describe relativistic heavy ion collisions. The process of collision is divided into two stages: abrasion and ablation. During the abrasion stage, the colliding nuclei interact through their nuclear surfaces, leading to the removal of nucleons from the surface regions of the nuclei. This process is governed by the overlap of the nuclear density profiles and can be described mathematically by the Glauber model, which calculates the probability of overlap between the two nuclei as they approach each other [41]. Nucleons in the overlap region are called participants and lead to the formation of a fireball emitting particles such as pions. On the other hand, the remaining nucleons are called spectators.

Following the abrasion stage, the ablation stage begins, where the spectators of the projectile form a pre-fragment, and continue to interact and exchange energy until they separate into final state fragments. This process involves the emission of nucleons and light fragments from the colliding nuclei and is characterized by the exchange of kinetic energy between the fragments. The two stage process is graphically illustrated in Fig. 2.5.

The abrasion-ablation model provides a useful framework for studying heavy-ion collisions and has been applied in various theoretical and experimental studies to understand phenomena such as nuclear stopping, energy dissipation in these collisions, and fragment production as well.

Following the fragmentation model, the next task is to quantify the interaction by defining their respective cross sections. In an accelerator-based fixed target experiment, the cross section, σ of the beam particles (b) to interact with the target nucleus (T) is given by the interaction rate divided by the total flux of the beam incident on the target and is equivalent to a transverse area of the target nucleus encountered by the beam nucleus. It is written as,

$$\sigma_{b+T} = \frac{1}{\Phi_b} \frac{dN_{b+T}}{dt}, \tag{2.15}$$

where the flux of beam particles is defined as the differential number of beam particles crossing an area element dA in the time interval dt, $\Phi_b = dN_b/(dAdt)$. For a target of mass density ρ, molar mass M, and thickness d_T, the area element $dA = M/(N_A\rho dx)$, where $N_A = 6.022 \times 10^{23}$ is Avogadro's constant, and dx is the differential target thickness. Substituting Φ_b in Eq. (2.15) gives,

$$\frac{dN_{b+T}}{dt} = \frac{dN_b}{dt} P_{b+T}, \tag{2.16}$$

where $P_{a+b} = \sigma_{b+T}/dA$ is the interaction probability.

Different types of cross sections can be defined based on Eq. (2.15). The first is the total cross section σ_{tot}, which accounts for all beam-target interactions without taking the type and yield of the final state particles into consideration. The second type is called elastic cross section σ_{el}, and measures interactions when the kinetic energy of the system is conserved, and the incoming and outgoing particles are identical, and no new particle is produced. The total cross section includes elastic cross section as well. Therefore, the processes in which at least one new particle is formed due to the beam-target interactions is described by the inelastic cross section σ_{inel}. Then it immediately follows that, $\sigma_{inel} = \sigma_{tot} - \sigma_{el}$. In the case of nuclear interactions, the quasi-elastic cross section σ_{qel} is defined as scattering process leading to disintegration of the nucleus, without producing additional new particles. Therefore the production cross section of particular nucleus is written as, $\sigma_{prod} = \sigma_{tot} - \sigma_{el} - \sigma_{qel} = \sigma_{ine} - \sigma_{eql}$.

The inelastic cross section σ_{inel}^{hA} derived from the Glauber theory for hadron-nucleus (hA) interactions is given as (see Eq.(4.83) from Ref. [28]),

$$\sigma_{inel}^{hA} = \int d^2b \left(1 - \exp\left(-\sigma_{tot}^{hp} T(b)\right)\right), \tag{2.17}$$

where σ_{tot}^{hp} is the total hadron-nucleon cross section , $T(b)$ is the number density of nucleons of the target nucleus at impact parameter b. Eq. (2.17) is useful in calculating the inelastic cross sections of the CR nucleus on the ISM protons. Data driven empirical approximation shows that in the momentum range $20 - 50\,\text{GeV}/c$, Eq. (2.17) for proton-nucleus (mass number A) interaction for $A > 1$ can be written as (see [42]),

$$\sigma_{ine}^{pA} \simeq 45\,\text{mb}\,A^{0.691}. \tag{2.18}$$

Whereas in the case of nucleus-nucleus collision ($A + B$), the inelastic cross section can be parameterized using the formula,

$$\sigma_{inel}^{AB} = \pi R_0^2 \left(A^{1/3} + B^{1/3} - \delta\right)^2, \tag{2.19}$$

where the value for the constants $R_0 = 1.47 \times 10^{-15}$ m and $\delta = 1.12$ is taken from Ref. [43].

In this thesis, the emphasis is on studying three types of fragmentation reactions: mass-changing, charge-changing and production reactions. The mass-changing reaction is

defined as an inelastic interaction leading to loss of at least one nucleon from the projectile nucleus P of mass A_P, upon interacting with the target nucleus, such that change in the projectile mass $\Delta A_P \geqslant 1$. A charge-changing reaction is an inelastic interaction in which at least one proton is lost from the projectile nucleus of charge Z_P, upon interacting with the target, such that the change in the projectile charge $\Delta Z_P \geqslant 1$. Every charge-changing reaction is necessarily a mass-changing reaction. but the converse is not true. The third kind of reaction is the fragmentation of projectile nucleus proceeding through a particular channel, resulting in the production of a specific fragment nucleus.

As a result of the fragmentation process, the participant nucleons comprising the final fragment nucleus posses a non-zero component of their 3-momentum in the rest frame of the fragment i.e. $\sum_i p_i = 0$, for the nucleon i with momentum p_i. This momentum is called the Fermi momentum (p_F) and is attributed to the quantum mechanical phenomenon called Fermi motion. It describes the motion of the nucleons bound inside a nucleus and depends on the depth of the nuclear potential well. The fragment momenta in ^{16}O+Be interactions at 2.1 $A\,\mathrm{GeV}/c$ were observed to follow a Gaussian distribution [44], $\exp\left(-p^2/2\sigma_p^2\right)$. Statistical models were developed to explain the distribution of the fragment momentum [45, 46]. The mathematical expression has the form (see Eq.(1) in [46]),

$$\sigma_p^2 \approx \sigma_0^2 \left(\frac{F(A-F)}{A-1} \right), \tag{2.20}$$

In Eq. (2.20), F is the mass number of the fragment and A is the mass number of the projectile. The proportionality constant σ_0 is expressed in terms of the Fermi momentum p_F, as $\sigma_0 = p_F^2/5$. Assuming a canonical value of Fermi momentum $p_F \approx 250\,\mathrm{MeV}/c$ yields the value for the constant $\sigma_0 \approx 110\,\mathrm{MeV}/c$ (see [46] for full description of the model).

2.6. Need for Improved Cross-sections

The relevant reaction channels for predicting the total boron production in the Galaxy in ^{12}C+proton interactions are the through the direct production of the stable boron isotopes ^{11}B and ^{10}B, and via the indirect channel from ^{11}C. Carbon-11 is a secondary radionuclide produced in spallation reactions of the primary CRs, which converts to the stable ^{11}B as ^{11}C$\rightarrow^{11}$B $+ \beta^+$, with a half-life $\tau_{1/2} \approx 20$ mins. Since $\tau_{1/2}$ is significantly less than the typical astrophysical timescales CRs spend in the galaxy (~ 1)Myr, the contribution from ^{11}C is
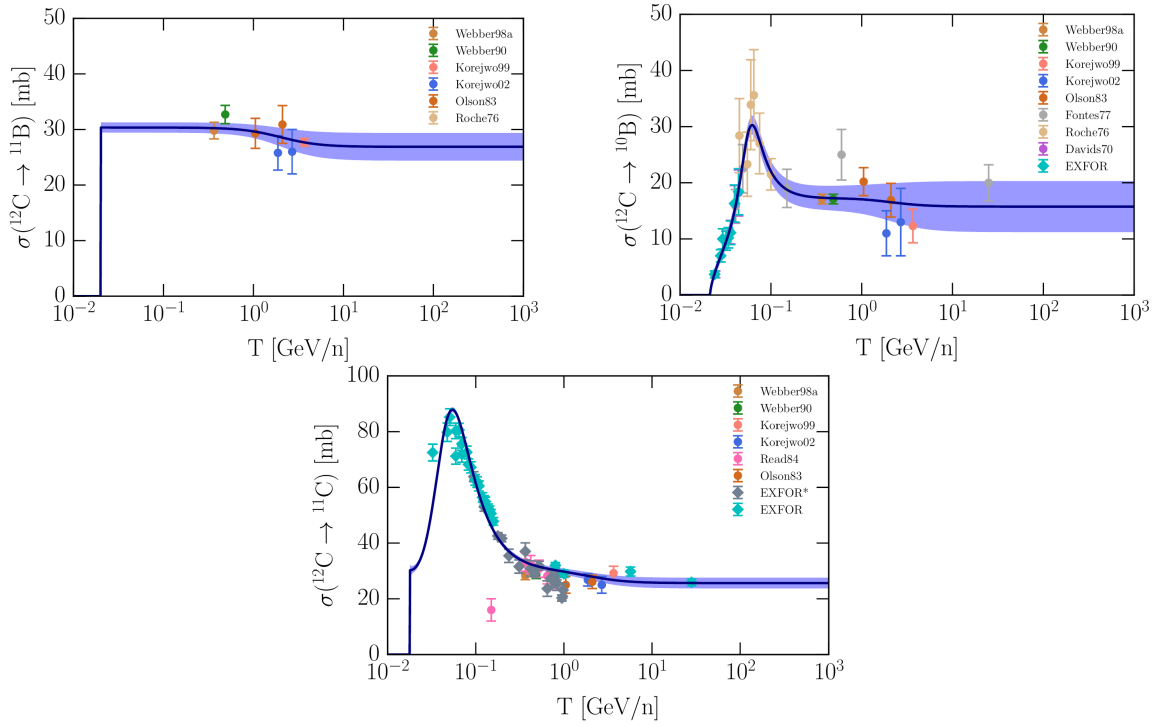
Figure 2.6.: Previous measurements of ^{12}C+p cross sections for the production of boron isotopes (top) and ^{11}C (bottom). The solid blue line and the purple band correspond to cross section model and the corresponding model uncertainty given in [47].

crucial in production of cosmic boron. Such nuclei are termed "ghost nuclei", as they are never directly observed at Earth. In addition, two more reaction channels are responsible for production of cosmic boron, they are: the decay of ^{10}Be→^{10}B, and ^{10}C→^{10}B. The impact of these channels on the total boron flux is comparatively small at approximately 7% of total boron flux prediction from ^{12}C [48]. The next most important progenitor for boron is ^{16}O, but it is out of the scope of the current work and will not be discussed in this thesis.

The current measurements of isotope production cross sections for ^{11}C, ^{11}B, and ^{10}B from ^{12}C shows a lack of precise cross section data at energies beyond $10\,A\,$GeV$/c$. A single high energy measurement of ^{11}C production at $28A\,$GeV$/c$ was performed by irradiating a graphite target with a proton beam and measuring its activity [49]. A comparison of previous measurements is shown in Fig. 2.6. The uncertainties in the current cross section data are at $\approx 10-20\%$ and even higher for some reaction channels [48], and is the largest source of uncertainty in determining the propagation parameters, namely the diffusion coefficient D and its energy dependence parameter δ. Propagation parameters inferred
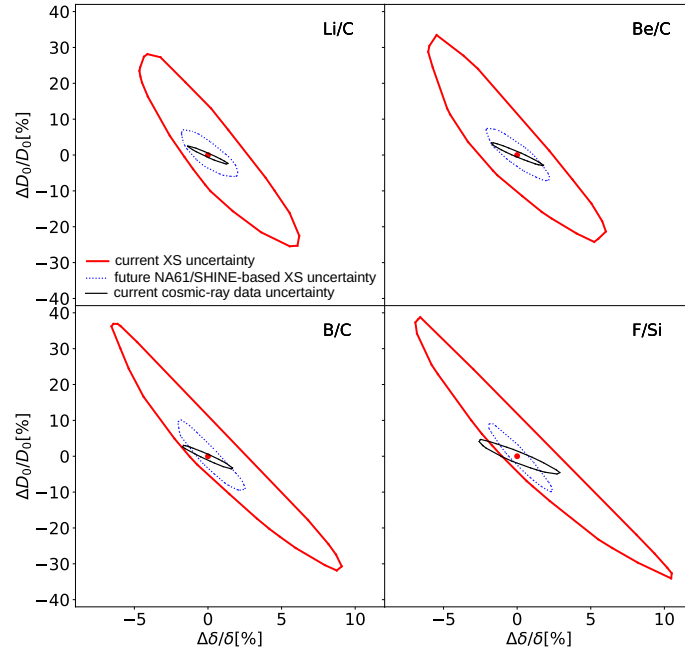
Figure 2.7.: Prediction of the accuracy to determine the transport parameters D_0 and δ derived from the four secondary-to-primary CR ratios Li/C, Be/C, B/C, and F/Si shown as 1σ contour in the relative error plane of the two parameters. Current uncertainty due to cross sections is shown as red contour, and the estimated uncertainty from future NA61/SHINE measurement as blue. The black contour is the intrinsic intensity from the data. Adapted from [50].

from the B/C ratio must be applicable to other secondary-to-primary ratios as well. The relevance of improving the cross section uncertainties of certain channels was reported in a recent work [50]. The improvement in the relative uncertainty of the transport parameters D_0 and δ (see Sec. 2.4) by improving the boron and fluorine production from carbon and silicon is shown in Fig. 2.7. Anomalies in the measured flux of elements indicates an excess in the cosmic lithium and fluorine fluxes as observed from the Li/C and F/Si ratios [51]. In contrast to the secondary nature of L Li and F, claims for a possible primary origin of these elements were put forth to explain the excess [52, 53]. These recent findings can not be resolved without nuclear cross sections with improved uncertainties [5, 54, 55]. Measurement of the flux ratio of unstable-to-stable secondary such as the ^{10}Be/^{9}Be can help break the degeneracy of the L/D ratio, where L is the Halo size and D_0 is the diffusion coefficient, inferred from the measurement of stable secondary-to-primary ratios such as B/C [56–58]. The impact of nuclear cross sections uncertainties in forecasting the relative precision of the size of the Galactic halo is shown in Fig. 2.8.

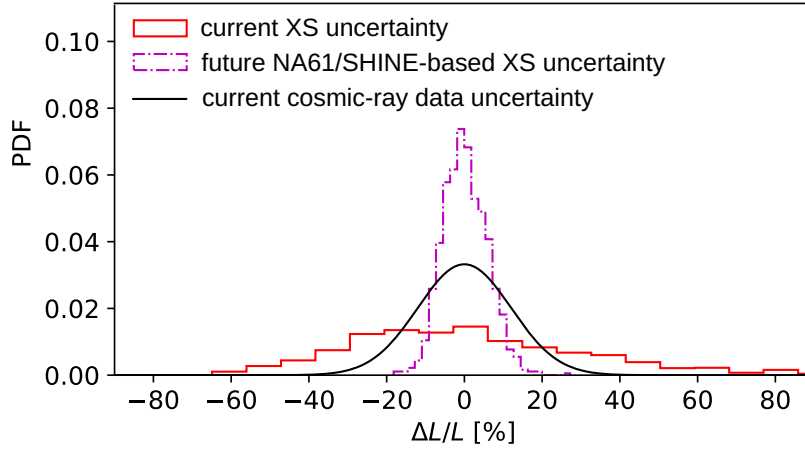Figure 2.8.: Distribution of the estimated relative precision of the Galactic halo size L from arising from the nuclear cross section measurements of the beryllium isotope production. Red distribution shows the current uncertainty on L with a standard deviation $\approx 30\%$, and magenta distribution shows the improved precision better than the flux measurements, with the new cross sections, with a standard deviation $\approx 5\%$. Figure adapted from [50]

Another interesting discovery is that of the antimatter excess observed in CR positron fraction $e^+/(e^- + e^+)$ up to $100\,\mathrm{GeV}$ first discovered by PAMELA [59], and later confirmed by Fermi-LAT [60] and AMS-02 [61]. While γ-ray emissions from the M31 halo in the energy, range $3-20\,\mathrm{GeV}$ suggests a similarity with Galactic center and the $\overline{p}$ excess [62–64]. Anti-matter like the excess e^+ and $\overline{p}$ are probes into indirect detection of dark matter. Nevertheless, the estimation of the secondary antiproton production flux is severely hampered by large uncertainties in nuclear cross sections and those of the transport parameters. The transport parameters can be inferred by the B/C flux ratio provided cross section with improved uncertainties are measured. This will help in predicting the secondary anti-matter flux from cosmic ray interactions that constitutes the background to dark matter signals. Detailed calculations of the impact of nuclear cross sections on determining the secondary $\overline{p}$ flux was performed in [50] and is shown in Fig. 2.9.

Enough evidence from various new studies indicate that fresh nuclear cross sections measurements with reduced uncertainties will provide clear insights into interpreting the recent discoveries. The goal of this thesis is to present the first results of cross section measurements of boron production from primary carbon nuclei, at $E > 10\,A\,\mathrm{GeV}/c$, as will be discussed in the following chapters.
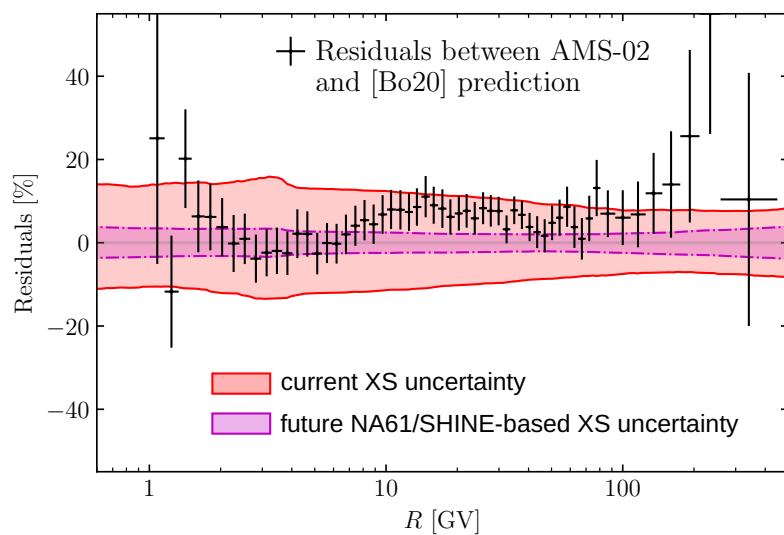
Figure 2.9.: Estimated accuracy on the predicted $\overline{p}$ flux after future NA61/SHINE measurements reaching precision levels better than the AMS-02 data [65], shown as the magenta envelope, while the red envelope is the uncertainty due to current cross section values. Adapted from [50].

3. The NA61/SHINE Facility

In this thesis, data collected with the NA61/SHINE facility is analyzed to study fragmentation of the ^{12}C nucleus. NA61/SHINE stands for SPS Heavy Ion and Neutrino Experiment. It is located in the CERN North Area, inside the Experimental Hall North 1 (EHN1) on the H2 beamline of the Super Proton Synchrotron (SPS). It is the successor to the NA49 experiment. It operates within a beam momentum range of approximately $10 - 450\,\mathrm{GeV}/c$. The physics programs of the experiment primarily focus on studying hadron-hadron and hadron-nucleus interactions in the interest of phase transitions in strong interactions and investigating the properties of neutrino beams produced in p-nucleus collisions for long baseline neutrino oscillation experiments. In addition to these, it is also aimed at measuring nuclear fragmentation cross-sections in nucleus-nucleus interactions, in the interest of Galactic cosmic ray propagation and extensive air-shower studies [66].

This chapter briefly describes the SPS accelerator (Sec. 3.1), the H2 beamline (Sec. 3.2), and the main and sub-detector systems of the NA61 experimental facility required for fragmentation studies (Sec. 3.3). The recent hardware upgrade that was undertaken during the CERN Long Shutdown 2, between 2019 and 2022 is detailed in Sec. 3.6.

3.1. CERN Accelerator Chain

Protons and ions are primarily accelerated by the liner accelerators LINAC2 and LINAC3 respectively. The protons energies are further boosted in the Proton Synchrotron Booster (PSB) or simply the Booster, before feeding it to the Proton Synchrotron (PS). Heavy ions are bunched into shorter pulses using the Low Energy Ion Ring (LEIR), post which they transported to PS. Protons and heavy ions are finally fed in to the Super Proton Synchrotron (SPS) for further acceleration, before directing the beam towards the CERN North Area or feeding the Large Hadron Collider (LHC). The accelerator chain is illustrated in Fig. 3.1.
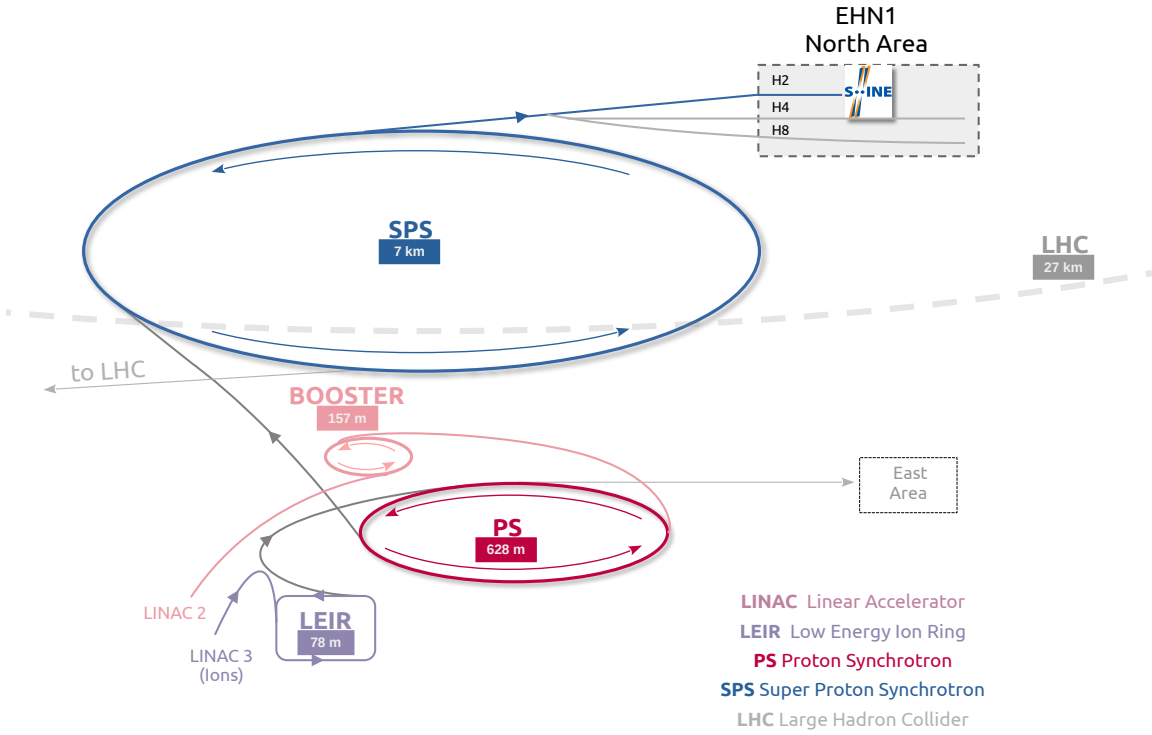
Figure 3.1.: The CERN accelerator complex with the accelerators relevant for particle transport to NA61/SHINE. The quoted value is the circumference of each accelerator (figure adapted from [67]).

The SPS is a particle accelerator, originally designed to achieve a maximum particle energy of 400 GeV. It has been used to accelerate protons, antiprotons, electrons, positrons, and heavy ions as well. Its major scientific results include the discovery of the W and Z boson during its operation as a hadron collider from 1981 to 1991, and the discovery of direct CP violation by the NA48 experiment. Today, it is the second-largest component within the CERN accelerator complex, boasting a circumference of ∼ 7 km. Its primary function is to accelerate particles from the Proton Synchrotron (PS) for generating beams to be injected in the LHC. Operating at a maximum of 450 GeV, it features 1317 conventional electromagnets, including 744 dipole magnets strategically placed to bend the particle beams along the circular path. The SPS also serves a variety of experiments like NA62 (the successor of NA48 experiment), the Common Muon and Proton Apparatus for Structure Spectroscopy (COMPASS), and the NA61/SHINE experiment. Additionally, the SPS is set to contribute to the AWAKE experiment, designed to explore innovative particle acceleration techniques.

The duration for which the beam is extracted from the SPS is called a spill. For the North Area the spill duration depends on the number of SPS users, and lasts for about 10 s with a 30% duty cyle. The intensity of the beam in proton mode is typically $\sim 10^{13}$ protons/cycle, and that for ions is $\sim 10^8$ per cycle. Its stable operational range of deliverable momenta for ion beams is $13A\,\text{GeV}/c$-$160A\,\text{GeV}/c$ [66].

3.2. H2 Beamline

The hadron and ion beams required for the physics programs of NA61/SHINE are provided by the SPS, and are further transported to EHN1 via the H2 beamline. H2 is capable of delivering positive as well as negatively charged particles. A secondary beam of positively (π^+, K^+) or negatively charged (π^-, K^-) particles is produced by directing a primary proton beam extracted from the SPS on to a primary Be target called T2. The target station is located ≈ 530 m upstream of the NA61/SHINE production target, and hosts several Be plates of different lengths. A target of appropriate length is chosen from these plates, that optimizes the yield of the requested secondary particle. For producing a secondary ion beam, a primary ^{208}Pb ion beam is guided on the T2 target. The fragmentation of the Pb ion produces secondary nuclei, which are then transported to EHN1. The H2 beamline is tuned to match with the momentum of the ions extracted from the SPS. The selection is performed by two large spectrometers. Multiple sets of dipole and quadrupole magnets on the beamline are used to steer and focus the beam particles, respectively. In the case of transporting a beam of specific ions, the H2 beamline selection is based on the rigidity R of the ion, which is proportional to its mass-to-charge ratio (A/Z). Additionally, the fragmentation of the ^{208}Pb ion smears the fragment momenta due to the Fermi motion of the nucleons. Therefore, the beam is mixed with other nuclear species with similar mass-to-charge ratio, and the elements neighboring the desired ion. The spectrometer has a maximum rigidity acceptance of $\Delta R/R \approx \pm 1.7\%$ [66]. The next section discusses the NA61/SHINE detector systems specifically relevant for performing fragmentation studies.

3.3. NA61/SHINE detectors

The schematic layout of the NA61/SHINE detectors is shown in Fig. 3.2. To study the fragmentation of a particular nucleus in the incoming beam it is crucial to determine its
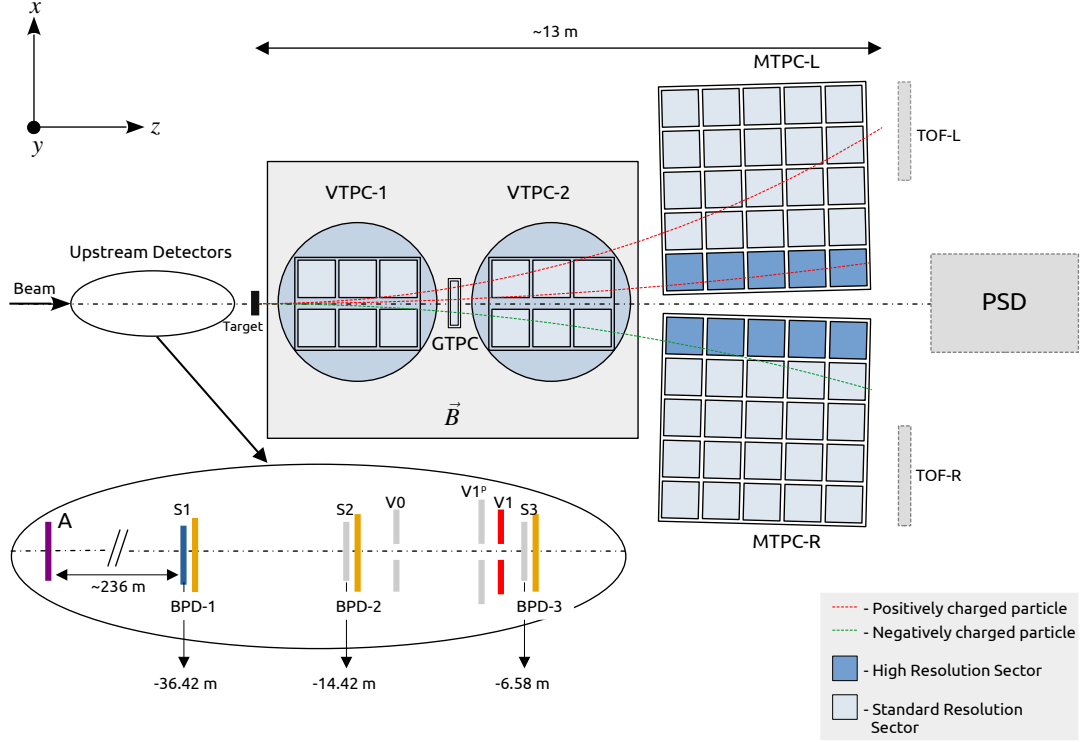
Figure 3.2.: NA61/SHINE experimental setup as used for this measurement. Detectors in grey were not used, but will be described briefly in Sec. 3.4.

charge and isotope before it is incident on the target. For this purpose, the beamline is equipped with detectors upstream of the target (shown in the inset of Fig. 3.2). These detectors are used to monitor the characteristics of the incoming beam, such as particle identification, timing information, understanding beam divergence, and defining trigger logic. These detectors include the scintillator counters, the Beam Position Detectors (BPDs), and veto scintillators. Similarly, the identification of the secondary fragments produced in the beam-target interactions is achieved by two sets of Time Projection Chambers (TPCs). The main detectors used for tracking the nuclear fragments are the Vertex-TPCs (VTPC-1/2) placed inside a set of superconducting magnets and the large acceptance Main TPC (MTPC-L/R). Both TPCs are placed symmetrically on the left and right of the beamline.

3.3.1. Detectors Upstream of the Target

The beamline detectors preceding the target are used as beam counters, to study the properties of the incident beam, as shown in the inset of Fig. 3.2. They primarily consist of a series of plastic scintillators of type BC-408, made of polyvinytoluene. The most upstream detector used for fragmentation studies is a $L \times B \times H = 6 \times 6 \times 0.5\,\text{cm}^3$ scintillator called the A detector. It is followed by the scintillator S1 with the same dimensions and material as that of the A-detector. Light output of the A and S1 detectors is read out with two and four fast PMTs (EMI9133) respectively. The four PMTs directly coupled to the S1 counter facilitate precise timing measurements (resolution $\approx 30\,\text{ps}$) in low multiplicity events. While the S1 is situated $36.42\,\text{m}$ from the target z position, the A detector is placed $\approx 240\,\text{m}$ further upstream of the S1, inside the beam tunnel. The A-S1 system records the arrival times of the incoming beam. This timing information is used in determining the time-of-flight (*tof*) corresponding to the various beam nuclei. Since the measured *tof* is a function of the mass of the particle, this information helps in the identification of the isotopes, which is a crucial step in this study.

Let us consider a beam nucleus consisting of A nucleons. Its rigidity is given by the ratio of the total momentum p to its electric charge Z as, $R = p/Z$. The *tof* t of this nucleus is given by,

$$t = \frac{L}{c\beta}, \tag{3.1}$$

where L is the distance between the two counting scintillators A & S1, the denominator is the relative velocity of the nucleus, with c the speed of light, and β is the ratio of momentum and the total energy of the nucleus. It is expressed in terms of its rigidity and mass as,

$$\beta = \frac{p}{E} = \frac{RZ}{\sqrt{(RZ)^2 + (Au)^2}}. \tag{3.2}$$

The total mass of the nucleus is expressed as Au, in terms of the mass number and the atomic mass unit u. Therefore, the time of flight t is given by the equation,

$$t = \frac{L}{c} \left(\frac{RZ}{\sqrt{(RZ)^2 + (Au)^2}} \right). \tag{3.3}$$

The total resolution σ_t of the measured *tof* depends on two factors. First, the spread in the measured times due the uncertainty in light travel time inside the scintillators A and

S1, before it reaches the PMT, and is denoted as σ_{LT}. The second factor is the intrinsic resolution of the PMT itself, σ_{PMT}. Therefore, the total *tof* resolution is given by,

$$\sigma_t = \sqrt{\sigma_{LT\text{-}S1}^2 + \left(\frac{\sigma_{PMT}}{N_{PMT\text{-}S1}}\right)^2 + \sigma_{LT\text{-}A}^2 + \left(\frac{\sigma_{PMT}}{N_{PMT\text{-}A}}\right)^2}. \tag{3.4}$$

Since the PMTs connected to the A and the S1 detectors are of the same type, a single quantity σ_{PMT} is used to describe its intrinsic resolution, weighted by the number of PMTs for A and S1, as $N_{PMT\text{-}A} = 2$ and $N_{PMT\text{-}S1} = 4$, respectively.

The rate of energy loss by a relativistic particle of charge Z, and speed v, traversing a material of charge z and relative atomic mass A, is described by the Bethe equation as,

$$-\frac{dE}{dx} = KZ^2 \frac{z}{A} \frac{1}{\beta^2} \left(\frac{1}{2}\ln f(\beta) - \beta^2 - \frac{\delta(\beta\gamma)}{2}\right), \tag{3.5}$$

where K is a proportionality constant, $\beta = \frac{v}{c}$, and $\gamma = \frac{1}{\sqrt{1-\beta^2}}$ is the Lorentz factor. Therefore, the charge of the incident beam particle is determined from its charge squared equivalent energy deposited in S1. The signal is used to trigger on the desired beam particle. Moreover, the detector V1 is a square scintillator of dimensions $L \times B = 10 \times 10 \, \text{cm}^2$ with a central hole of 1 cm diameter. It is placed ≈ 1 m from the target z-position, upstream of BPD-3. The central hole defines the size of the incident beam on the target surface, and functions as a veto detector for highly diverging particles, missing the target. The signals from the S1 and V1 are used to define the trigger logic (see Sec. 4.2.1).

In the examination of incoming beam particle positions within the transverse plane, a telescope comprising three Beam Position Detectors (BPDs) is positioned along the beamline, preceding the target. The NA61/SHINE BPDs, featuring active areas of $4.8 \times 4.8 \, \text{cm}^2$, are multiwire proportional chambers (MWPC), employing an Ar/CO_2 gas mixture with an 85/15 ratio. Each BPD independently measures the position of the trigger-selected beam particle in two orthogonal directions by utilizing two planes of orthogonal sense wires. They are 15 μm thick tungsten wires with a 2 mm pitch. The determination of a 3-dimensional point by a specific Beam Position Detector (BPD) is built from two transverse coordinates obtained from the two strip planes and the BPD's position along the beamline. To reconstruct the trajectory of a beam particle, least squares fits of straight lines are conducted independently in the $x - z$ and $y - z$ planes using the positions measured by the three BPDs.

Table 3.1.: Technical details of the VTPCs, MTPC, and the GTPC [66].

	VTPC-1/2	MTPC-L/R	GTPC
Size (L×W×H) [cm]	$250 \times 200 \times 98$	$390 \times 390 \times 180$	$30 \times 81.5 \times 70$
Pad size [mm]	3.5×28.0	$3.6 \times 40.0, 5.5 \times 40.0$	4.0×28.0
Drift length [cm]	66.60	111.74	58.97
Drift velocity [cm/μs]	1.4	2.3	1.3
Drift field [V/cm]	195	170	173
Drift voltage [kV]	13.0	19.0	10.2
Gas Mixture	Ar/CO_2 (90/10)	Ar/CO_2 (95/5)	Ar/CO_2 (90/10)
No. of sectors	2×3	5×5	1

3.3.2. Detectors Downstream of the Target

A time projection chamber functions as a particle detector, discerning and characterizing particles by reconstructing their paths within a gas-filled volume. Positioned within a uniform magnetic field, the chamber can detect a curved trajectory of charged particles. A uniform electric field ~ 100 V/cm is established by applying a high voltage of the order of ~ 10 kV. The particle traversing the chamber initiates gas ionization, generating electron-ion pairs along the trajectory. These electrons drift along the electric field lines towards a set of three wire planes located at the top of TPC. The wire planes are shown in Fig. 3.3. The cathode plane ensures that at the sense wires, the signal from the electrons is amplified via Townsend avalanche. This induces a charge on the segmented pad plane which is then read out by the front-end electronics. The measured induced charge of the avalanche electrons and the arrival times provide help in the 3-dimensional reconstruction of the tracks. Analyzing the curvature and energy loss signal of these tracks determines the particle's charge and momentum.

The uniform electric field cage for the TPCs at NA61/SHINE is made of aluminized Mylar strips maintained at the appropriate electric potential via a voltage divider. Measurements of the x and z coordinates of the particle track is provided by the induced charge on the top pad plane, while the y-coordinate is determined from the arrival times of the drift electrons on the pad plane. Technical parameters of each of the TPCs are given in Tab. 3.1.

Each Main Time Projection Chamber (MTPC-L/R) features a readout surface measuring 390×390 cm^2, with an electric field cage height of approximately 110 cm. It is filled with a gas mixture of Ar/CO_2 in a 95/5 proportion. The track signals are captured by 25 proportional chambers per TPC, called sectors, providing up to 90 measured points and
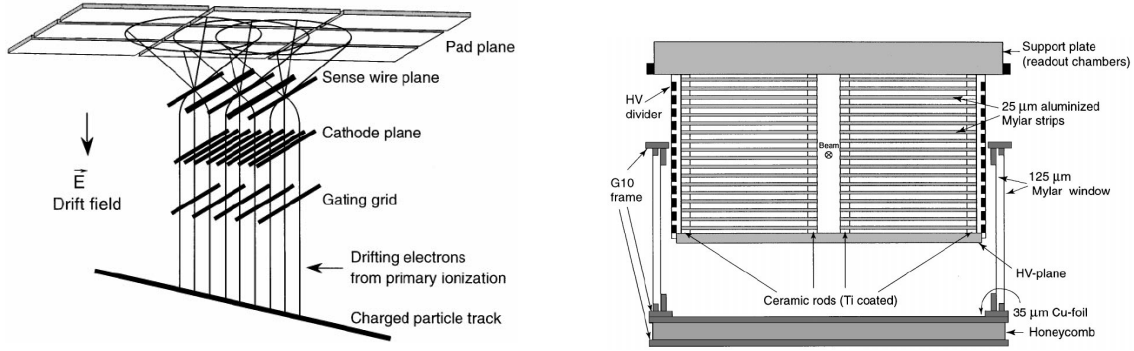
Figure 3.3.: An illustration of the working of a time Projection Chamber, with a vertically upward electron drift, is shown on the left. On the right is the schematic layout of the VTPC in the $x - y$ plane. The two field cages are seen on both sides of the beam (figures taken from [68]).

ionization samples on each particle trajectory. The precision of the average ionization energy loss measurement for a particle is around 4%.

The Vertex TPC comprises a gas box with a top surface area of $250 \times 200 \, \text{cm}^2$ and a depth of 67 cm. Field-cage structures are inserted to exclude a 120 cm region on either side of the beamline, where the particle density in Pb+Pb reactions is too high for trajectory resolution. A gas mixture of Ar/CO_2 in a 90/10 proportion is employed, and the readout is conducted by six proportional chambers on the top, providing up to 72 measurements and ionization samples on the particle trajectories. Further details on the Vertex and Main TPCs can be found in [68]. The VTPCs are placed inside two identical super-conducting dipole magnets of dimensions $L \times B = 570 \times 360 \, \text{cm}^2$. The maximum achievable combined bending power is 9 Tm at an operating current value of 5000 Amperes. The magnetic field for the standard configuration at a beam momentum $\geq 150A \, \text{GeV}/c$, is set to 1.5 T and 1.1 T in the first and the second super-conducting magnet respectively. The ratio of the two fields is maintained at a fixed value for lower beam momenta as well. The magnetic yokes are designed to maximize the opening angle on the downstream side, in the plane in which the charged particles are deflected.

A supplementary tracking device, the Gap-TPC, is strategically positioned on the beam-line between VTPC-1 and VTPC-2. This device is specifically placed to cover the gap between the sensitive volumes of the VTPCs, enhancing the precision of tracking. By incorporating additional points measured in the Gap-TPC, high-momentum tracks can be extrapolated more accurately back to the primary vertex. This proves particularly useful

in distinguishing particles originating from the primary vertex but measured solely in the MTPCs. The Gap-TPC aids in more effectively discerning such particles from conversion electrons that mimic high-momentum tracks outside the magnetic field.

3.4. Other Detectors

The NA61/SHINE facility utilizes a variety of detectors serving the requirement of the physics goals of the experiment. These detectors were not used in the pilot measurement discussed in this analysis, and hence, are briefly described in this section.

3.4.1. Beamline detectors

Apart from the upstream detectors mentioned in Sec. 3.3.1, the beamline can be equipped with additional beam counters depending on the measurement to be performed. These are the scintillators S2 and S3, positioned behind the BPD-2 and BPD-3 detectors. The thickness of S2 is $d_{S2} = 0.2\,\text{cm}$ and that of S3 is $d_{S3} = 0.5\,\text{cm}$. Moreover, the interactions of the beam in the target are signaled by placing scintillators S4 and S5 ($d_{S4} = d_{S5} = 0.5\,\text{cm}$), downstream of the target.

In addition to the square V1 detector, the beamline can be equipped with three veto scintillator detectors. These are called V0, V0^p, and the V1^p. The details of all the upstream detectors are given in Tab. 3.2.

Table 3.2.: Beam detector parameters: dimensions, inner hole diameter (ϕ_{in}), and its position relative to the target at $z = 0.0\,\text{m}$. The disc type detector dimensions are denoted by ϕ, where the first value is the outer diameter and the second value, is its thickness.

Detector	Dimensions (mm)	Hole (mm)	Position (z) (m)
S2	$\phi = 28 \times 2$	-	-8.81
S3	$\phi = 26 \times 5$	-	-0.77
S4	$\phi = 20 \times 5$	-	3.70
S5	$\phi = 20 \times 5$	-	15.61
V0	$\phi = 80 \times 10$	$\phi_{\text{in}} = 10$	-8.35
V0^p	$300 \times 300 \times 10$	$\phi_{\text{in}} = 20$	-8.19
V1^p	$300 \times 300 \times 10$	$\phi_{\text{in}} = 20$	-0.93

3.4.2. Time-of-Flight Scintillators

As particle identification solely based on energy loss measurement is not viable in the crossover region of the Bethe-Bloch curves, NA61/SHINE incorporates additional and independent identification through Time of Flight (*tof*) detectors. The ToF-L and ToF-R detectors, inherited from NA49, are utilized. To broaden the identification capabilities of NA61/SHINE to meet the requirements of neutrino physics, a new forward detector (ToF-F) was constructed and positioned between ToF-L/R, just behind the MTPCs. The determination of the particle's mass squared involves combining information from the particle's time of flight (*tof*) with the track length (l) and momentum (p) measured in the TPCs. This detector is not used in this analysis since the time resolution is not good enough for isotope identification based on the measured *tof* difference.

3.4.3. Projectile Spectator Detector

The Projectile Spectator Detector (PSD) is a modular lead/scintillator hadron calorimeter used for measuring projectile spectator energy in central nucleus-nucleus collisions at the trigger level. The accurate measurement of the energy carried by projectile spectators on an event-by-event basis allows for the extraction of the number of interacting nucleons from the projectile with a precision of one nucleon.

The PSD consists of a total of 44 modules, out of which 16 small modules of size $10 \times 10\,\mathrm{cm}^2$ and weighing $120\,\mathrm{kg}$ each, are placed in the center while the outer part consists of 28 large $20 \times 20\,\mathrm{cm}^2$ modules, each weighing $500\,\mathrm{kg}$. Each module comprises 60 pairs of lead plates and scintillator tiles arranged alternately, with thicknesses of $1.6\,\mathrm{cm}$ and $4\,\mathrm{cm}$, respectively. The plates are stacked together and secured with $0.5\,\mathrm{mm}$ thick steel tape, enclosed within a box made of $0.5\,\mathrm{mm}$ thick steel. The overall length of the modules corresponds to 5.7 nuclear interaction lengths. The PSD was not used in the pilot measurement, but is foreseen for future fragmentation runs, to mainly detect neutrons.

3.5. Reconstruction using Shine $\overline{\text{Off}}\underline{\text{line}}$

The raw detector data, such as counts from the analog-to-digital and time-to-digital converters, are transformed to a structured data format used for further analysis using the software called Shine $\overline{\text{Off}}\underline{\text{line}}$ [69]. It is a C++ based software routine adapted from
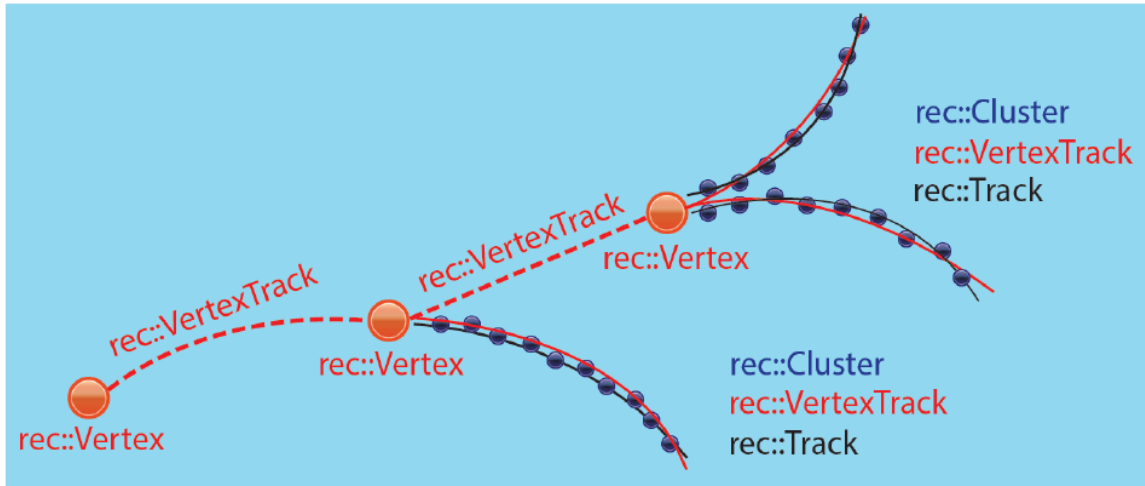
Figure 3.4.: Graphical representation of the objects stored in a SHOE file structure (adopted from [69]).

the Offline Software Framework of the Pierre Auger Observatory, used for reconstruction, calibration and analysis of the data.

A brief description of data reconstruction is as follows: Raw data from the TPC pad-time bin is *clusterized* to output a set of three-dimensional reconstructed points called *clusters*. These points are then associated to a charged particle, grouped, and perform to fit to each group to make a track, called a Local Track, corresponding to a TPC volume. Next, the *Local Tracks* are extrapolated to adjacent chambers to select and obtain the best matching track in this chamber volume, to merge into a single track across the two chambers, called a *Global Track*. Finally, a vertex finding algorithm is implemented to determine the origins of the tracks. One of the algorithms is called the Main Vertex Finder and Fitter, which identifies tracks originating in the beam-target interaction to determine the main vertex. These tracks are termed Vertex Tracks, and are fundamentally important objects for further analysis. Higher-level raw and reconstructed data, such as these objects, are stored in SHINE Offline Event (SHOE) files. An illustration of the objects stored in it is shown in Fig. 3.4. Complete details of the reconstruction procedure are described comprehensively in Ref. [70].

3.6. Detector Upgrade

The NA61/SHINE detector systems were upgraded and commissioned during the Long Shutdown 2 (LS2) at CERN between 2019 and 2021. The main aim of this hardware upgrade
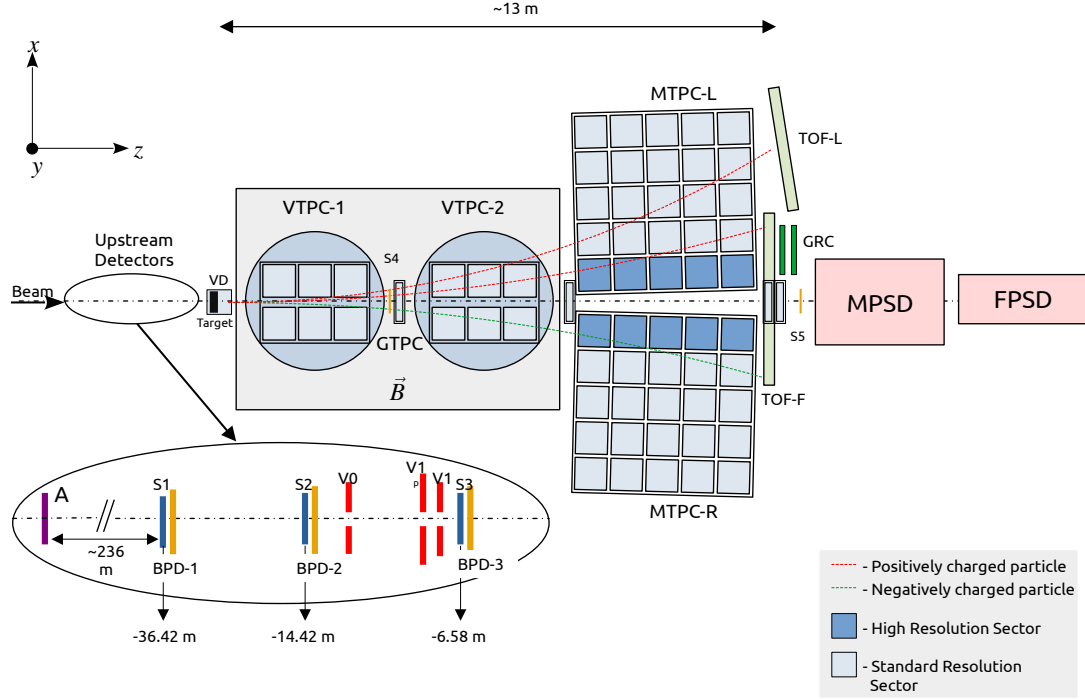
Figure 3.5.: The schematic of the NA61/SHINE detector systems post the LS2 hardware upgrade.

was to increase the data-taking rate from 80 Hz to 1000 Hz, to meet the requirements of the charm and neutrino physics programs conducted at NA61/SHINE. This required a change of readout electronics of the TPCs, a completely new Data Acquisition (DAQ) system, and a new trigger system. A detailed overview of NA61/SHINE DAQ can be found in [71]. The maximum data-taking rate achieved post the upgrade reached 1.6 kHz, well beyond the expected rate of 1 kHz, enabling high-statistics runs in the future (complete details are given in Ref. [72]).

The enhancements to the NA61/SHINE detector encompassed the following modifications:

1. Construction of new Beam Position Detectors (BPD), replacing the old MWPC with Silicon Strip Matrix. The active area of the matrix is $97 \times 97 \, \text{mm}^2$ with a $190 \mu m$ pitch [73].

2. Replacement of the old TPC readout electronics with the new Front End Cards (FEC) adopted from ALICE [73].

3. Construction of a new Vertex Detector using ALPIDE pixel sensors for the detection of neutral D meson [73].

4. Construction of new ToF detectors for particle identification at mid-rapidity, based on Multi-gap Resistive Plate Chamber (MRPC) technology and time resolution $\approx 50\,\text{ps}$ [73].

5. Development of the Geometry Reference Chamber (GRC) for dedicated in-situ drift velocity measurements in the TPCs. The GRC consists of a pair of Cartesian readout MWPCs, with a granularity of 6 mm in the drift direction (see Ref. [74] for complete details).

6. The existing Projectile Spectator Detector (PSD) was replaced with two calorimeters, namely the Main PSD (MPSD) consisting a total of 32 modules, and the Forward PSD (FPSD) placed further downstream, consisting of 9 modules. The purpose of this upgrade was to overcome the issue with increased radiation hardness and readout rate of heavy ion beams during the post LS2 runs.

7. Implementation of a new Trigger and Data Acquisition (TDAQ) system that is fully scalable, allowing seamless integration of new detectors—a capability absent in the old DAQ system.

By the end of 2021, the new readout electronics, based on the former ALICE TPC readout, were successfully incorporated into the two Vertex TPCs and subjected to successful testing. After this initial phase, the upgrade initiative persisted into 2022, involving integrating the new readout system into the two Main TPCs, the GTPC, and the three Forward TPCs (FTPC-1/2/3). Total number of FECs installed on the TPCs is given in Tab. 3.3. Only one outermost upstream sector each of the MTPC-L and MTPC-R could not be fully equipped due to component shortages. However, this constitutes a minor region of acceptance and does not impact the physics performance in subsequent runs. Since these printed circuit boards (PCBs) differ in shape and connector types from those previously used in NA61/SHINE, a considerable amount of work with adapters, preparation of the connector cables, and re-designing the mechanical suspension was performed. A complete ready-to-install Front End Card connected with kaptons (flexible polyimide) is shown in Fig. 3.6. The entire set of TPCs was readied for data collection during the proton run scheduled in
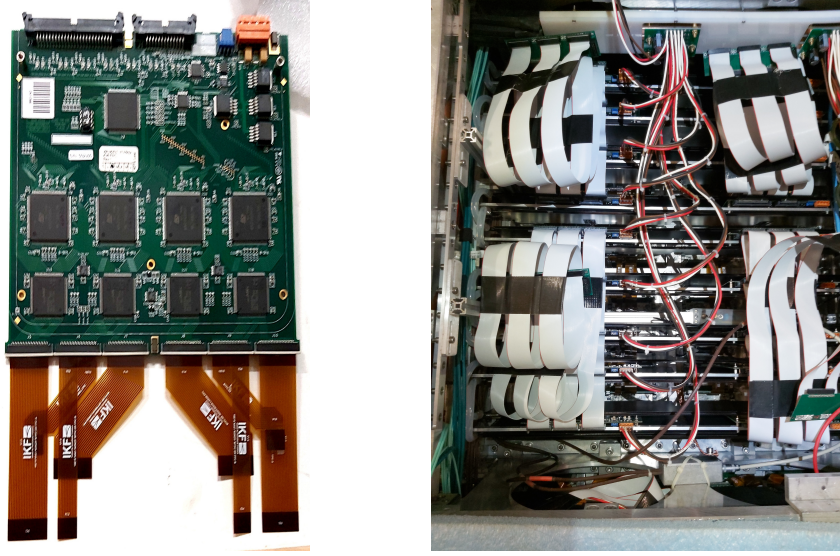
Figure 3.6.: *Left:* An ALICE Front End Card connected with flexible polyimide ready to be installed in a TPC sector. *Right:* A MTPC-L Standard Resolution (SR) sector is completely equipped with 18 FECs, with the power cables connected to the Low Voltage bus bar of the sector on the top.

July 2022. A functional MTPC-L sector installed with the new electronic boards connected to the low voltage power supply is shown in Fig. 3.6.

Key improvements with the newer FECs compared to the existing electronics are the higher digitization rate boosting the readout rate by a factor of 10, larger dynamic range due to 10 bit ADC, and improved electronic noise from $1000e_{rms}$ to $< 1000e_{rms}$. The major improvement in the raw ADC distribution in the TPCs is clearly seen in Fig. 3.8. The noise levels in the individual TPC sectors have significantly reduced, leading to better particle track resolution in the VTPCs and the MTPC, as well. During test runs, event

Table 3.3.: Distribution of Front-End Cards (FECs), Readout Control Unit (RCUs) and Common Readout Receiver Cards (C-RORCs) in Readout Nodes at NA61/SHINE experiment [75].

	VTPC-1,2	MTPC-HR	MTPC-SR	GTPC	FTPC-1	FTPC-2,3	Total
FECs	432	270	720	8	12	36	1478
RCUs	24	20	40	1	1	2	88
C-RORCs	4	4	7		1		16

Figure 3.7.: The author during hardware shifts for MTPC FEC installation (left) and the works on the beamline A-detector cable inside the tunnel (right).

rates reached up to 1.9 kHz, and the observed data taking rates during data collection in the p-run were up to 1.6 kHz, more than the upgrade goal of 1 kHz.

Moreover, the readiness of the A-detector, was checked during a two-day Machine Development (MD) interval at CERN in September 2022. During this period, the ethernet cable for the A-detector was placed inside the beamline, to enable smooth connection during future fragmentation runs. Smooth functioning of the A-detector is crucial for accurate time-of-flight measurement of the beam ions as emphasized in Chs. 4 and 5. The contribution of the author during the hardware upgrade is shown in Fig. 3.7).

Run 30580 Event 304   2017-08-23T23:43:52Z (UTC), 1187567050 (GPS), Unix:1503531832s

Pre-upgrade 2017 p+C Event
(noise-dominated)

Run 40867 Event 194954   2022-07-26T10:54:32.430888448Z (UTC), 1342868090:4.30888e+08 (GPS), Unix:1658832872s,4.30888e+08ns

Post-upgrade 2022 p+T2K Event
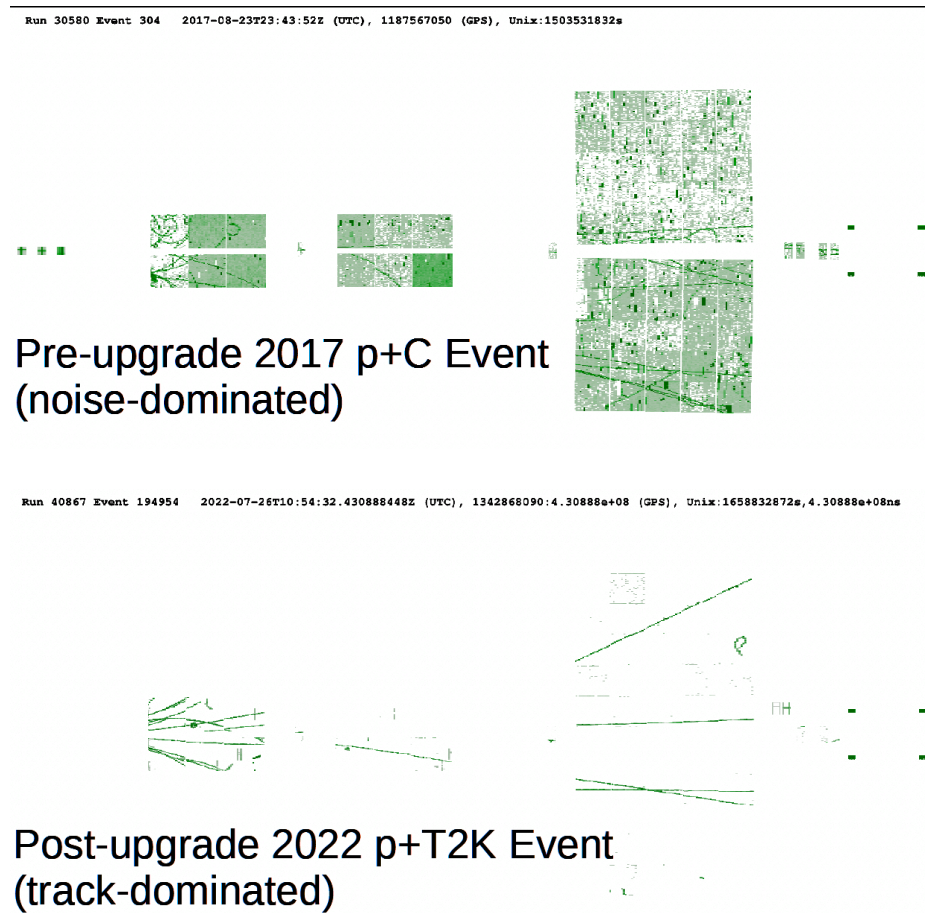(track-dominated)

Figure 3.8.: Raw ADC distribution of the TPCs, where the top plot shows an event in p+C interaction at 120 GeV/c, before the upgrade while the bottom plot shows an event recorded during the 31 GeV/c proton run on the graphite target similar to the one used in T2K, after the NA61/SHINE detector upgrade. Figure taken from Ref. [72].

4. Pilot Run on Nuclear Fragmentation

In order to study the feasibility of performing nuclear fragmentation measurements at SPS energies, a pilot run was conducted at the NA61/SHINE facility in December 2018 [76]. The primary objective of this run was to examine the production of light secondary nuclear fragments, like lithium (Li), beryllium (Be), and boron (B) through spallation of intermediate-mass nuclei like ^{12}C on a proton target, at beam momentum $p > 10A\,\text{GeV}/c$. In this chapter, the details of the run parameters, such as the ion beam, trigger settings, detector setup and the targets are discussed.

4.1. Secondary Ion Beam

Production of secondary ion beams at CERN for measuring nuclear fragmentation cross-sections was first reported in Ref. [77]. The desired projectile for the pilot run was the ^{12}C nucleus. As described in Sec. 3.2, the secondary ion beam was created by fragmenting a high-intensity ($\sim 10^8$ ions/spill), fully ionized lead ^{208}Pb beam from the SPS onto the beryllium target (T2). Two sets of data were recorded for the pilot run in which the beamline spectrometers were tuned to select particles with rigidity $R = 28\,\text{GV}/c$, and $R = 27\,\text{GV}/c$ with momentum per nucleon $p_A = 14A\,\text{GeV}/c$ and $p_A = 13.5A\,\text{GeV}/c$, respectively. The $28\,\text{GV}/c$ secondary beam was produced with a 30 cm plate while the beam at $27\,\text{GV}/c$ was produced from a 16 cm plate. The beam tune rigidity value was chosen to satisfy two basic conditions. First, the primary requirement of this measurement is to meet the energy scale $> 10A\,\text{GeV}/c$ where the fragmentation cross section becomes independent of the momentum. Second, the *tof* resolution measured from the A-S1 system deteriorates with increasing beam momentum, hindering separation of isotopes. Therefore, the SPS was operated at its stable lower limit for ions beams. Additional preliminary details regarding the two datasets are tabulated in Tab. 4.1.
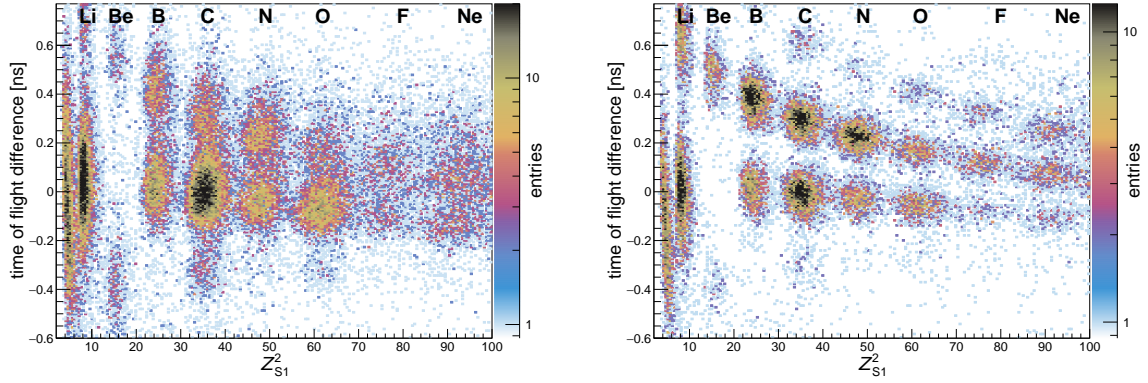
Figure 4.1.: The beam composition at $p = 13.5A\,\mathrm{GeV}/c$ (left) and $p = 14.0A\,\mathrm{GeV}/c$ (right) recorded during the pilot run. The squared charge from the $\mathrm{d}E/\mathrm{d}x$ signal in S1 is shown on the x-axis, and the difference in the time-of-flight Δt of the various nuclei as measured by the A-S1 system, on the y-axis.

The composition of the beam for the two different momenta, namely, $13.5A\,\mathrm{GeV}/c$ and $14.0A\,\mathrm{GeV}/c$ are shown in Fig. 4.1. The y-axis is the difference in the *tof* between two isotopes denoted as Δt. Using the formula for *tof* given in Eq. (3.3), an analytical expression for Δt corresponding to the difference in *tof* for two nuclei of mass numbers A_1 and A_2 can be written as,

$$\Delta t = \frac{L}{c}\left(\sqrt{1 + \left(\frac{A_1 u}{RZ}\right)^2} - \sqrt{1 + \left(\frac{A_2 u}{RZ}\right)^2} \right) \tag{4.1}$$

The time of flight difference Δt depends on the masses of the two isotopes. For example, in the case of the two carbon isotopes ^{13}C and ^{12}C, the Δt calculated using Eq. (4.1) is ~ 0.3 ns. This value is in good agreement with the measured Δt as seen in Fig. 5.1. The spectrometer magnets were fine-tuned to select $A/Z = 2$ nuclei. The setting with $R = 27$ GV/c and 16 cm long Be target maximized the yield of the desired ^{12}C nucleus, produced in the Pb+Be interactions.

The process of fragmentation inherently introduces a spread σ_p, in the longitudinal component of the particle momentum p along the z-axis. It is attributed to the quantum effect of the Fermi motion of the resultant nuclear fragments, wherein they possess a momentum distribution $\exp\left(\frac{-p^2}{2\sigma_p^2}\right)$ in their rest frame (see Sec. 2.5). Nuclear Fermi motion can distribute the longitudinal momentum of the fragments nearly up to 5%, which is much larger than the nominal beam momentum acceptance. This effect combined with the momentum acceptance of the beam-line enables neighboring isotopes and elements with mass-to-charge similar to $A/Z = 2$ to pass the rigidity selection of the beam-line

	Beam momentum	
	$14A\,\text{GeV}/c$	$13.5A\,\text{GeV}/c$
Run number:	39327-39346	39350-39422
T2 length	30 cm	16 cm
Rigidity	28 GV	27 GV
$\vec{B}$-field scaling factor	59%	59%
Target	Events recorded $\times 10^5$	
PE	1.3	5.5k
C	1.6	5.2k
OUT	1.0	1.2k
Total	3.9	11.9k

Table 4.1.: Run settings and number of beam trigger events recorded at two different beam momenta.

(see Sec. 3.2 for details). Furthermore, the momentum acceptance of the beam-line can be quantified as $\Delta p_z/p_z \approx 1\%$, and corresponds to the collimator slit opening. This quantity is a crucial parameter in determining the detector response model used for fitting the distribution of fragments in the MTPC in Sec. 5.4, and will be discussed in detail in the next chapter.

All nuclei with $A/Z = 2$ are in Fig. 4.1 placed at $\Delta t = 0$ line, whereas heavier fragments ($A/Z > 2$) and light fragments ($A/ < 2$) are above and below this line respectively. The enhanced yield of the desired nucleus ^{12}C is clearly seen on the left panel on Fig. 4.1. While the separation between the elements is evidently distinct, the isotope separation based on the Δt resolution for the $13.5A\,\text{GeV}/c$ dataset is weakly resolved.

As can be seen in Fig. 4.1, the ratio of ^{12}C to other carbon isotopes is approximately $1 : 1$. For a more efficient data-taking, the beam was adjusted by selecting particles with a different rigidity R, and a shorter primary T2 target, enhancing the ratio. However, as is also visible from the figures, this adjustment caused a slight deterioration of the resolution, particularly pertaining to Δt measurement. The time-of-flight resolution, $\sigma_{\Delta t}$ was determined by performing a fit to the 1-dimensional Δt distribution. In the case of $p_A = 14A\,\text{GeV}/c$, it was $\sigma_{\Delta t} \approx 32\,\text{ps}$, which worsened to $\sigma_{\Delta t} \approx 60\,\text{ps}$ for $p_A = 13.5A\,\text{GeV}/c$. Nevertheless, the separation was good enough for identification and separation of the carbon isotopes.

Table 4.2.: The number of secondary ions produced in ^{208}Pb+Be (T2 target) interaction as recorded during the pilot run, for the two momenta.

Z	A	Isotope	No. of particles	
			$14A\,\mathrm{GeV}/c$	$13.5A\,\mathrm{GeV}/c$
3	6	^{6}Li	4k	7k
	7	^{7}Li	1k	-
4	7	^{7}Be	0.1k	0.6k
	9	^{9}Be	0.8k	0.4k
5	10	^{10}B	4k	12k
	11	^{11}B	7k	6k
	11	^{11}C	4k	37k
6	12	^{12}C	98k	400k
	13	^{13}C	87k	94k
	14	^{14}C	8k	4k
7	14	^{14}N	5k	8k
	15	^{15}N	8k	6k
8	16	^{16}O	1k	3k
			$\Sigma \approx 228\mathrm{k}$	$\Sigma \approx 650\mathrm{k}$

4.2. Detector Setup

A subset of all the available NA61 detector systems as described in Sec. 3.3 and shown in Fig. 3.2 is used for the pilot measurement. The TPCs were operated at a lower voltage for measuring carbon and boron fragments, making it less sensitive to low-charge particles, like Li and Be. This reduces the selection efficiency of such particles, as will be discussed briefly in Sec. 5.6. In the following sections, the trigger logic, and targets used in this analysis are discussed.

4.2.1. Trigger settings

Fast triggering signals from the beam line scintillator S1 and the veto detector V1 are used in anti-coincidence to form the trigger logic, and instruct the DAQ to record the data. Two triggers were defined for this measurement, namely the all beam trigger T1, and the carbon trigger T3 set to select $Z^2 = 36$ particles, written as,

$$\mathrm{T1} = S1_{\mathrm{all}} \wedge \overline{\mathrm{V1}}$$

$$\mathrm{T3} = S1_{\mathrm{C}} \wedge \overline{\mathrm{V1}}.$$

Table 4.3.: Specifications of the targets used for the 2018 pilot run.

Quantity	Target name	
	PE	C
$L \times B \times H$	$2.5 \times 2.5 \times 1.5\,\text{cm}^3$	$2.5 \times 2.5 \times 1.0\,\text{cm}^3$
Density (ρ)	$0.924 \pm 0.001\,\text{g/cm}^3$	$1.84 \pm 0.01\,\text{g/cm}^3$
Molar Mass (M)	14	12

The T1 selects all the beam particles present in the beam composition, whereas the T3 utilizes the Z^2 equivalent dE/dx signal from S1 to perform an online selection of carbon nucleus in the beam. Only T3 events were considered for this analysis, while the T1 and T3 events are utilized to make auxillary measurements of nuclei other than ^{12}C, as will be discussed in Sec. 6.3.2.

4.2.2. Targets

Furthermore, to measure the production of lighter fragments in ^{12}C+p interactions, a polyethylene (CH$_2$, hereafter PE) and graphite block (hereafter C) were used to emulate a proton target. While the C target was employed to take into consideration the ^{12}C+C interactions inside PE, the PE itself was used as the main proton target. Finally, to measure the interactions of the beam outside the target (OUT), e.g. in the beam counters upstream of the target and the TPC support structures downstream of the target, approximately 10% of the total events were recorded with an empty target holder.

During the course of the run, the target holder position was remotely controlled to alternate between the three target settings PE, C, and OUT (empty target holder), as shown in Fig. 4.2. Details of the target are given in Tab. 4.3.

Keeping in view the primary goal of the pilot run, which was to study the production of light nuclei like B from the fragmentation of a C beam, the Monte-Carlo simulations performed indicated that the optimal magnetic field of the superconducting vertex magnets (VTX1 & VTX2) should be set to 59% of the full field value [39]. This particular magnetic field scale factor reduced the secondary interactions of the resultant boron fragments in the detectors downstream of the target, such as the support structures of the Vertex-TPCs along the curved trajectory through the $\vec{B}$-field.

As can be seen from Tab. 4.2, the 14A GeV/c data comprise only 20% of the total number of ^{12}C projectiles. In the following, the focus is on the analysis of the larger data set taken
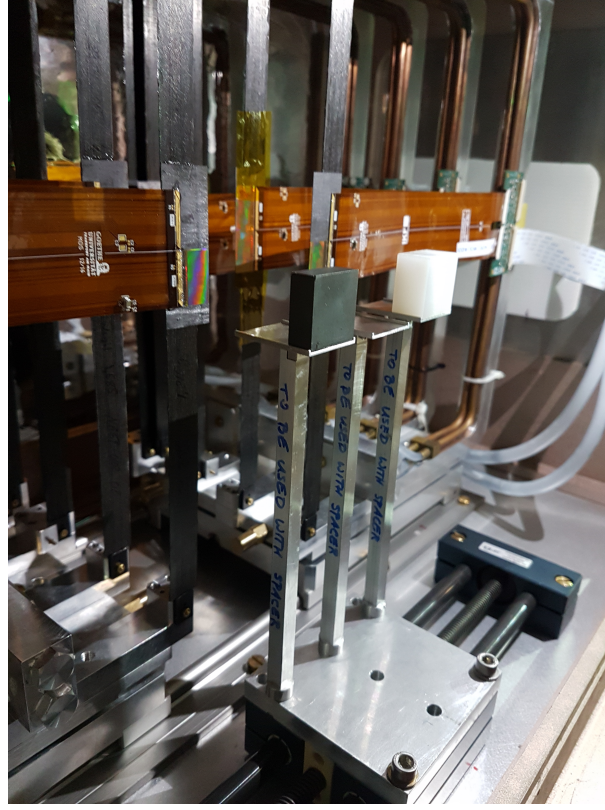
Figure 4.2.: The target holder with the two targets, polyethylene (PE) and graphite (C), used during the 2018 pilot run. The target holder is mounted onto a servo motor-controlled base which is used to place the desired target on the beamline This entire setup is enclosed within a He-filled box constituting the Vertex Detector as shown in the background.

after the beam re-tuning at $p_A = 13.5A\,\mathrm{GeV}/c$. Over the 3-day data-taking period, a total of 1.1×10^6 beam trigger events were recorded, including all three target settings. The raw data was reconstructed using the Shine $\overline{\mathrm{Off}\underline{\mathrm{line}}}$ Framework version v1r13p0. The EventBrowser view of one such reconstructed event is shown in Fig. 4.3. The red line corresponds to the Vertex Track reconstructed from the Main Vertex at target z. While the green lines represent local tracks. The timing information from the scintillators, the charge signals based on measured $\mathrm{d}E/\mathrm{d}x$ in the detectors, and the BPD and TPC positions are some of the many parameters that need to be calibrated for further analysis. The calibration procedure is beyond the scope of this work. Nevertheless, it is discussed in comprehensive details in Ref. [39].

Key parameters enabling precise measurement required for this analysis, essentially depend on two criteria: first, accurate identification and selection of the beam particle

incident on the target, called upstream selection, and second, identification of nuclear fragments in MTPC-L, called downstream selection.

Beam particle identification requires two inputs:

1. $dE/dx \propto Z^2$: the charge of the beam is determined from the energy deposit signal in the scintillator counter S1 (online selection)

2. *tof* $\propto (A/Z)$: time-of-flight measured between the A-detector and the S1 helps to identify the isotope.

Downstream selection requirements:

1. Energy deposit, $dE/dx \propto Z^2$ in the TPC volumes determines the charge of the fragment track.

2. Deflection of charged fragments along the x-direction in the magnetic field, relative to the beam

The details of these selections relevant for the measurement will be discussed in the next chapter.
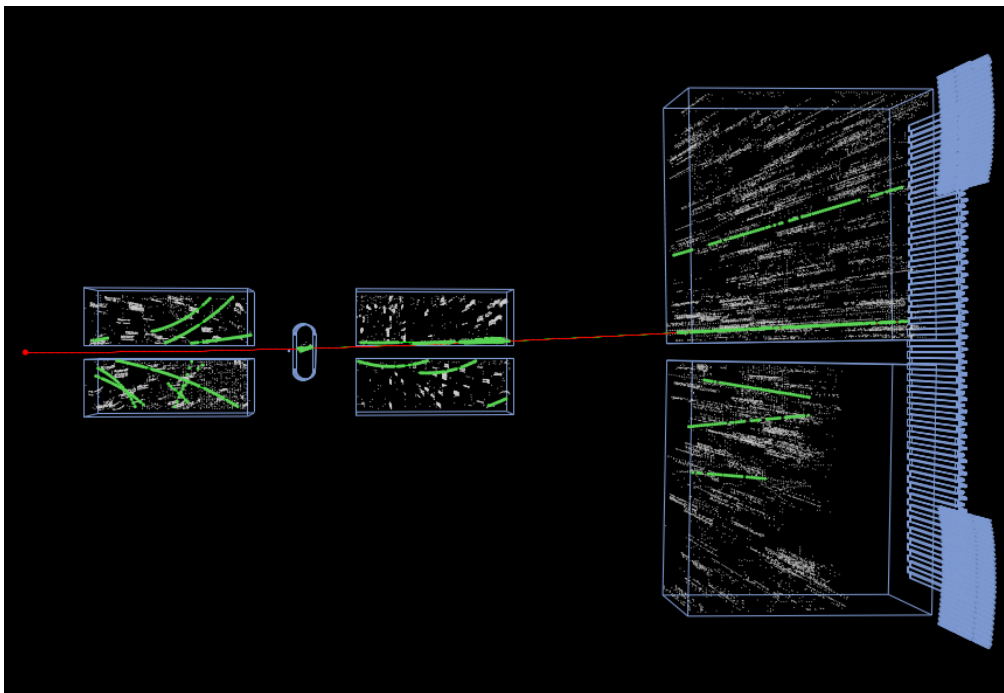
Figure 4.3.: SHINE *eventBrowser* top view of an event from the pilot run in the $x - z$ plane, with the VTPCs, GTPC, the MTPCs, and the ToF wall outlined in blue. A reconstructed vertex track orginating from the target is shown in red, while the clusters on local tracks for each TPC are shown in green. Unmatched charge clusters are shown as white dots.

5. Measurement of Interaction Probabilities

In a fixed target experiment with a composite beam containing more than one type of nucleus, the identification of a particular nucleus as the beam particle is crucial to study its fragmentation. The second important piece of information is identifying the nuclear fragments produced from the beam-target interaction. The details of the beam particle and fragment tracks selection are described in this chapter. Moreover, the details of the fit performed to the distribution of fragments in the MTPC is also discussed in details.

Data selection entails the event-level and track-level selection of the data used for our analysis. They are classified into two main categories: upstream cuts, focusing on beam-particle identification, and downstream cuts which pertain to the identification and selection of nuclear fragments in the TPCs, relevant to our study.

5.1. Upstream Selection of the Beam Particle

The two key inputs for accurate and efficient beam particle selection were introduced in Sec. 3.3. In this section, these inputs are discussed comprehensively, describing the selection of ^{12}C, optimization of the cut, estimation of the uncertainties, and finally giving and overview of the quality cuts performed.

5.1.1. Projectile Isotope Selection

For the upstream selection of the beam, we operate only with triggered events shown in Fig. 5.1.

In order to select ^{12}C as the primary beam particle, and to estimate the number of events corresponding to various isotopes present in the beam composition, a Poisson log-likelihood fit is performed on the 2-dimensional *tof* vs. Z^2 distribution of the upstream
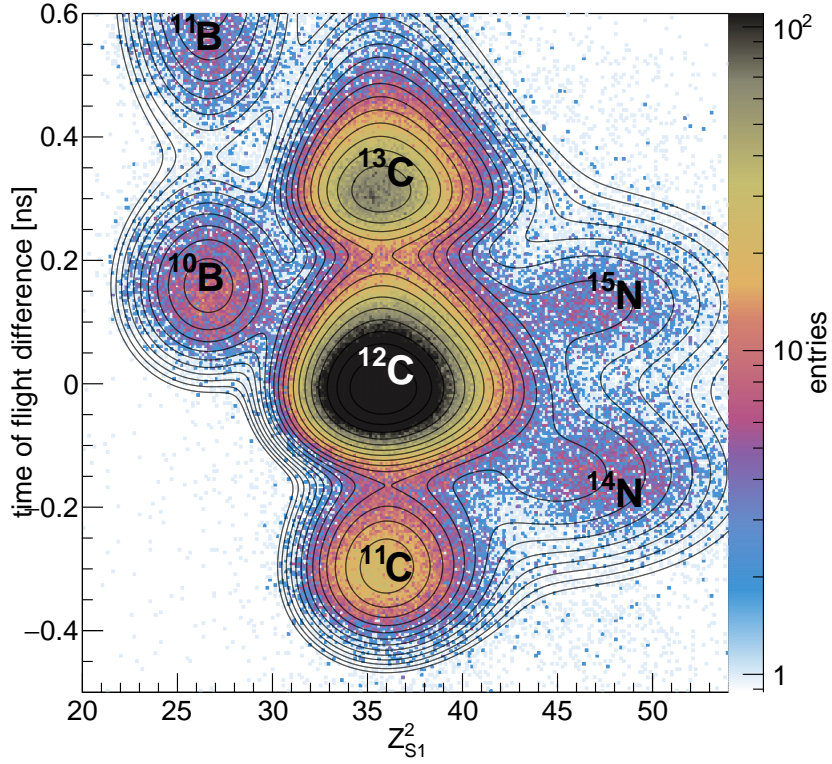
Figure 5.1.: Upstream fragments Δt vs. Z_{S1}^2 distribution of the T3 data. The 2-dimensional function fit to data is shown as contour lines.

fragments constituting the beam. Subsequently, an optimal selection criterion is established based on the fit results. This criterion aims to maximize the count of ^{12}C events while simultaneously minimizing the presence of impurity isotopes neighboring ^{12}C within the selected data.

The shape of the Δt vs Z^2 distribution not uniform across all the isotope peaks as seen in Fig. 5.1, but has distinct tails along both the axis. This distorted drop-shape is clearly visible for the carbon isotopes. Therefore, the fit model employed to describe the upstream fragment distribution is a 2-dimensional elliptical Gaussian function with exponential tails. This function can be mathematically expressed using two 1-dimensional elliptical Gaussian distribution convolved with an exponential to model the characteristic tail. Let $f(x)$ and $g(y)$ be the two model functions along the x and y axes corresponding to the Z^2 and Δt axes, respectively. Then, the total function $F(x, y)$ to describe an isotope peak, can be written as,

$$F(x, y) = N \left(f(x) \cdot g(y) \right), \tag{5.1}$$

where N is the normalization of the peaks. It quantifies the number of events corresponding to every isotope in the data. Furthermore, the independent functions $f(x)$ and $g(y)$ resulting from the convolution of a Gaussian with exponential tail, can be separately written as,

$$f(x) = \frac{1}{2} \left[\exp \left(-\lambda_x \left(x - \mu_x - \frac{\sigma_x^2 \lambda_x}{2} \right) \right) (1 + \text{erf}(a(x))) \right], \tag{5.2a}$$

$$g(y) = \frac{1}{2} \left[\exp \left(-\lambda_y \left(y - \mu_y - \frac{\sigma_y^2 \lambda_y}{2} \right) \right) (1 + \text{erf}(b(y))) \right], \tag{5.2b}$$

where μ_x is the mean of the squared charge Z^2 as measured in S1, and μ_y is the mean of the parameter Δt, measured between the A and the S1 scintillators. The parameter σ_x and σ_y correspond to the widths of the Gaussian function whereas λ_x and λ_y characterizes the exponential tails, along the x (Z^2) and y (Δt) axes, respectively. The arguments of the Error functions, $a(x)$ and $b(y)$, in the equations above are functions of the parameters σ and λ, and are written as,

$$a(x) = \left(\frac{x - \mu_x - \sigma_x^2 \lambda_x}{\sigma_x \sqrt{2}} \right), \tag{5.3a}$$

$$b(y) = \left(\frac{y - \mu_y - \sigma_y^2 \lambda_y}{\sigma_y \sqrt{2}} \right), \tag{5.3b}$$

The fit is performed over the range $20.0 \leqslant Z_{\text{S1}}^2 \leqslant 54.0$ and $(-0.5 \leqslant \Delta t \leqslant 0.7)$ ns. The resultant fit describing the data is shown in Fig. 5.1. The goal of the fit is to maximize the selection efficiency of ^{12}C thereby minimizing the statistical uncertainty and the systematics due to the presence of neighboring nuclei in the fragment distribution. A numerically iterative procedure is undertaken to determine the optimal cut to select ^{12}C as the primary beam particle, for further analysis. Let us define the relative fraction of the ^{12}C peak as the ratio of a set threshold value f_{th} to the maximum of the ^{12}C peak $f_{12\text{C}}$, determined from the fit. This is represented visually in Fig. 5.2. This ratio is denoted by k. The iterative procedure is as follows: we start by selecting upstream events at the ratio

Table 5.1.: Parameter values used to select primary ^{12}C nucleus to make the optimal cut at $k \approx 10\%$, as described in the text.

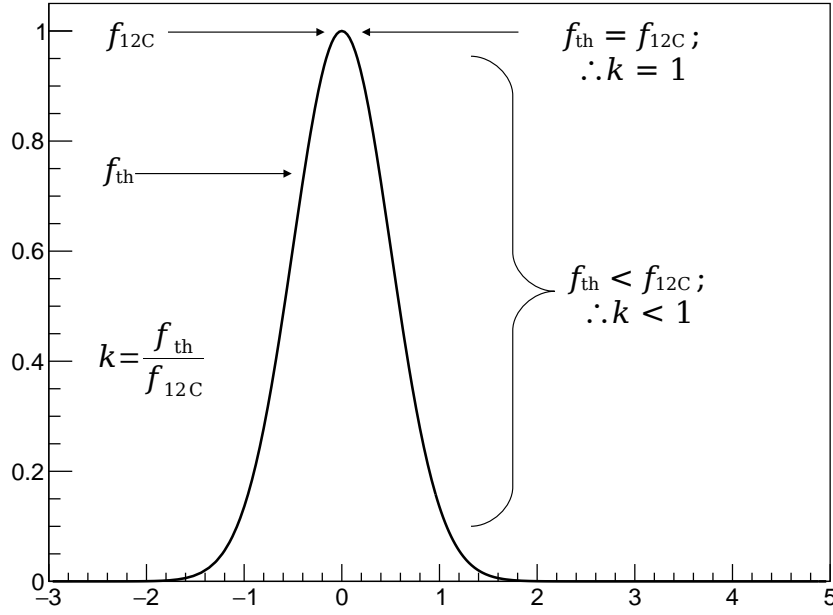| μ_x	σ_x	λ_x	μ_y	σ_y	λ_y
35.00	1.78	0.71	-0.04	0.04	19.83

Figure 5.2.: The relative fraction of the ^{12}C peak used in the iterative procedure to determine the optimal cut.

$k = 1$. This simply corresponds to the pure ^{12}C peak, with a very small number of beam particles. Following which, we determine the number of nuclear fragments produced in beam-target interactions (N) by counting the fragment tracks in the MTPC. In the case of production of ^{11}C, number of tracks N corresponding to it in the MTPC-L are measured. Next, the relative uncertainty $\sigma(N)/N$ on the quantity N is computed. At the ratio $k = 1$, the relative uncertainty is dominated by the statistical uncertainty $\sigma_{\text{stat.}}$ owing to a few events. This procedure is repeated for decreasing values of k, which means moving farther away from the ^{12}C peak and widening the cut to gather more statistics. As k decreases, the systematic uncertainty on N, denoted as $\sigma_{\text{syst.}}$ rises due to the contribution from the feed-down of the neighboring isotopes. The rising relative fractions of impurity nuclei with decreasing k is shown in Fig. 5.4. The optimum is defined as the value of k, for which the relative uncertainty on N is minimum. This corresponds to $k \approx 10\%$ for all the isotope production studies undertaken in this work. The total efficiency of this cut to select ^{12}C is 66%. It is shown as a black contour in Fig. 5.3.

The fraction of neighboring impurity nuclei present in the optimized cut is determined from the integral of the extrapolated fit peak corresponding to each nucleus neighboring ^{12}C. The relative fraction is plot against k as shown in Fig. 5.4. The red dashed vertical
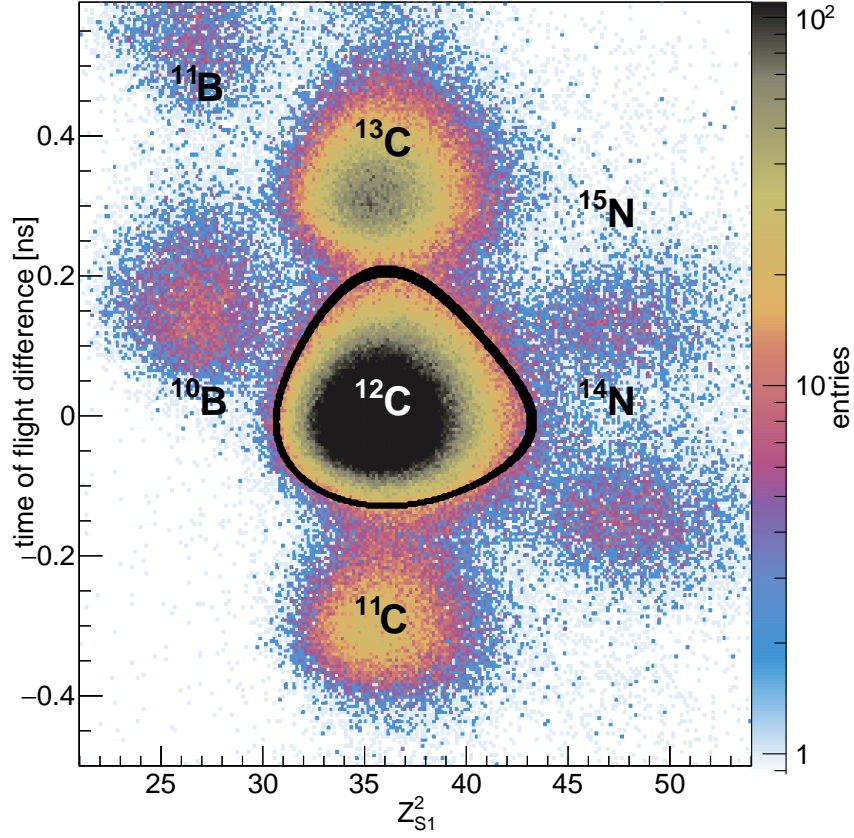
Figure 5.3.: The Δt vs. Z_{S1}^2 plot of the T3 data showing the primary triggered nucleus ^{12}C along with the neighboring isotopes passing the momentum acceptance of the beam-line. Optimal selection of ^{12}C as beam nucleus is shown by the black contour.

line represents the optimal cut value for the selection of ^{12}C. The largest contribution comes from the ^{11}C, due to its exponential along the Δt axis, followed by ^{14}N. The relative fractions of these nuclei will be used to correct the measured cross section, as will be described in Sec. 6.6.2.

5.1.2. Upstream Quality Selection

In addition to the isotope selection procedure detailed above, we impose further cuts as part of the beam particle selection criteria on an event-by-event basis. These cuts are listed in Tab. 5.2 along with their corresponding efficiencies for the three data sets, PE, C, and OUT. The online carbon trigger is tuned to select $Z^2 = 36$ particles based on their energy deposit in the S1 scintillator. The $t_{(A1,A2)}$ and $a_{(A1,A2)}$ cuts select events such that
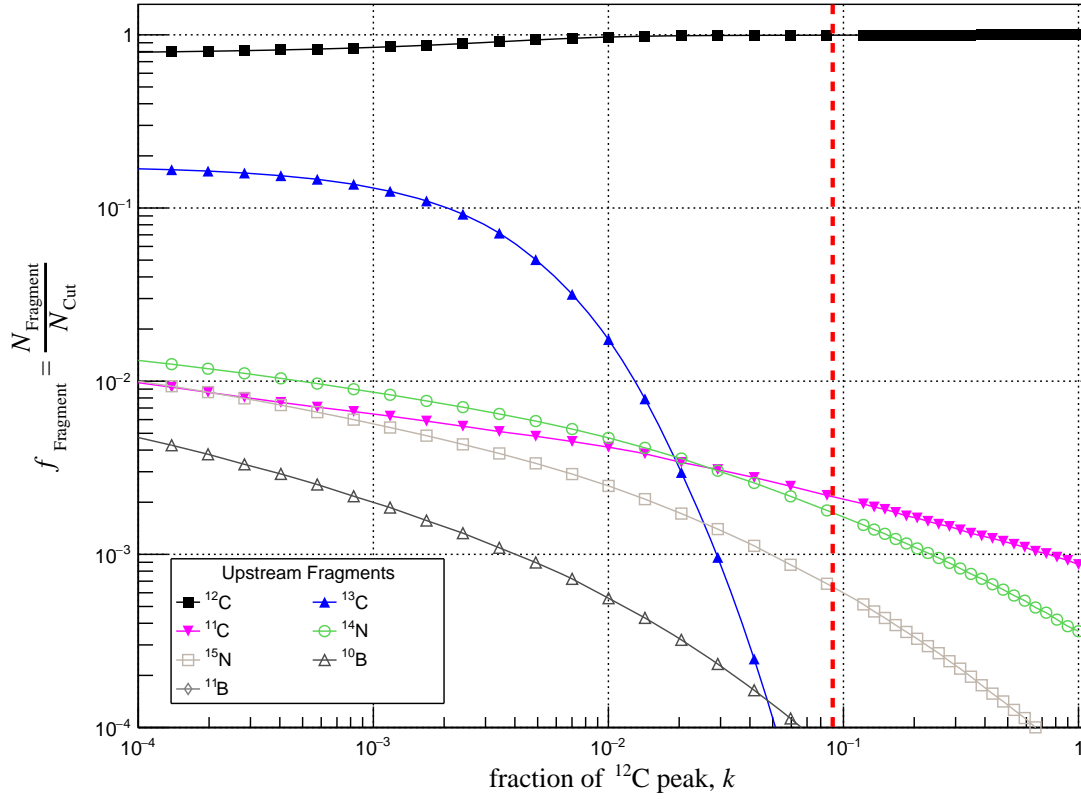
Figure 5.4.: Selected projectile isotope fractions as a function of offline contour-level cut. The optimal cut for ^{12}C selection is shown as vertical red dashed line at abcissa$\approx$ 0.1.

the time and signal amplitude as measured by the two PMTs A1 and A2, of the A-detector, are within the specified operational range of the scintillator.

BPD measurements primarily serve the purpose of determing the arrival direction of the incident beam particle. This is achieved by performing a least-squares fit using linear interpolation from the BPD measurement points in the $x-z$ and $y-z$ planes, and reconstructing the beam particle track. Therefore, position measurements of the beam from at least two BPDs are required to determine the direction. This information is further used to extrapolate the beam position as measured at the end of the MTPC-L, and is crucial in this analysis to determine the relative position of the fragments in the MTPC. This is ensured by the Two BPDs cut, which only selects events in which the beam signal is present in at least two of the three BPDs. Moreover, the beam position determined from BPD-1 measurement is used to calibrate the signal of the S1 detector. In the case where BPD-1 does not measure a signal, the signals from the other two BPDs can be used to make a linear extrapolation to the position of BPD-1, which can then be used for calibration. The

Table 5.2.: A list of upstream selection cuts applied to the calibrated data to select ^{12}C nuclei as the primary beam particle of interest.

Selection cut	Events (×10^3)			Effciency (%)	Comment
	PE	C	OUT		
13.5 A GeV/c	463	410	106	100.0	—
Carbon Trigger (T3)	372	331	85	80.3	Online $Z^2 = 36$ triggered events.
$t_{(A1,A2)}$	323	286	74	86.8	A-det timing information $t_A > 0$ ns
$a_{(A1,A2)}$	290	258	66	89.8	A-det amplitude, $100 \leqslant a_A \leqslant 1000$
Two BPDs	253	225	58	87.6	Beam signal present in at least 2 BPDs.
BPD-3 signal	235	210	54	93.0	Good BPD-3 measurement
WFA cut	230	205	53	97.6	Exclude off-time particles.
^{12}C cut	150	135	35	66.0	Offline selection of ^{12}C isotope.

BPD-3 x-y cut is used to filter out events based on the measured x-y position of the beam in BPD-3, to make sure that it hits the target. The aperture diameter for this selection is $\phi = 1.6$ cm. It is larger than the 1 cm central hole in V1, to account for the divergence of the beam. All events registered out of this region are rejected. Beam particles separation cut or WFA cut is used to prevent counting multiple tracks due to beam particles closely spaced in time. Particles arriving closer than $2\mu s$ are rejected (track separation in drift direction $|\Delta y| < 5.0$ cm). The timing information from the S1 scintillator is used for this cut.

5.2. Downstream Selection of Fragment Tracks in the MTPC

A large fraction of the ^{12}C beam particles incident on the thin target of thickness d_T pass without any interaction, while a small fraction of the beam interacts with the target, fragmenting to isotopes of lighter nuclei like B, Be, Li, etc. These charged fragments traverse through the superconducting magnets hosting the detectors, VTPC1 & VTPC2, and are deflected in the x-y plane finally depositing energy in the MTPC-L.

The beam-target interaction produces multiple particle tracks in the TPCs associated with every reconstructed event. Therefore, fragment tracks with the shortest distance to the extrapolated ^{12}C beam in the x and y directions are used for our analysis. The distance between a reconstructed track and the beam extrapolation in the x-direction is given by $\Delta x = x_{track} - x_{beam}$ and similarly in the y-direction by $\Delta y = y_{track} - y_{beam}$. Measurements of the beam positions determined from the BPD reconstruction are used to determine the x_{beam} and y_{beam}. The extrapolation through the vertex magnetic field is performed using

the *MagneticFieldTracker* module of Shine $\overline{\text{Off}}\underline{\text{line}}$. Reconstructed tracks satisfying the criteria $\Delta x < 30.0$ cm for MTPC, and $\Delta x < 20.0$ cm for VTPC-2 and GTPC are selected for the analysis.

More than one particle arriving within a short time window leads to pile-up in the detectors and can mimick beam particles. They are called off-time particles. Such particle tracks are distinguished by measuring the arrival times of the drifting electrons along the y-direction of the MTPC. They are rejected by placing a cut on the nominal beam y position at the end of the MTPC as, $|\Delta y| < 5$ cm. Moreover, the minimum requirement on the number of charge clusters produced by a track in the MTPC is $N_{\text{clusters}} > 70$. If N_{clusters} for a track in the VTPC-2 and the GTPC are more than 15 and 6 respectively, the dE/dx signal in the TPCs can be used for the re-interaction cut.

Carbon fragment tracks in the MTPC are selected by placing cuts on the squared-charge of the track determined from the energy loss dE/dx as, $31.0 < Z^2_{\text{MTPC}} < 44.0$. Similarly, the cuts for the boron fragments are $22.5 \leqslant Z^2_{\text{MTPC}} \leqslant 27.5$, for beryllium fragments are $16.0 \leqslant Z^2_{\text{MTPC}} \leqslant 18.0$, and for lithium fragments are $7.8 \leqslant Z^2_{\text{MTPC}} \leqslant 10.5$. These limits are set conservatively such as to reduce downstream interactions.

As GTPC and VTPC-2 preceed the Main-TPC, additional cuts are placed to reject boron isotopes produced from beam fragmentation between these detectors. We plot Z^2_{GTPC} vs. $Z^2_{\text{VTPC-2}}$ for tracks corresponding to boron fragments in MTPC-L. The dominant boron peak at $Z^2 \approx 25$ shows agreement between the measurements of all the three TPCs. Nevertheless, two additional peaks at $Z^2_{\text{GTPC}} > 32.0$ and $Z^2_{\text{VTPC-2}} > 31.0$ clearly indicate conversion of the ^{12}C beam between GTPC and VTPC-2, and VTPC-2 and MTPC-L, as indicated on the plot. These events are rejected for the boron analysis, by placing cuts on Z^2_{GTPC} and $Z^2_{\text{VTPC-2}}$ as shown by the dashed lines in Fig. 5.5.

Similar to the boron case, beam interaction events in the detectors for Be and Li, are rejected by placing appropriate cuts on Z^2_{GTPC} and $Z^2_{\text{VTPC-2}}$ as shown in Fig. 5.6 and Fig. 5.7.

5.3. Fragments in the MTPC

To accurately determine the number of fragments produced from beam-target interaction, it is important to understand the origin of the fragment track as measured in the MTPC. The final x position of the beam in at the end of the MTPC is denoted as x_{beam} and calculated as described in Sec. 5.2.
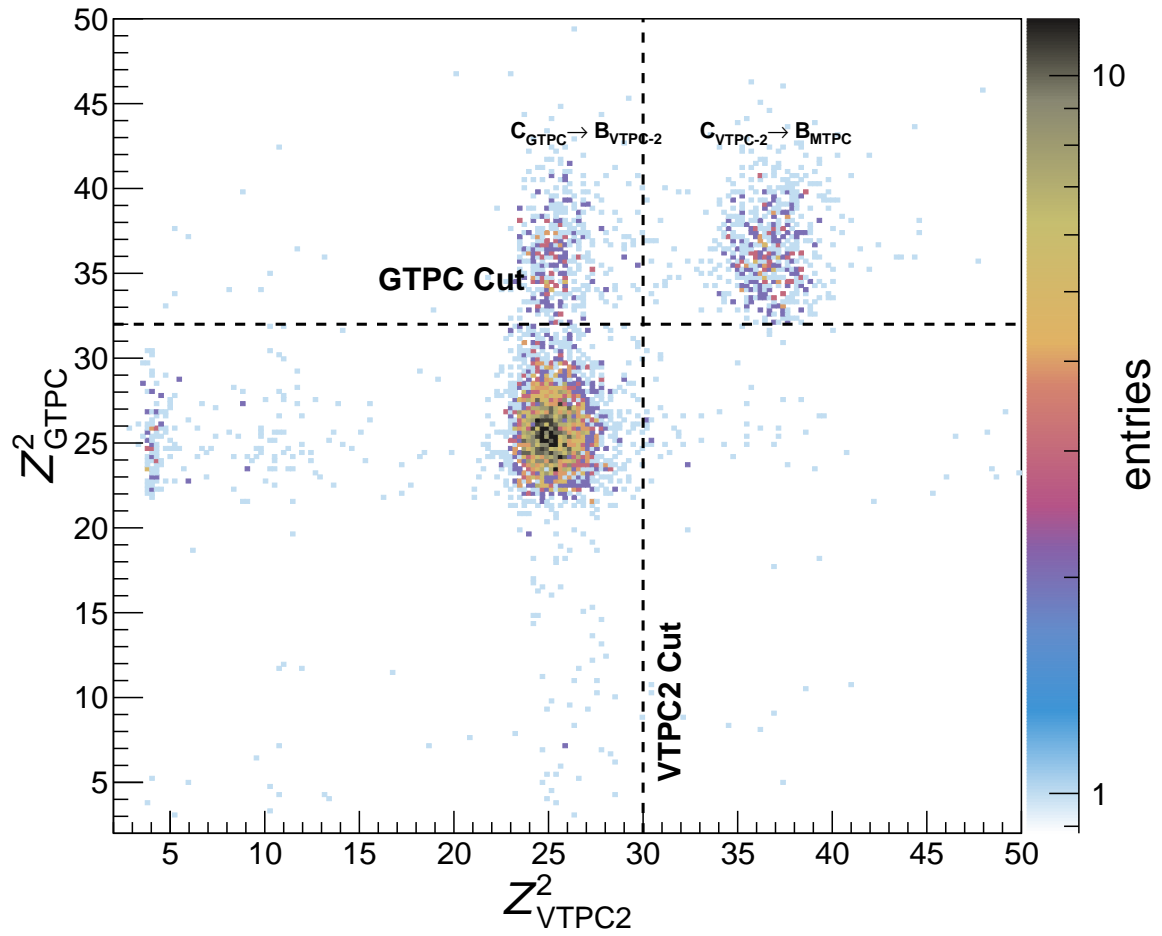
Figure 5.5.: Distriution of the squared charge Z^2 measured in the GTPC and VTPC-2 for tracks identified as boron in the MTPC-L. The Z^2 cut applied for boron analysis is shown by the dashed lines.
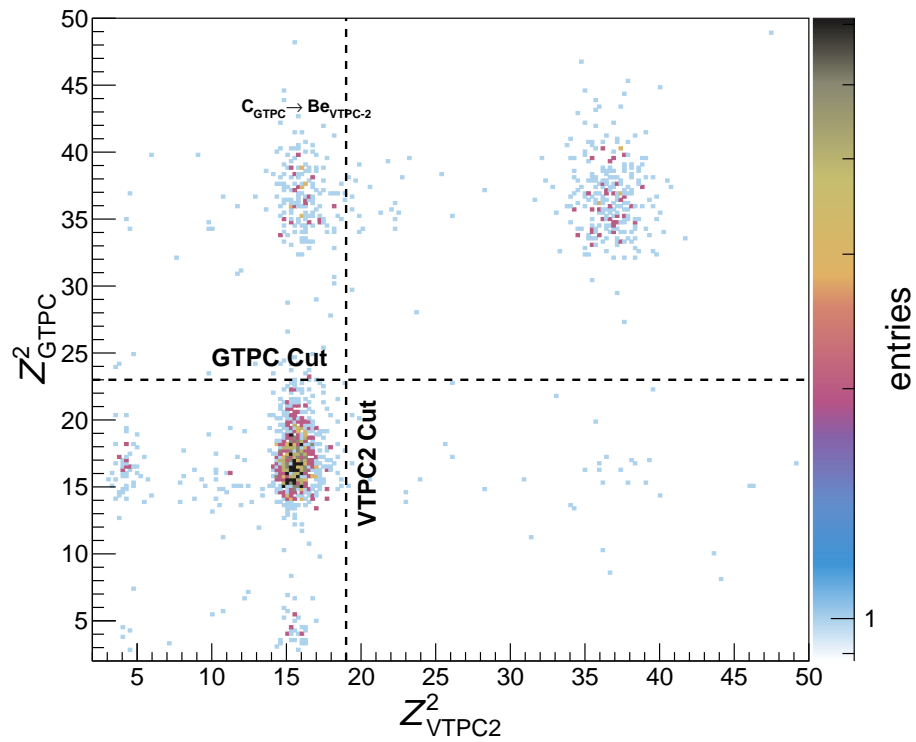
Figure 5.6.: Same as Fig. 5.5 for beryllium (left) events in the MTPC-L.
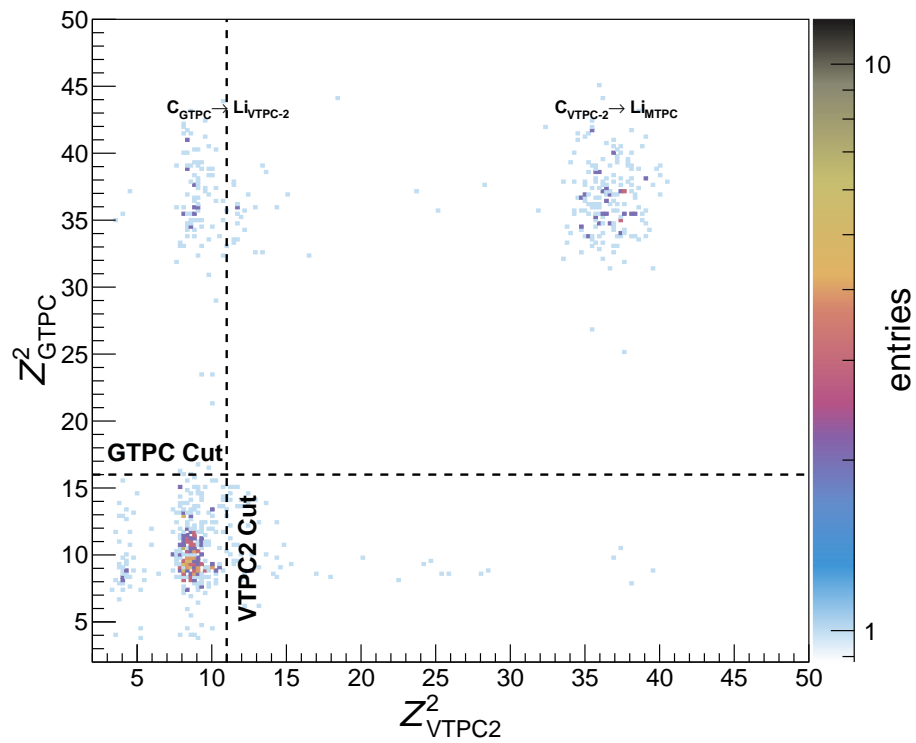

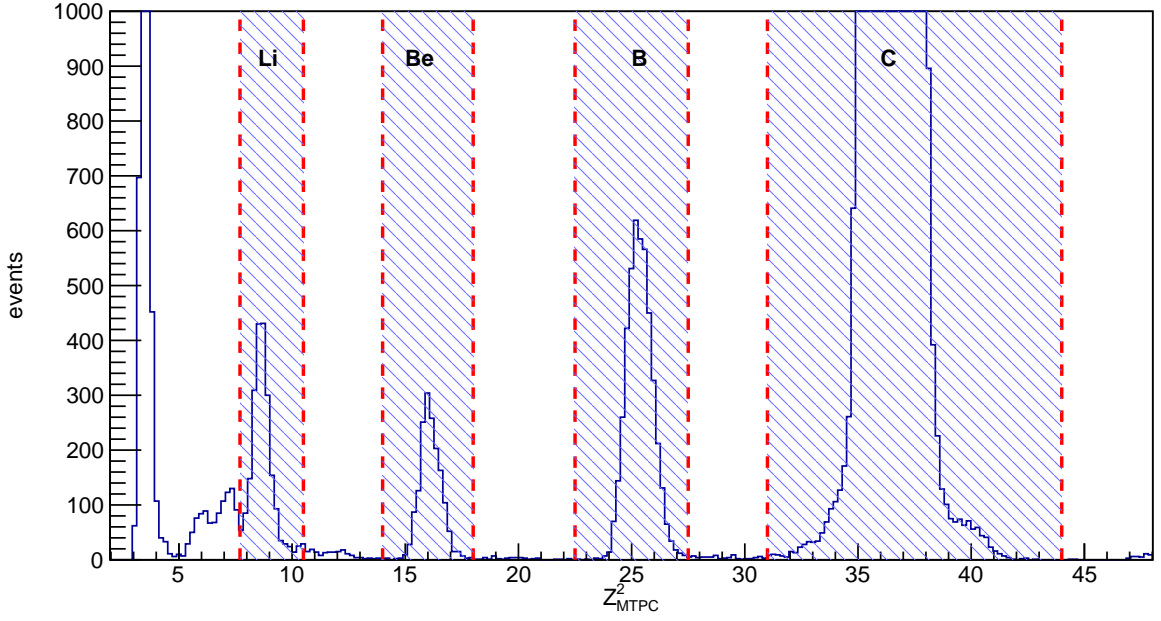Figure 5.7.: Same as Fig. 5.5 for lithium events in the MTPC-L.

Figure 5.8.: Squared charged distribution of fragments in the MTPC-L. The blue shaded regions correspond to the cut used to select carbon, boron, beryllium and lithium fragments in the MTPC (see text for details).

Let us consider two isotope nuclei, where one is the beam and the other is the fragment nucleus produced from the beam-target interaction. They consist of A_{beam} and $A_{\text{frag.}}$ number of nucleons with charge Z. Let x_{beam} and $x_{\text{frag.}}$ be the nominal position along the x-axis at the end of the MTPC-L, corresponding to the beam and the fragment track respectively. The process of nuclear fragmentation conserves the momentum per nucleon p_A but the rigidity of the fragment nucleus is different from that of the beam. Since charged fragments are deflected in the magnetic field depending on their rigidity, a change in rigidity deviates the fragment track from the beam track, resulting in a different x position than that of the beam. The deflection of the fragment tracks with respect to the nominal beam position at the end of MTPC-L is written as

$$\Delta x = x_{\text{frag}} - x_{\text{beam}}. \tag{5.4}$$

The final x position corresponding to a track is related to the rigidity as $x \propto 1/R$. Hence fragments with higher rigidity bend less compared to low rigidity fragments. Therefore, final x-positions of different fragments at the end of the MTPC can be determined as

$$\Delta x = x_{\text{frag}} - x_{\text{beam}} \propto \left(\frac{1}{R_{\text{frag}}} - \frac{1}{R_{\text{beam}}} \right). \tag{5.5}$$
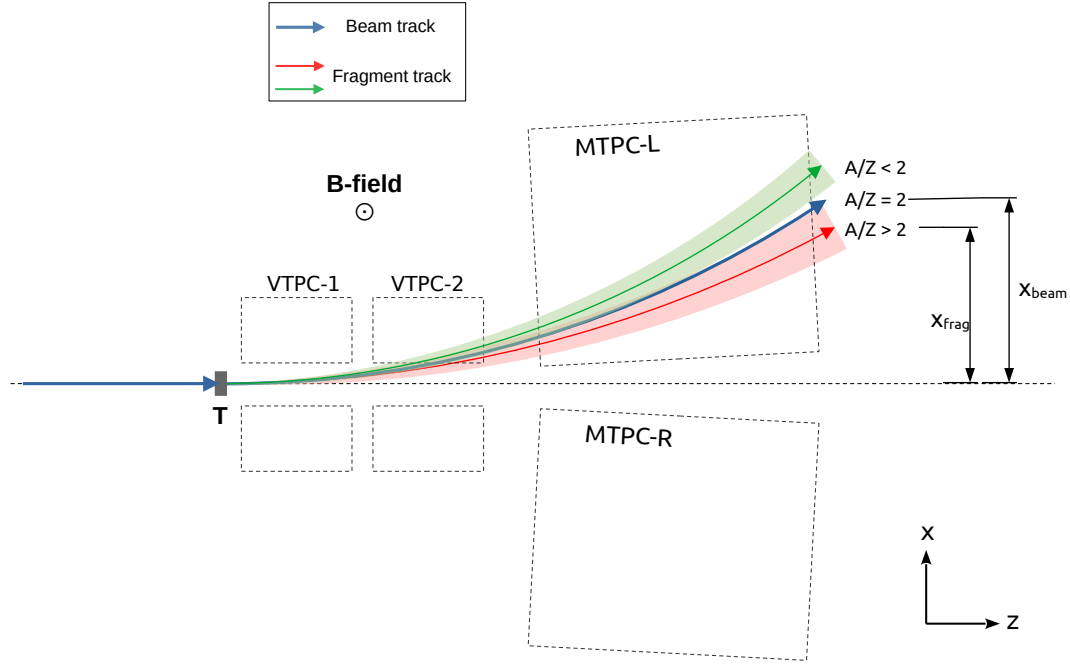
Figure 5.9.: Schematic diagram depicting the deflection of the tracks in the magnetic field of the VTPCs. These tracks correspond to the beam nucleus (blue) and the secondary fragments (red & green) produced at the target (T). The direction of the magnetic field is as shown. The red and green bands correspond to the width of the fragment peaks, σ_F, due to the Fermi momentum, p_F, imparted during the fragmentation process.

Furthermore, the rigidity R for a nucleus can be expressed in terms of its mass number, and charge as, $R = p_\mathrm{A}(A/Z)$. Therefore, (5.5) can be re-written as,

$$\Delta x = \Theta \frac{Z}{p_\mathrm{A}} \left(\frac{1}{A_\mathrm{frag}} - \frac{1}{A_\mathrm{beam}} \right). \tag{5.6}$$

A proportionality constant Θ is introduced here. It quantifies the bending power of the magnetic field with unit equivalent to rigidity/cm and is written as GVcm/c. Since p_A is conserved, all nuclei with the same rigidity, that is to say, all nuclei possessing the same A/Z ratio are deflected equally, to the same final x position as measured in the MTPC-L. Consider ^{12}C as the beam particle with $A/Z = 2$. Therefore, these beam particles as well as the secondary fragments produced due to the beam-target interaction with $A/Z = 2$ (like ^{10}B, ^{6}Li) have the same x-position. Other nuclear fragments, with $A/Z < 2$ and $A/Z > 2$,
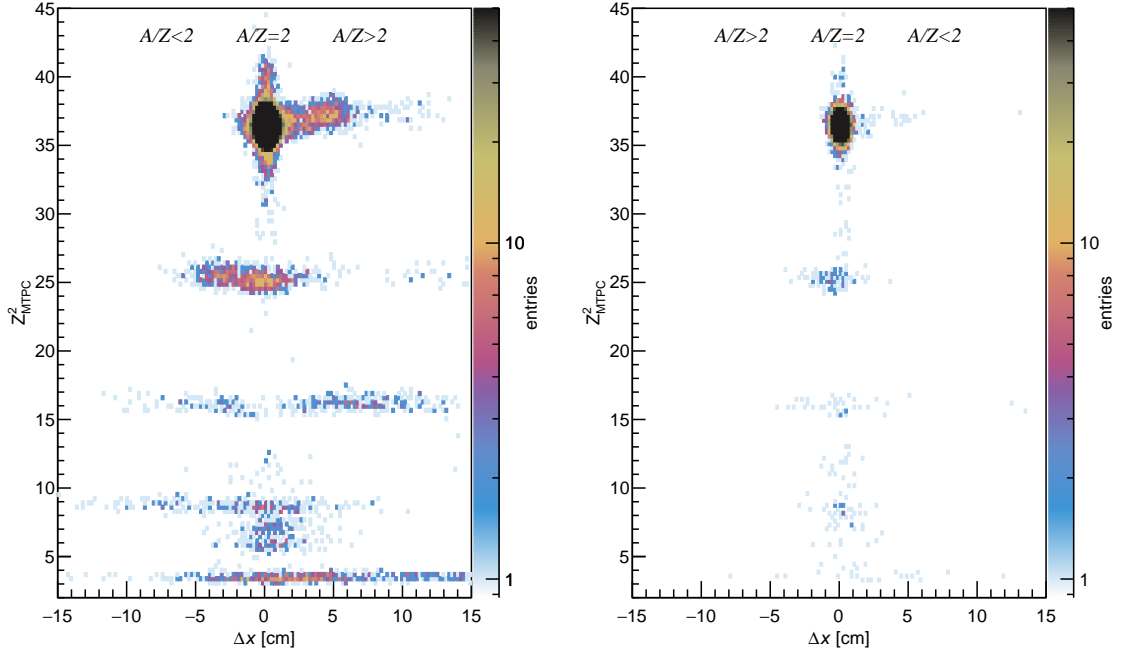
Figure 5.10.: Nuclear fragments produced by the interaction of the ^{12}C beam with the target shown relative to the nominal beam position in the MTPC at $\Delta x_{\text{beam}} = 0.0\,\text{cm}$. The non-interacting beam is seen as the dark blob at this position. The squared charge measured in the MTPC is shown on the y-axis, with target inserted as shown on the left, and target removed on the right)

are positioned subject to their rigidity, either at larger or smaller values of Δx compared to the nominal beam position. This can be seen in Fig. 5.9, where the fragments detected in the MTPC-L are shown for the IN and OUT cases, in the left and right panels respectively.

Additionally, the fragmentation process imparts a non-zero momentum of the order of Fermi momentum ($p_{\text{F}} \approx 250\,\text{MeV}/c$), in the rest frame of the fragment. This induces a spread $\sigma(p_{\text{z}})$ in the longitudinal component of the momentum of the fragment p_{z}, equivalently altering the rigidity of the fragment nucleus. This influences the placement of the fragment track by spreading its final x position as well. The x distribution of the fragment tracks have a width σ_{F}, hereafter called as the Fermi width. The value of σ_{F} depends on two factors: first, the mass number of the fragment A_{iso}, and second, the distance from the end of the MTPC, to where it is produced. For instance, a ^{11}C fragment produced by the beam-target interaction at target z position is different from a ^{11}C fragment produced at VTPC-2, downstream of the target, inside the magnetic field.

Therefore $\sigma_F(z{=}target) > \sigma_F(z{=}VTPC{-}2)$. This knowledge helps in distinguishing true signal from the target from the tracks originating out of the target. The Fermi width of tracks originating from the target is shown as green and red bands for fragments with different mass numbers in Fig. 5.9. The Z^2 v/s. Δx distribution of such fragments is shown in Fig. 5.10 for the IN and OUT cases.

5.4. Fitting the Distribution of Fragments

In order to determine the isotopic yields of the various fragments produced in the beam-target interactions, the Δx distribution of the fragments in the MTPC needs to be fit with an appropriate model describing the detector response, combined with the width due to the Fermi motion of the fragments. A flat-top Gaussian function with symmetric exponential tails is used as the detector model to describe the MTPC Δx response (Eq. (5.7)). The physical basis to use this function is that it appropriately combines the momentum acceptance of the beam-line convolved with the track resolution of the MTPC (denoted by $D(x, \Delta x, \sigma)$). The flat-top Gaussian function is a convolution of a rectangular function corresponding to the momentum acceptance slit in the mass spectrometers on the H2 beamline, and a Gaussian function associated with resolution to determine the x-position of the track at the exit of the MTPC. All the beam nuclei (called the primary particles) constituting the composite beam are fit with this model. It is mathematically expressed as follows:

$$D(\Delta x, \delta x, \sigma_{\text{det}}, \lambda) = \kappa \left(\frac{1}{2\delta x} \left(\text{erf}\left(\frac{\Delta x + \frac{\delta x}{2}}{\sigma_{\text{det}}\sqrt{2}} \right) + \text{erf}\left(\frac{\Delta x - \frac{\delta x}{2}}{\sigma_{\text{det}}\sqrt{2}} \right) \right) \right) + (1 - \kappa) \left(\frac{1}{2\lambda} \exp\left(-\frac{|\Delta x|}{\lambda} \right) \right)$$

(5.7)

The first term is the flat-top Gaussian function whereas the second term denotes the symmetrical exponential tails characterized by the parameter, λ, and are attributed to multiple scattering in the target and the detector material. The width of the flat top Gaussian is denoted by δx. Here κ denotes the relative fraction of the two functions in the model. Details of all the parameters are described in Sec. 5.5.

The fragments produced in the beam-target interaction (secondary particles) are fit with an additional Gaussian ($G(x, \sigma_F)$) convolved with the detector function ($D(\Delta x, \delta x, \sigma_{\text{det}}, \lambda)$) to model the spread in the momentum due to their Fermi motion Sec. 2.5. It is denoted as σ_F and is called the Fermi width (see Sec. 5.5.3 for further details). The complete model

used for the fit is written as the convolution of the two functions as,

$$D(\Delta x, \delta x, \sigma_{\text{det}}, \lambda) \otimes G(\Delta x, \sigma_{\text{F}}) = D(\Delta x, \delta x, \sigma_{\text{det}}, \lambda) \otimes \frac{1}{\sigma_{\text{F}}\sqrt{2\pi}} \exp\left(-\frac{\Delta x^2}{2\sigma_{\text{F}}^2}\right). \qquad (5.8)$$

The convolution is computed over the entire fitting range, $-22.0 < \Delta x /\text{cm} < 22.0$. A combined Poisson binned log-likelihood fit of the three datasets namely PE, C, and OUT is performed on the Δx-distribution using the MINUIT minimization program [78]. For the case of Poisson-distributed histogram, the corresponding likelihood chi-square function, χ_{p}^2, that was minimized in the fit is taken from Ref. [79], and is written as,

$$\chi^2 = 2 \sum_i D_i - n_i + n_i \ln\left(\frac{n_i}{D_i}\right), \qquad (5.9)$$

The summation is over all the bins, indexed as i. For each bin, the number of events predicted by the fit model described in Eq. (5.8), is written as D_i, and the number of events in the bin from the data as n_i. The model input parameters retrieved from the fit are discussed in the next section.

5.5. Fit Parameters

The model parameters of the fit essentially aid in quantifying the measurement and also to understand the systematic uncertainties related to the experiment. These parameters retrieved from the fit to the fragment distributions as discussed in the previous sub-section are discussed here in further details.

5.5.1. Normalization

The aim of fitting the Δx-distribution of the fragments is to determine the yield of a particular isotope. In principle, it is given by the number of tracks as measured in the MTPC-L corresponding to different isotopes, which inturn is determined from the normalization of each of the peaks, retrieved from the fit. For a target setting T, we denote the number of beam tracks as $N_{\text{beam}}^{\text{T}}$, and the number of fragment tracks as $N_{\text{iso}}^{\text{T}}$. These values for the three target settings are given in Tab. 5.5

Table 5.3.: The fit parameters for the carbon and boron fragments Δx-distribution in the MTPC. The superscript 'p' stands for primary and corresponds to the nucleus present in the beam composition, whereas the superscript 'dn' corresponds to fragments produced inside the magnetic field, downstream of the target. Quantities in square brackets are fixed during the fit.

Element	Isotope	Experimental parameters					Fragment parameter	
		δx (cm)	σ_{det} (cm)	Θ (GVcm/c)	λ (cm)	κ	α	σ_{F} (cm)
Carbon -	12^{p}	0.416 ± 0.006	0.252 ± 0.005	1244 ± 22	0.42 ± 0.02	0.83 ± 0.02	-	[0.0]
	11						1.00	1.17 ± 0.05
	10						1.52	1.77 ± 0.08
	11^{dn}						0.69	0.80 ± 0.03
Boron -	10^{p}	[0.416]	[0.252]	[1244]	[0.42]	[0.83]	-	[0.0]
	11						1.00	1.10 ± 0.04
	10						1.52	1.67 ± 0.06
	11^{dn}						0.69	0.80 ± 0.03
	10^{dn}						0.67	0.78 ± 0.03
Beryllium -	7	[0.416]	[0.252]	[1244]	[0.42]	[0.83]	1.00	3.65 ± 0.07
	9						0.65	2.37 ± 0.05
	10						0.49	1.78 ± 0.03
Lithium -	6	[0.416]	[0.252]	[1244]	[0.42]	[0.83]	-	2.28 ± 0.17
	7						-	3.31 ± 0.27

The probability of producing the fragments downstream of the target, inside the magnetic field (denoted with a subscript 'dn' in Figs. 5.11 and 5.12), is independent of the target setting. These fragments are supposed to be the result of the beam interacting with the detector support structures. Therefore, the normalisations of these peaks is shared among the data-sets in the combined fit.

5.5.2. Experimental Parameters

The experimental parameters are used in understanding and quantifying the measurement setup. Hence they are shared amongst all the three data sets in the combined fit. Owing to large dataset size, these parameters are best estimated from the carbon fragment fit. For the boron, beryllium and lithium fragment fits, these values are fixed to the values retrieved from the carbon fits.

The first parameter given in Tab. 5.3 is δx, which quantifies the slit width corresponding to the momentum acceptance of the beam-line. It can be calculated from the best-fit value as $\delta x / x_{\text{beam}}$, where x_{beam} is the final x position of the beam particles at the end of the MTPC after deflecting through the magnetic field. For ^{12}C beam, $x_{\text{beam}} = 46.98$ cm and from the fit we have $\delta x \approx 0.42$ cm. Therefore, the beam-line acceptance is calculated as

$\delta x / x_{\text{beam}} = 0.42/46.98 \approx 0.09\%$. This value is consistent with experimentally set value $\Delta p/p \approx 1\%$ of the H2 beamline.

Furthermore, the energy loss of the beam inside the target reduces its total momentum and induces an additional constant shift in x_{beam}. This is calculated based on the change in the total momentum of the beam as, $\Delta p_{\text{beam}} = (p_A A_{\text{beam}} - p_{\text{dEdx}})$, where p_{dEdx} quantifies the energy loss. Therefore, the beam rigidity can be written as, $R_{\text{beam}} = \Delta p_{\text{beam}}/Z$, to further calculate the relative positions of the isotopes as discussed earlier. For empty target holder (OUT), we set $p_{\text{dEdx}} = 0.0 \, \text{GeV}/c$, while the same for targets retrieved from the fit is $p_{\text{dEdx}} = 0.12 \, \text{GeV}/c$ for PE, and $p_{\text{dEdx}} \approx 0.14 \, \text{GeV}/c$. These values are within 10% of energy loss calculated from the Bethe equation Eq. (3.5) for a minimum ionizing particle.

The detector response of the MTPC is given by the parameter σ_{det}. It quantifies the track resolving power of the TPC along the x-direction. While the parameter λ depicts the symmetric tails attributed to multiple scattering of the particle passing through the various materials following its curved trajectory in the TPCs.

5.5.3. Fragment Parameters

As mentioned earlier, the Fermi width σ_F is a distinguishing factor to identify the various isotope fragments. It depends on the mass number of the fragment and its point of origin. The procedure adopted in the fit is as follows: for a fit corresponding to the isotope distribution of one element, the expected σ_F for all the isotopes is determined using a Monte Carlo code, then we take the ratio of the Fermi widths of all the isotopes present in the data to the width of one of the isotope as the reference. This ratio is written as $\alpha = \sigma_F(\text{iso})/\sigma_F(\text{ref.})$. This ratio is used for fitting fragment distribution. The isotope with the highest statistics is chosen as the reference. For instance, for the carbon fit, ^{11}C has the highest yield compared to any other isotopes. Hence its Fermi width, $\sigma_F(^{11}\text{C})$ is used as an internal reference value in the carbon and the boron fits as well. The Fermi width $\sigma_F(\text{iso}) = \alpha\sigma_F(^{11}C)$.

The Fermi widths are determined from a Monte Carlo method by simulating the transport of the fragment nucleus to the MTPC through the $\vec{B}$-field in the VTPCs. In principle, it randomizes the momentum 3-vector, $\vec{p} \equiv (p_x, p_y, p_z)$ for each nucleon of the fragment nucleus in its rest frame, to simulate the Fermi motion. Next, the fragment system is Lorentz-boosted to the laboratory frame to get the final values of the three components of $\vec{p}$ at the z-position corresponding to the end of the MTPC ($z = 730 \, \text{cm}$). The distribution

of the lateral component of the momentum p_x along with the longitudinal component p_z determines the corresponding Fermi width, σ_F. Since σ_F is a function of the mass number of the fragment, therefore $\sigma_F(^{11}C) = \sigma_F(^{11}B)$ and similarly, $\sigma_F(^{10}C) = \sigma_F(^{10}B)$. The scaling factor α for each of the isotopes used during the fit is given in Tab. 5.3.

Similarly, in the beryllium fit, the reference σ_F is the Fermi width of the ^7Be isotope. The scaling factor α for other isotopes is calculated in the similar way as described for carbon isotopes. While for the lithium fit, the Fermi widths for the two peaks were set independently not constrained to any refernce Fermi width. The values of σ_F for ^7Li and ^7Be are comparable at 1σ deviation.

5.6. Fit results

The results from the combined fit to the distribution of carbon fragments for the three data sets is shown in Fig. 5.11. The ^{12}C beam that passes without undergoing an interaction is shown as the orange peak at $\Delta x = 0\,\text{cm}$. The symmetric exponential tails attributed to multiple scattering are clearly seen for the ^{12}C peak. Carbon isotopes ^{11}C and ^{10}C produced from fragmentation of ^{12}C are shown in pink and teal respectively. In addition to this, the ^{11}C fragments produced further downstream of the target, inside the magnetic field, is shown as the blue peak. Since these fragments do not traverse the magnetic field completely, they are deflected to a lesser extent than the fragments originating from the target. Hence it is appropriately placed in the valley between ^{12}C and ^{11}C, assuming it originates from the z position corresponding end flange of He beam pipe or the VTPC-2 support structure. It is denoted with the subscript 'dn' on the plot, and is further explained in Sec. 6.1. Including this peak in the fit is needed to describe the overall distribution.

Fit results for the boron fragments are shown in Fig. 5.12. Each of the data sets is fit with five peaks corresponding to boron isotopes originating at various locations in the experiment. Similar to the carbon isotopes discussed previously, the true signal of the boron isotopes ^{11}B and ^{10}B produced at the target is shown as pink and teal peaks respectively. The fragments produced downstream in the magnetic field are shown as blue and green peaks for ^{11}B and ^{10}B respectively. Finally, the narrow orange peak corresponds to the primary ^{10}B impurity nucleus present in the beam composition. It is interesting to note that, the three ^{10}B peaks posses the same rigidity and hence coincide exactly at
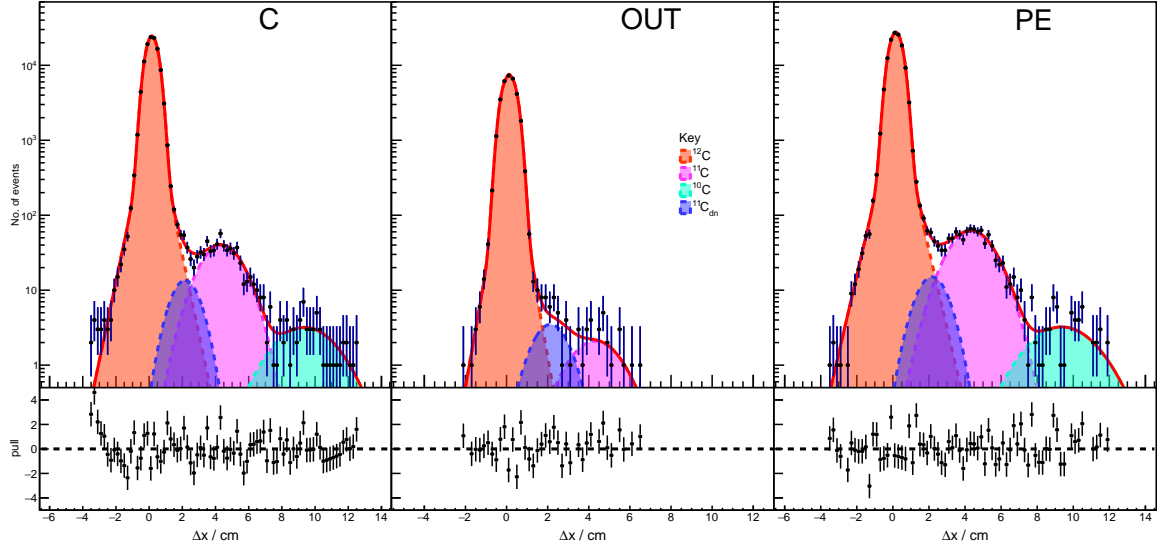
Figure 5.11.: Results from the combined fit to the Δx-distribution of the carbon fragments as measured in the MTPC-L for the three data sets, C, OUT and PE. Further information on the various peaks is discussed in the text.

the same value, $\Delta x = 0$ cm. They are distinguished from each other only based on their different widths.

Similarly, the fit results of the beryllium and lithium fragments are shown in Fig. 5.13 and Fig. 5.14 respectively. In the case of beryllium, three peaks corresponding to ^{7}Be (orange), ^{9}Be (pink) and ^{10}Be (teal) are used to describe the fragment distribution. Identification of the isotope peaks is severly hindered by poor statistics in the OUT case as seen in the middle panel of Fig. 5.13. Nevertheless, the combined fit across the three data set bypasses this issue of describing the distribution well such that the integral of the fit function is in good agreement with the number of events in the in the OUT data set. The ^{8}Be isotope is an extremely short-lived radionuclide, which α decays to ^{4}He with half-life $\tau \approx 82$ atto-seconds. Therefore, it decays before it can reach the MTPC-L, and is absent in our data, as seen in Fig. 5.13. For the lithium fit, two isotope peaks ^{6}Li (orange) and ^{7}Li (pink) are fit.

The fragments contributing to the total boron production are the radionuclides ^{11}C, ^{10}C, the boron isotopes ^{11}B, and ^{10}B, and the ^{10}Be. Fragmentation of ^{12}C to ^{10}C is not measured in this analysis, due to low statistics, and absence of primary ^{10}C in the beam composition which is essential for the measurement, as will be discussed later in Secs. 6.3.2 and 6.4. The combined statistics of the ^{11}C, ^{11}B and ^{10}B is much larger than that of the individual Be and Li isotopes. Moreover, the overlap of the Be and Li peaks due to smearing
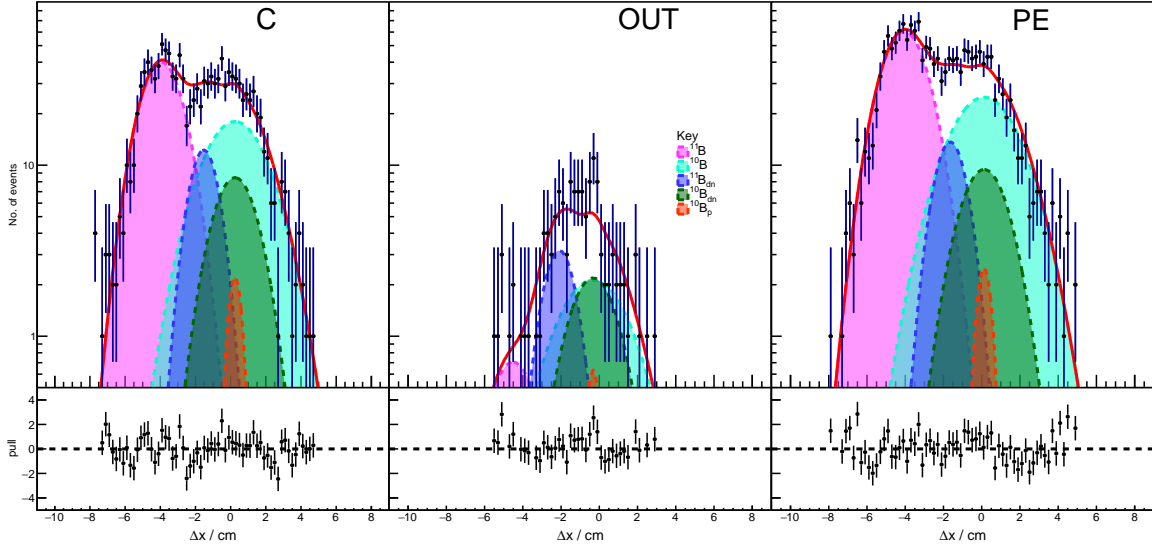
Figure 5.12.: Same as Fig. 5.11 for the distribution of boron fragments in the MTPC-L.

of their Fermi widths is more compared to that of the C and B fragments. This leads to inefficient identification of the isotopes in the fit, but these light fragments can still be measured by the MTPCs. Systematic study related to adjusting the magnetic field strength is required to determine the optimal separation of low-mass isotopes, without increasing contributions from secondary downstream interactions. Additionally, the Z^2_{MTPC} based selection of the Li and Be fragment tracks needs further investigation, particulary for Li, where the selection efficiency is potentially hampered on the rising edge of Z^2_{MTPC}, as seen in Fig. 5.8. Therefore, the focus of the analysis framework developed in the next chapter is limited to the production of ^{11}C, ^{11}B, and ^{10}B. Nevertheless, it will be shown that the same framework is applicable to measure production of lighter fragments as well, thereby generalizing the analysis.

The measured number of ^{12}C $N_{12\text{C}}$ and total number of carbon fragments N_{C} in the MTPC are tabulated in Tab. 5.4. The probabilities therein correspond to the total measured mass-, and charge changing reactions, calculated as,

$$P^{\text{int.}} = 1 - P^{\text{surv.}}, \tag{5.10}$$

where $P^{\text{surv.}} = \frac{N_{\text{C}}}{N_{\text{beam}}}$, is the survival probability of the carbon nucleus, and will be explained in details in Sec. 6.1. Number of ^{11}C, ^{11}B, and ^{10}B MTPC fragments and the respective total production probabilities are given in Tab. 5.5. The production probabilities are simply
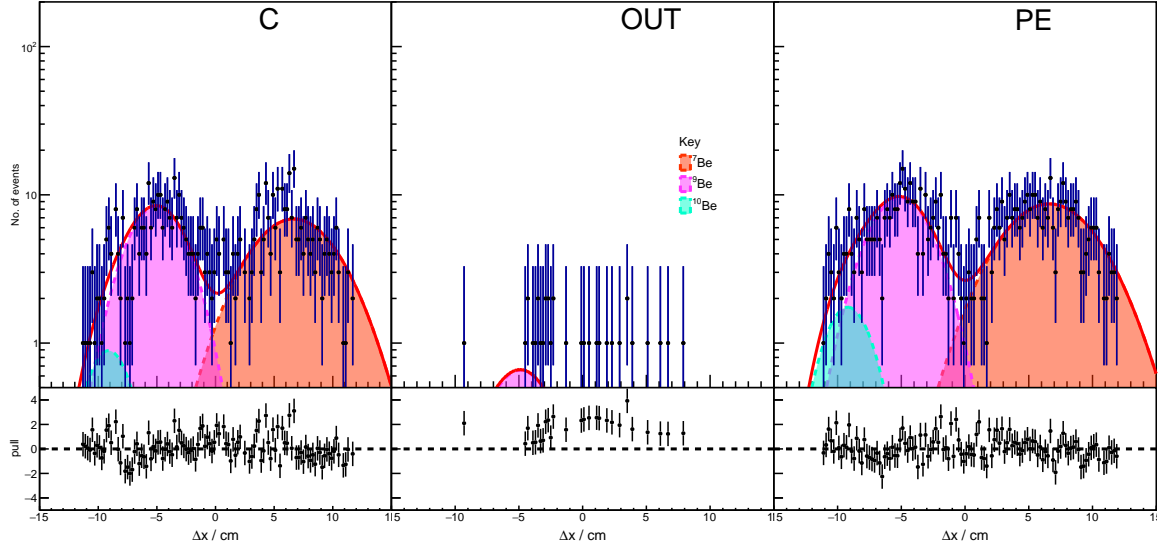
Figure 5.13.: Same as Fig. 5.12 for the distribution of beryllium fragments in the MTPC-L
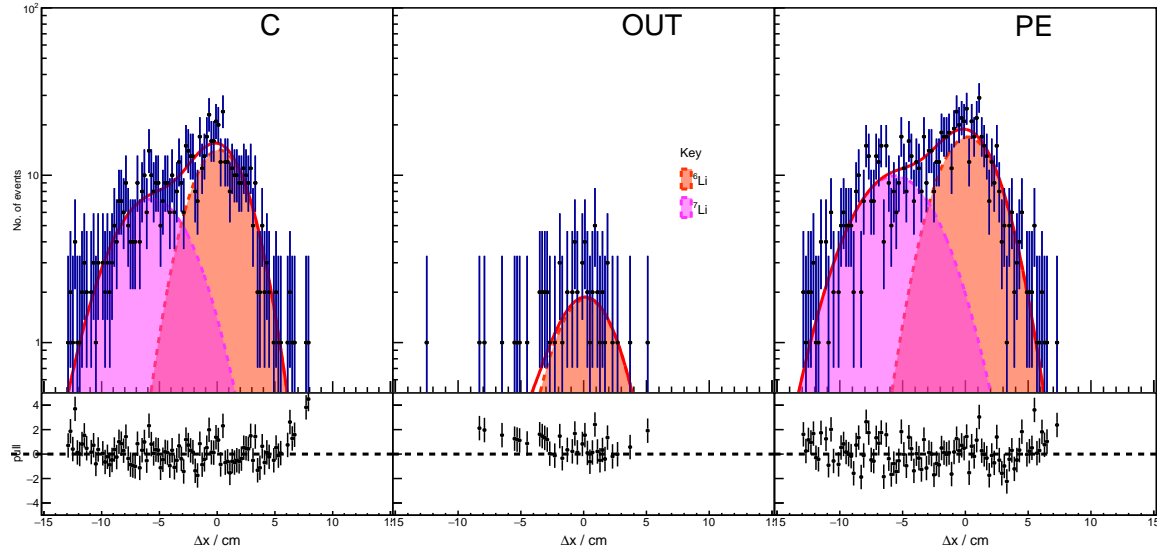

Figure 5.14.: Same as Figs. 5.12 and 5.13 but for lithium fragments.

given by the ratio,

$$P_{12C \to f} = \frac{N_{12C \to f}}{N_{beam}}. \tag{5.11}$$

where f = {^{11}C, ^{11}B, ^{10}B}. These are the main quantities that will be used in the derivation of cross section, detailed in the next chapter.

Table 5.4.: The total number of ^{12}C beam particles and that as measured in MTPC-L, for the three target settings, namely PE, C and OUT. N_{beam} is the number of beam particles. $P^{int.}$ to total measured interaction probability calculated as Eq. (5.10)

Target	N_{beam}	Mass-changing		Charge-changing	
		N_{12C}	$P^{\text{int.}}$	N_C	$P^{\text{int.}}$
PE	150883	125902 ± 520	0.166 ± 0.001	126900 ± 527	0.159 ± 0.001
C	135284	113388 ± 485	0.162 ± 0.001	114062 ± 490	0.157 ± 0.001
OUT	34990	31419 ± 255	0.102 ± 0.002	31453 ± 257	0.101 ± 0.002

Table 5.5.: The number of recorded beam particles N_{beam} and fragments, with the corresponding total production probability calculated using Eq. (5.11) to the three datasets, PE, C, and OUT, determined from the fit to the fragment distribution in the MTPC-L.

Dataset	N_{beam}	N_{11C}	$P_{12C \rightarrow 11C}$	N_{11B}	$P_{12C \rightarrow 11B}$	N_{10B}	$P_{12C \rightarrow 10B}$
PE	150883	905 ± 55	0.0060 ± 0.0002	881 ± 45	0.0058 ± 0.0002	553 ± 41	0.0036 ± 0.0002
C	135284	587 ± 46	0.0043 ± 0.0002	578 ± 35	0.0043 ± 0.0002	400 ± 31	0.0029 ± 0.0002
OUT	34990	31 ± 7	0.0009 ± 0.0002	20 ± 6	0.0005 ± 0.0001	48 ± 12	0.0014 ± 0.0002

6. Measurement of the Cross Sections

The fit-based procedure to determine the number of nuclear fragments produced in ^{12}C interactions was described in the previous chapter. However, the results from fits to the fragment distribution in MTPC-L measure the total interaction of the beam particles along its trajectory, including the interactions occuring inside, as well as outside the target. Therefore, to compute the true, in-target total inelastic cross section and the partial cross section for isotope production, various contributing factors need to be taken into consideration. In this chapter, the framework of the analysis adopted for measuring the relevant cross-sections is discussed in details.

A formalism based on measurable probabilities is developed to derive analytical expression for calculating in-target interaction of the beam, consequently leading to cross sections. Along the same lines, various correction factors applied to the measurements and the corresponding systematic uncertainty are also computed. In this analysis, we will study three different types of reactions of interest: "mass-changing reactions", where the projectile nucleus loses at least one nucleon, "charge-changing" reactions, where the projectile loses at least one proton, and the reactions in which the projectile nucleus fragments to a particular isotope.

6.1. Interaction Regions of the Beam

In order to determine the in-target interaction probability of the ^{12}C beam, it is helpful to classify the locations along the trajectory followed by the beam particles, where its probability to undergo an inelastic interaction is non-zero. Let us denote this probability as $P_{C \to X} \neq 0$.

Following this, the experimental area is conveniently zoned into four regions of interest, where the beam nucleus can fragment by undergoing an inelastic interaction leading to a charge-changing, mass-changing, or isotope production reaction (see Fig. 6.1). The first

region is the area upstream of the target denoted by the superscript 'up'. This region extends from the S1 detector ($\approx 31\,\text{m}$ from the target) up to BPD3 ($z = 6.70\,\text{m}$), where the beam line detectors are inter-spaced with air. Among the beam line detectors consisting of S1 followed by the three Beam Position Detectors, the highest material budget corresponds to the S1 detector. It is a $6 \times 6\,\text{cm}^2$ square plastic scintillator of thickness $d_{\text{S1}} = 0.5\,\text{cm}$, made up of a polymer called vinyl toluene. The material density is $\rho_{\text{S1}} = 1.03\,\text{g/cm}^3$ and the carbon-to-hydrogen ratio in each polymer cell is $\text{C} : \text{H} = 1 : 1.1$. These physical properties make it remarkably similar to the polyethylene target (PE) and render it an appropriate site for the interaction of the beam nuclei. The BPDs are gas-filled multiwire proportional chambers, and the nuclear interaction length of a single BPD is approximately 4% of that of S1 (see Tab.1 in [66]). Therefore the interaction probability is comparitively smaller than at S1.

The second region is associated with the target itself and the beam interactions inside the target material. The corresponding probability is called the in-target interaction probability and is the primary quantity of interest in this measurement. It is denoted by the superscript 'T' throughout the analysis. The third region of interaction is close to, but downstream of the target. The target is placed inside the a Helium gas-filled box comprising of the Vertex Detector (VD). Due to its proximity to the target, beam nuclei interacting inside the VD volume will resemble the beam fragmentation at the target itself. These pseudo interactions also need to be accounted for, to avoid miscalculation. This region is denoted by the superscript, 'VD'.

Finally, the fourth region is the downstream region comprising the time projection chambers, namely the two sets of Vertex-TPCs placed inside the superconducting magnets, the Gap-TPC, and the Main-TPC. The charged nuclei follow a curved trajectory traversing the vertex magnets and can interact with the support structures of the TPCs, leading to fragmentation. Moreover, a pipe filled with helium gas is installed on the beam line, between the two chambers of VTPCs. Its purpose it to suppress the number of δ-electrons, and decrease event-level fluctuations of the track densities in the TPCs. The outer rim of the pipe is made from composite carbon fiber. Therefore, given the magnetic field setting for the pilot run, there is a finite probability for the beam to interact in this region, leading to production of fragments. Since the VTPC support structures and the He beam pipe are within $1\,\text{m}$, these two interaction locations are lumped into one single downstream region. These four interaction regions are schematically illustrated in Fig. 6.1. The curved
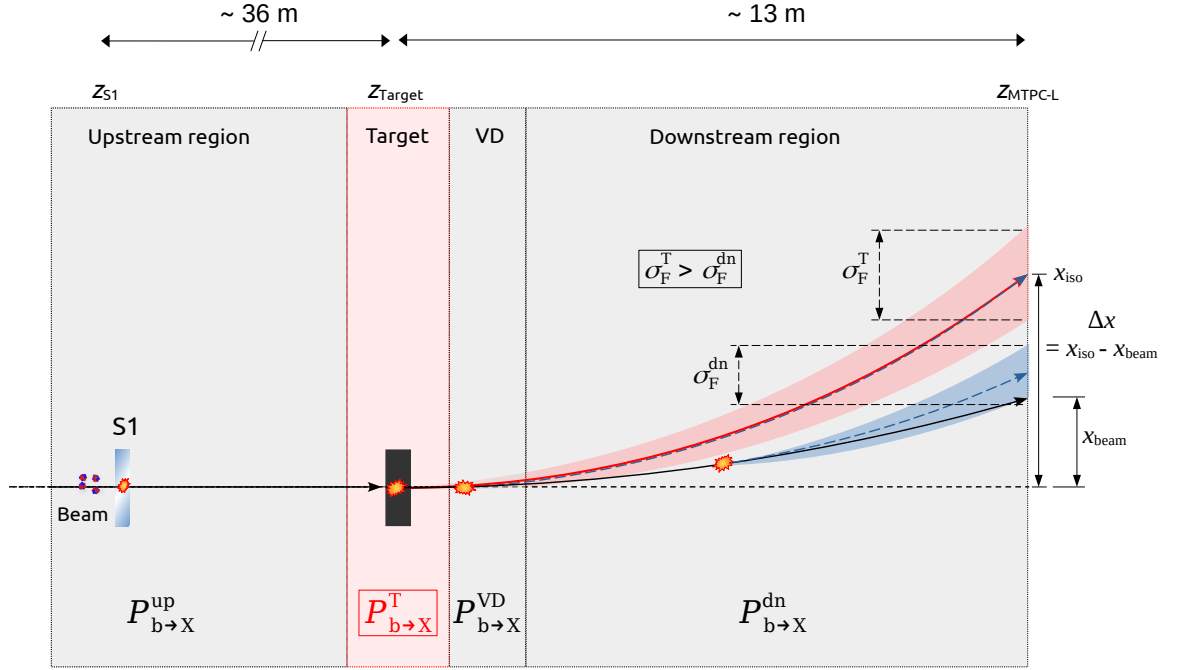
Figure 6.1.: An illustration of the four interaction regions of the experiment contributing to the total measured interaction probability as seen in the $x - z$ plane (see text for details of the regions and the corresponding probabilities). The explosion symbols denote interactions.

beam track is shown as the black solid line with a total deflection x_{beam}, along the x-direction. The trajectory of the fragments produced at the target location and in the VD region are shown with a red dashed line. The red band depicts the Fermi width σ_F^T of the fragments. The blue dashed line and the band (σ_F^{dn}) shows the nuclear fragments produced downstream of the target, inside the magnetic field.

In the following development of the analysis formalism, the beam particle is denoted as 'b' and let 'X' be the resulting family of fragment nuclei lighter than 'b'. Then, b→X denotes a charge-changing or mass-changing reaction. In the case of the production of a specific isotope fragment 'f', b→f denotes the isotope production reaction. To determine the true in-target interaction probability, it is convenient to work with the probability that a nucleus that traverses the beam line retains its identity, by not undergoing any interaction. It is written as $P_{b\to b}$ for the beam nucleus 'b' and $P_{f\to f}$ for the fragment nucleus 'f'. It is called the survival probability of the corresponding nucleus, and will be used extensively in the analysis to simplify the calculations [6]. Each of the following sections describes the method of determining the survival probabilities from the measured number of particle tracks, for the three types of reactions analyzed in this work. Since probability
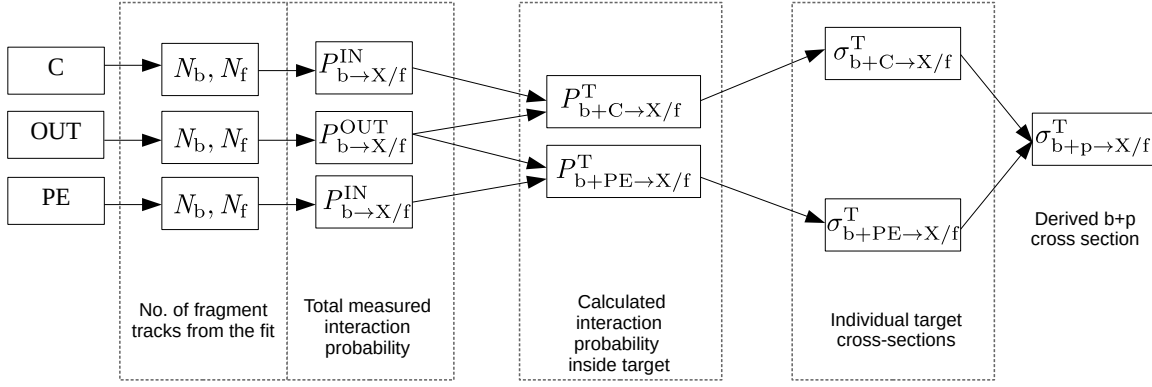
Figure 6.2.: The general flow of the analysis undertaken in this work for a ^{12}C nucleus as the fragmenting beam particle. Here 'T' denotes the target status and 'X' denotes a nuclear fragment other than ^{12}C, in general, represents as charge-, mass-changing, or a specific production reaction.

is a conserved quantity, the interaction probability, for instance, for nucleus 'b', is thus written as, $P_{b \to X} = (1 - P_{b \to b})$.

The steps in the analysis are represented in the flowchart shown in Fig. 6.2. The fit to the fragment distribution described in Ch. 5 results in the total measured number of MTPC tracks (N_f) for each target setting. Combining this with the number of beam events N_b, the total measured interaction or production probability is computed, including the one for the empty target holder case (OUT). The next step is to calculate in-target interaction or production probability for PE and C, after correcting for target out interactions. Following this, the cross sections for the two targets are determined, which is then lastly used to compute the relevant cross section with a proton target.

6.2. Mass-Changing Cross Section

It is essential to define a mass-changing reaction in the context of a nucleus-nucleus interaction. In this work, the mass-changing interaction is defined as an inelastic interaction resulting in the loss of one or more nucleons from the beam nucleus. Therefore, the emphasis is explicitly concerned with the projectile fragmentation in a fixed-target experiment.

Let the projectile beam of charge Z_b, consisting of A_b nucleons, be denoted as 'b'. A mass-changing reaction is represented as b→X, where X is any particle other than the nucleus 'b'. In the simplest case, the assumption is that X is a nucleus with A_X nucleons,

such that $\Delta A = A_{\mathrm{b}} - A_{\mathrm{X}} \geq 1$. The total number of beam particles incident on the target T is given by N_{b}. Let N be the number of particles that do not undergo an inelastic interaction and reach the MTPC. This number is determined by measuring the number of MTPC-L tracks associated with nucleus 'b'. Then the total measured survival probability of nucleus 'b' is written as,

$$P_{\mathrm{b}\to\mathrm{b}} = \frac{N}{N_{\mathrm{b}}} \tag{6.1}$$

The terms of the ratio above are known measured quantities. In the case where the target is placed in (IN), it is further expressed as a product of the individual survival probabilities of the beam nucleus in the four regions defined above, namely, upstream, the target, the region close to and downstream of the target (VD), and downstream, as,

$$P_{\mathrm{b}\to\mathrm{b}}^{\mathrm{IN}} = P_{\mathrm{b}\to\mathrm{b}}^{\mathrm{up}} P_{\mathrm{b}\to\mathrm{b}}^{\mathrm{T}} P_{\mathrm{b}\to\mathrm{b}}^{\mathrm{VD}} P_{\mathrm{b}\to\mathrm{b}}^{\mathrm{dn}}. \tag{6.2}$$

For the empty target holder (OUT), since there is no target, the corresponding survival probability $P_{\mathrm{b}\to\mathrm{b}}^{\mathrm{T}} = 1$. Therefore, the total measured survival probability in this case is written as a product of only three independent probabilities as,

$$P_{\mathrm{b}\to\mathrm{b}}^{\mathrm{OUT}} = P_{\mathrm{b}\to\mathrm{b}}^{\mathrm{up}} P_{\mathrm{b}\to\mathrm{b}}^{\mathrm{VD}} P_{\mathrm{b}\to\mathrm{b}}^{\mathrm{dn}}. \tag{6.3}$$

The upstream and downstream survival probabilities are independent of the target setting. Therefore these quantities remain unchanged for the IN and OUT cases. The probability that the nucleus 'b' survives the passage through the target medium is determined on dividing equation Eq. (6.2) by Eq. (6.3), to obtain the final expression as,

$$P_{\mathrm{b}\to\mathrm{b}}^{\mathrm{T}} = \left(\frac{P_{\mathrm{b}\to\mathrm{b}}^{\mathrm{IN}}}{P_{\mathrm{b}\to\mathrm{b}}^{\mathrm{OUT}}} \right). \tag{6.4}$$

Therefore the in-target inelastic interaction (b→X) probability is simply written as,

$$P_{\mathrm{b}\to\mathrm{X}}^{\mathrm{T}} = \left(1 - P_{\mathrm{b}\to\mathrm{b}}^{\mathrm{T}} \right) = 1 - \left(\frac{P_{\mathrm{b}\to\mathrm{b}}^{\mathrm{IN}}}{P_{\mathrm{b}\to\mathrm{b}}^{\mathrm{OUT}}} \right). \tag{6.5}$$

The final expression above is a set of two equations for the two targets, namely PE and C. The in-target mass-changing probability for the beam nucleus 'b' can therefore be

determined from known quantities for the IN and OUT cases. Specific study for ^{12}C selected as the beam particle is discussed in Sec. 6.3.1.

6.3. Charge-Changing Cross-section

The measurement of the charge-changing reaction is analogous to the formulation of the mass-changing probability described in the previous section. To begin with, a charge-changing reaction is defined as an inelastic interaction in which a beam nucleus of charge Z_B fragments to a nucleus 'Y' of charge Z_Y after interacting with the Target (T), where $\Delta Z = Z_B - Z_Y \geq 1$. Therefore, Eq. (6.2) and Eq. (6.3) can be re-written for a charge changing reaction as well. In this case, the survival probability quantifies a charge-retaining reaction, denoted as b→b, and the numerator in Eq. (6.1) equals the measured number of MTPC events N corresponding to all the particle tracks with the charge Z_B. The final expression for the in-target interaction of nucleus 'B' leading to a charge-changing reaction (B*to*Y) has the exact same form as Eq. (6.5) and is written as,

$$P_{B \to Y}^{T} = \left(1 - P_{B \to B}^{T}\right) = 1 - \left(\frac{P_{B \to B}^{IN}}{P_{B \to B}^{OUT}}\right). \tag{6.6}$$

The beam nucleus 'B' can inelastically interact with the target to produce an isotope nucleus 'K', where $\Delta Z = 0$ but $\Delta A \geq 1$. Nucleus 'K' acts as an intermediate particle and possesses a finite probability to interact with a target nucleus, undergoing a charge-changing reaction, fragmenting to nucleus 'Y', such that $Z_Y < Z_K$. In such a case where a mass-changing interaction is followed by a charge-changing reaction, the process B→K→Y will resemble a charge-changing reaction of nucleus 'B'. An additional term is introduced to account for the two-step 'pseudo charge-changing' reaction by modifying the target survival probability $P_{B \to B}^{T}$ and modifying Eq. (6.2) as follows:

$$P_{B \to B}^{IN} = P_{B \to B}^{up} P_{B \to B}^{T} P_{B \to B}^{VD} P_{B \to B}^{dn} + P_{B \to B}^{up} P_{B \to K}^{T} P_{K \to K}^{VD} P_{K \to K}^{dn}. \tag{6.7}$$

The second term contains the probability that nucleus 'B' interacts inside the target, and needs an explanation. The interaction in-target interaction probability given in the equation above are $O(10^{-3})$, as will be shown in Sec. 6.4. Hence the total contribution of consecutive interactions occuring inside the target, is $O(10^{-6})$, and is numerically small

compared to the first term in Eq. (6.7) with the survival probabilities, which is of order $\mathcal{O}(1)$. Therefore, such interactions can be ignored in this analysis, for measuring the charge-changing probability of any nucleus.

6.3.1. Carbon-12

The nucleus of primary interest in this analysis is ^{12}C. Therefore, a particular case for measuring the ^{12}C mass- and charge-changing reaction is described in this section. However, the formalism can be applied to any other nuclei under investigation, the details to which are discussed in the next section. The upstream selection follows the procedure described in Sec. 5.1.1 to select the ^{12}C isotope from the composite beam as the primary fragmenting beam particle. Thus, in this case, b=^{12}C. Hence, Eq. (6.5) for a target setting T, is written as,

$$P^{\mathrm{T}}_{12\mathrm{C}\rightarrow\mathrm{X}} = \left(1 - P^{\mathrm{T}}_{12\mathrm{C}\rightarrow 12\mathrm{C}}\right) = \left(1 - \frac{P^{\mathrm{IN}}_{12\mathrm{C}\rightarrow 12\mathrm{C}}}{P^{\mathrm{OUT}}_{12\mathrm{C}\rightarrow 12\mathrm{C}}}\right). \tag{6.8}$$

Since the probability of survival can be simply written in terms of the probability of interaction, as, $P_{\mathrm{i}\rightarrow\mathrm{i}} = 1 - P_{\mathrm{i}\rightarrow\mathrm{X}}$, all the survival probability terms in the above equation are replaced accordingly. Making this substitution and re-arranging the terms in Eq. (6.8), we get,

$$P^{\mathrm{T}}_{12\mathrm{C}\rightarrow\mathrm{X}} = \frac{P^{\mathrm{IN}}_{12\mathrm{C}\rightarrow\mathrm{X}} - P^{\mathrm{OUT}}_{12\mathrm{C}\rightarrow\mathrm{X}}}{1 - P^{\mathrm{OUT}}_{12\mathrm{C}\rightarrow\mathrm{X}}}. \tag{6.9}$$

In the equation above, the probabilities on the right are calculated from the number of ^{12}C fragment tracks $N_{12\mathrm{C}}$ measured in the MTPC and the number of incident beam particles for each target setting, as

$$P^{\mathrm{IN/OUT}}_{12\mathrm{C}\rightarrow\mathrm{X}} = 1 - \left(\frac{N^{\mathrm{IN/OUT}}_{12\mathrm{C}}}{N^{\mathrm{IN/OUT}}_{\mathrm{beam}}}\right). \tag{6.10}$$

The number of tracks $N_{12\mathrm{C}}$ is determined from the fit to the Δx-distribution of carbon fragments in the MTPC, as described in Sec. 5.3. In the case of charge-changing reaction, $N_{12\mathrm{C}}$ is simply replaced by the measured number of all carbon ($Z^2_{\mathrm{MTPC}} = 36$) tracks in the MTPC, N_{C}. These numbers along with the number of beam particles, and the total measured interaction probabilities for the three target settings, namely, PE, C, and OUT, are given in Tab. 5.4. The total measured interaction probabilities are calculated using Eq. (6.8) and the in-target interaction probabilities are calculated using Eq. (6.10).

6.3.2. Auxiliary Measurement of Other Beam Nuclei

The formalism detailed in the previous section can be applied to any nucleus present in the data for computing its mass- and charge changing cross section. The upstream cuts are modified in a way to select the desired nucleus from the beam composition, to study its fragmentation. The lower and higher thresholds of the *tof* and Z^2 are altered accordingly to make the selection.

The online T3p or carbon trigger (Z^2 =36) allows the neighboring elements and their corresponding isotopes, i.e. nuclei up to a charge difference, $\Delta Z = 1$ and mass difference $\Delta A = 2$ nuclei. This provides an excellent opportunity to make additional measurements by selecting these isotopes as the primary beam particle. These auxillary measurements are done by altering the upstream cuts on the calibrated data, such as to select a desired nucleus as the primary beam particle, for instance, the isotopes neighboring the ^{12}C. The measurements are necessary for calculating various corrections and systematic effects as described in Sec. 6.6, in order to study the feed-down reactions of the type, A+p→f, where A≠^{12}C and corresponds to a neighboring nucleus, which fragment to nucleus, 'f'. These reactions alter the true ^{12}C+T interaction probabilities and need to be corrected. Equivalently, it also introduces a systematic uncertainty on the measurement. Additionally, these auxillary measurements are also used to calculate the mass-changing cross-section of a desired nucleus, which can then be input to correct the in-target production cross section (detailed in Sec. 6.6.3).

For the measurement in the scope of this analysis, the feed-down cross-section of the following nuclei need to be measured: ^{13}C, ^{11}C, ^{15}N, ^{14}N, ^{11}B and ^{10}B. These nuclei are present in the upstream beam composition (Fig. 4.1). Each of the nuclei is selected as the primary beam particle by altering the cuts on the *tof* as measured from the A-S1 system, and the Z^2 equivalent dE/dx in the scintillator S1. Furthermore, all other upstream cuts listed in Tab. 5.2 and applied for ^{12}C selection remain unchanged. Unlike the upstream selection procedure for ^{12}C described in Sec. 5.1.1, simpler rectangular cuts are applied to select a particular nucleus. This is accomplished by placing an upper and lower limit on the measured *tof* and Z^2_{S1}. The total number of beam particles corresponding to these nuclei for the three target settings, PE, C, and OUT, the total measured and the in-target interaction probability is calculated and given in Tab. 6.1.

The table shows the total number of events for each of the isotopes present in the data, along with the corresponding charge-changing and mass-changing interaction probabilities

Table 6.1.: The statistics for each of the nuclei selected as the primary beam particle (N_b) and its number as measured in the MTPC (N_i), for the mass-changing reaction. Total measured and the target-OUT corrected probabilities are also given in the last two columns.

Nucleus (i)	Target	N_b	N_i	$P_{i\to X}^{IN/OUT} = \left(1 - \frac{N_i}{N_b}\right)$	$P^T = \left(\frac{P^{IN} - P^{OUT}}{1 - P^{OUT}}\right)$
	PE	35810	30347	0.152 ± 0.002	0.084 ± 0.003
^{13}C	C	31501	26887	0.146 ± 0.002	0.077 ± 0.004
	OUT	7953	7357	0.075 ± 0.003	-
	PE	12300	10595	0.139 ± 0.003	0.068 ± 0.006
^{11}C	C	10490	9144	0.128 ± 0.003	0.057 ± 0.006
	OUT	2669	2466	0.076 ± 0.005	-
	PE	1692	1191	0.296 ± 0.011	0.098 ± 0.030
^{15}N	C	1292	949	0.265 ± 0.012	0.059 ± 0.030
	OUT	315	246	0.219 ± 0.023	-
	PE	1607	1302	0.190 ± 0.010	0.102 ± 0.019
^{14}N	C	1383	1151	0.168 ± 0.010	0.078 ± 0.020
	OUT	349	315	0.097 ± 0.016	-
	PE	1929	1379	0.285 ± 0.010	0.061 ± 0.028
^{11}B	C	1743	1261	0.276 ± 0.011	0.049 ± 0.028
	OUT	473	360	0.239 ± 0.020	-
	PE	3561	2872	0.193 ± 0.007	0.109 ± 0.012
^{10}B	C	3100	2581	0.167 ± 0.007	0.081 ± 0.013
	OUT	785	711	0.094 ± 0.010	-

calculated as Secs. 6.2 and 6.3. These auxiliary measurements are then used in the analysis to determine the contribution of the neighboring isotopes to the cross-sections determined. The feed-down from these neighboring isotopes leads to systematic uncertainty and correction to the final result.

6.4. Isotope Production Cross-section ($\Delta A = 1$)

In this section, the derivation of the equation for the in-target production of a nucleus 'f' resulting from the fragmentation of beam nucleus 'b' is described. The reaction is denoted as b→f. The total measured probability for the production of 'f' from 'b' is the ratio of the number of tracks N_f corresponding to 'f' as measured in the MTPC, to the total number of incident beam particles N_b. For both the target settings, namely IN and OUT, it is written

as,

$$P_{b \to f}^{IN/OUT} = \frac{N_f^{IN/OUT}}{N_b^{IN/OUT}}.$$

(6.11)

The number of fragment tracks in the ratio above are derived from the fragment distribution fit results (Tab. 5.5).

The analysis proceeds in the same way as described for the mass-changing reaction. To begin with, the total measured probability from Eq. (6.11) can be expanded and expressed as a sum of three terms corresponding to the three regions of interest as described in Sec. 6.1. Then the total measured probability is written as,

$$P_{b \to f}^{IN} = P_{b \to f}^{up} P_{f \to f}^{T} P_{f \to f}^{VD} P_{f \to f}^{dn} + P_{b \to b}^{up} P_{b \to f}^{T} P_{f \to f}^{VD} P_{f \to f}^{dn} + P_{b \to b}^{up} P_{b \to b}^{T} P_{b \to f}^{VD} P_{f \to f}^{dn}.$$

(6.12)

The first term measures the number of MTPC events of the nucleus 'f' that result from the fragmentation of the beam 'b' interacting in the upstream region. These fragments reach the MTPC without interacting in any of the following downstream regions, and is written as the product of the three survival probabilities $P_{f \to f}^{T} P_{f \to f}^{VD} P_{f \to f}^{dn}$. Since the upstream region is outside the magnetic field, the fragment nuclei follow a linear trajectory along the beam line. Upon encountering the magnetic field of the vertex magnets, the fragment nuclei are deflected along the x-direction by x_f^{up} cm, subject to change in its rigidity relative to that of the beam.

The fragments produced inside the target are represented in the second term containing the probability $P_{b \to f}^{T}$. The assumption here is that the beam nucleus 'b' does not interact before the target, and the fragment produced retains its identity in the downstream region before it reaches the MTPC. The deflection of fragments produced inside the target, in the magnetic field is x_f^{T} and is equal to x_f^{up}. Since the upstream production probability $P_{b \to f}^{up}$ is independent of the target setting, the fragments produced upstream will also be present in the empty target holder case (OUT). That being the case, target out data can be used to measure the corrected number of MTPC tracks of 'f'. In this case, $P_{b \to f}^{T} = 0$. Consequently, the total measured production probability for OUT is a sum of two terms, and is written as the following:

$$P_{b \to f}^{OUT} = P_{b \to f}^{up} P_{f \to f}^{VD} P_{f \to f}^{dn} + P_{b \to b}^{up} P_{b \to f}^{VD} P_{f \to f}^{dn}.$$

(6.13)

The first term is the upstream production, whereas the second term is the production of 'f' in the VD region, just downstream of the target.

The resultant fragments produced downstream of the target, inside the magnetic field are deflected to a lesser extent relative to the beam, as opposed to the fragments produced at the target location. These nuclei traverse only partially through the magnetic field and possess a smaller spread in their longitudinal momentum resulting from the Fermi motion of the fragment. This results in a narrower Fermi width $\sigma_{\mathrm{F}}^{\mathrm{dn}}$ for such fragments as depicted by the blue band in Fig. 6.1. Thus, the downstream produced fragments can be identified and included in the fit to the Δx-distribution of the fragments (eg. blue peak in Fig. 5.11). The contribution of downstream produced fragments is made explicit at the level of the fit and hence it does not contribute to the total 'f' production probability inside the target, ($P_{\mathrm{b}\to\mathrm{f}}^{\mathrm{T}}$), evading the need to correct for this during the calculation of the cross sections. The in-target production probability is obtained by subtracting Eq. (6.13) from Eq. (6.12). The resulting expression, after minor simplification, is given below:

$$P_{\mathrm{b}\to\mathrm{f}}^{\mathrm{IN}} - P_{\mathrm{b}\to\mathrm{f}}^{\mathrm{OUT}} = P_{\mathrm{b}\to\mathrm{f}}^{\mathrm{up}} P_{\mathrm{f}\to\mathrm{f}}^{\mathrm{VD}} P_{\mathrm{f}\to\mathrm{f}}^{\mathrm{dn}} \left(P_{\mathrm{f}\to\mathrm{f}}^{\mathrm{T}} - 1\right) + P_{\mathrm{b}\to\mathrm{b}}^{\mathrm{up}} P_{\mathrm{b}\to\mathrm{f}}^{\mathrm{VD}} P_{\mathrm{f}\to\mathrm{f}}^{\mathrm{dn}} \left(P_{\mathrm{b}\to\mathrm{b}}^{\mathrm{T}} - 1\right) + P_{\mathrm{b}\to\mathrm{b}}^{\mathrm{up}} P_{\mathrm{b}\to\mathrm{f}}^{\mathrm{T}} P_{\mathrm{f}\to\mathrm{f}}^{\mathrm{VD}} P_{\mathrm{f}\to\mathrm{f}}^{\mathrm{dn}}. \tag{6.14}$$

It is non-trivial to quantify the contribution of the material of the region corresponding to VD, to the total material budget. Nevertheless, the product of the survival probabilities of 'f' just downstream of the target and in the downstream regions, $P_{\mathrm{f}\to\mathrm{f}}^{\mathrm{VD}} P_{\mathrm{f}\to\mathrm{f}}^{\mathrm{dn}}$, can be determined by the auxillary measurement of nucleus 'f'. This is accomplished by altering the upstream selection such that nucleus 'f' is selected from the beam composition as the primary fragmenting particle as shown in Sec. 6.3.2. These additional probabilities can be measured from the data, owing to the fact that the nucleus type 'f' is present in the data. Then following the same procedure as described in the Sec. 6.2, we can write Eq. (6.3) for 'f' in the OUT case. The terms are re-arranged to obtain the product of the two probabilities as,

$$P_{\mathrm{f}\to\mathrm{f}}^{\mathrm{VD}} P_{\mathrm{f}\to\mathrm{f}}^{\mathrm{dn}} = \frac{P_{\mathrm{f}\to\mathrm{f}}^{\mathrm{OUT}}}{P_{\mathrm{f}\to\mathrm{f}}^{\mathrm{up}}}. \tag{6.15}$$

Furthermore, the second term of Eq. (6.14) containing the probability $P_{\mathrm{b}\to\mathrm{f}}^{\mathrm{VD}}$ can be replaced using the expression for the total target out production probability in Eq. (6.13), as,

$$P_{\mathrm{b}\to\mathrm{b}}^{\mathrm{up}} P_{\mathrm{b}\to\mathrm{f}}^{\mathrm{VD}} P_{\mathrm{f}\to\mathrm{f}}^{\mathrm{dn}} = \left(P_{\mathrm{b}\to\mathrm{f}}^{\mathrm{OUT}} - P_{\mathrm{b}\to\mathrm{f}}^{\mathrm{up}} P_{\mathrm{f}\to\mathrm{f}}^{\mathrm{VD}} P_{\mathrm{f}\to\mathrm{f}}^{\mathrm{dn}}\right). \tag{6.16}$$

Substituting Eqs. (6.15) and (6.16) into Eq. (6.14) results in the following expression:

$$
P_{b\to f}^{IN} - P_{b\to f}^{OUT} = P_{b\to f}^{up} \frac{P_{f\to f}^{OUT}}{P_{f\to f}^{up}} \left(P_{f\to f}^{T} - 1 \right) + \left(P_{b\to f}^{OUT} - P_{b\to b}^{up} \frac{P_{f\to f}^{OUT}}{P_{f\to f}^{up}} \right) \left(P_{b\to b}^{T} - 1 \right)
$$
$$
+ P_{b\to b}^{up} P_{b\to f}^{T} P_{f\to f}^{VD} P_{f\to f}^{dn}
$$

(6.17)

Re-arranging the terms in the equation above, we get,

$$
P_{b\to f}^{IN} - P_{b\to f}^{OUT} P_{b\to b}^{T} = \frac{P_{b\to f}^{up}}{P_{f\to f}^{OUT}} P_{f\to f}^{up} \left(P_{f\to f}^{T} - P_{b\to b}^{T} \right) + \frac{P_{b\to b}^{up}}{P_{f\to f}^{up}} P_{f\to f}^{OUT} P_{b\to f}^{T}
$$

(6.18)

Finally, solving the above equation for the in-target production probability of the fragment 'f', we get the following expression:

$$
P_{b\to f}^{T} = \frac{P_{f\to f}^{up}}{P_{b\to b}^{up}} \frac{1}{P_{f\to f}^{OUT}} \left(P_{b\to f}^{IN} - P_{b\to f}^{OUT} P_{b\to b}^{T} \right) - \frac{P_{b\to f}^{up}}{P_{b\to b}^{up}} \left(P_{f\to f}^{T} - P_{b\to b}^{T} \right).
$$

(6.19)

All the probabilities on the right side of Eq. (6.19) are direct measurable quantities except for the leading ratio terms corresponding to the upstream survival probabilities of nucleus 'b' and 'f'.

The ratio in the first term on the right is the ratio of the probabilities of nuclei 'b' and 'f' such that they do not undergo an inelastic interaction in the upstream region before the target. As mentioned earlier, these probabilities can be estimated by identifying the material of the beam-line detectors. The plastic scintillator S1 is identified to be the most probable location for the beam particles to interact due to its similarity to the PE target. The upstream survival probabilities can thus be estimated with the knowledge of the carbon-to-hydrogen ratio of the polymer cell of polyvinyl toluene, and the independently calculated mass-changing probabilities of the 'b' and 'f' nuclei with the C and the proton target as described in Sec. 6.2. And since the probability P is proportional to the cross-section σ, the ratio of the probabilities can be easily determined by taking the ratio of the cross-section of the 'b' and 'f' nuclei.

In the second term, the ratio is the upstream production of 'f' to the upstream survival of nucleus 'b'. The ratio is $\sim O(10^{-3})$ and is followed by the difference of the in-target mass-changing probabilities, $P_{b\to b}^{T}$ and $P_{f\to f}^{T}$ of 'b' and 'f' respectively. These quantities are calculated as per Eq. (6.4). The survival probabilities are large and nearly of the same order. Therefore, the difference term too is $\sim O(10^{-6})$, which reduces the total contribution of

the second term in Eq. (6.19). The complete derivation and estimation of the upstream probabilites is detailed in Appendix A.1.

The final step in the analysis is computing the relevant cross sections for the different reactions described in the previous sections. The interaction probability P of a particle interacting with a target (T) is written as,

$$P^{\mathrm{T}} = 1 - \exp\left(\frac{-d_{\mathrm{T}}}{\lambda_{\mathrm{T}}}\right), \tag{6.20}$$

where $\lambda = 1/(n_{\mathrm{T}}\sigma^{\mathrm{T}})$ is the nuclear interaction length measured in cm. The number density n_{T} of the target material is expressed in terms of the molar mass M, Avogadro's constant N_{A}, and the target density ρ_{T}, as $n = N_{\mathrm{A}}\rho/M$, whereas σ^{T} is the interaction cross section measured in millibarns (mb).

Eq. (6.9) and Eq. (6.19) are sets of two equations, each corresponding to the two different targets namely, PE and C. Hence the cross-section can be determined by making these substitutions and re-arranging the terms in Eq. (6.20) to give the final expression as,

$$\sigma^{\mathrm{T}} = -\frac{M_{\mathrm{T}}}{N_{\mathrm{A}}\rho_{\mathrm{T}}d_{\mathrm{T}}}(1 - \ln P^{\mathrm{T}}). \tag{6.21}$$

Therefore, after calculating the in-target interaction probabilities for the reactions b+PE and b+C, it can be substituted in Eq. (6.21) to obtain the cross-sections with the PE and C targets, respectively. The principal quantity of interest for our study is to measure the ^{12}C+p mass-changing and isotopic production cross-sections. It can then be computed as follows:

$$\sigma^{\mathrm{p}}_{^{12}\mathrm{C}\to\mathrm{X/f}} = \frac{1}{2}\left(\sigma^{\mathrm{PE}}_{^{12}\mathrm{C}\to\mathrm{X/f}} - \sigma^{\mathrm{C}}_{^{12}\mathrm{C}\to\mathrm{X/f}}\right) \tag{6.22}$$

where X denotes the mass-changing and charge-changing reaction of ^{12}C and 'f' denotes the production of specific isotope (in our case ^{11}C, ^{11}B & ^{10}B). The factor 1/2 comes from the fact that the ratio C : H = 1 : 2 in each cell of the polyethylene molecule, and therefore has to be taken into the calculation when subtracting the ^{12}C+C contribution from the ^{12}C+PE interactions.
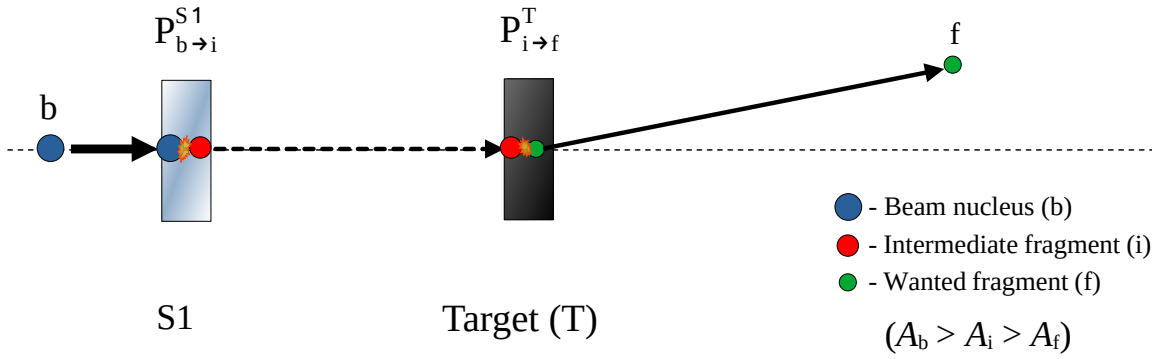
Figure 6.3.: An illustration of the two-step reaction leading to production of $\Delta A > 1$ fragments. The intermediate nucleus i shown in red is a $\Delta A = 1$ nucleus, which further fragments to the wanted fragment f inside the target.

6.5. Isotope Production Cross-section ($\Delta A > 1$)

The formulation described in the previous section is a special case for comparatively easier reaction channels. It is directly applicable to the production of nuclear fragments with A_f nucleons from the fragmentation of the beam with A_b nucleons, such that $\Delta A = A_b - A_f = 1$, e.g. the production of ^{11}C and ^{11}B from a ^{12}C beam. In the case of production of lighter fragments such that $\Delta A > 1$, e.g. the reaction $^{12}C \rightarrow ^{10}B$, additional contributions from indirect channels, more specifically, multi-step interactions, leading to fragment production, also need to be taken into account. An example of such a reaction is ^{12}C fragmenting to a $\Delta A = 1$ nucleus, like ^{11}C or ^{11}B in the upstream region, at the S1 detector, followed by its interaction with one of the targets (PE or C), resulting in $\Delta A \geqslant 2$ nuclei like ^{10}C or ^{10}B. This reaction is graphically represented in Fig. 6.3.

The thickness of the two effective targets, S1 and T itself is 0.5 cm and 1-1.5 cm respectively. In the thin target approximation, where target thickness d_T is approximately 10% of the nuclear interaction length λ associated with fragment production, the in-target probability of production is $P^T \approx O(10^{-3})$. Two-step production reactions introduce additional terms in Eq. (6.12), containing the product of the two production probabilities $P^{S1}P^T$, which is approximately $O(P^{T^2}) \sim 10^{-6}$. Therefore the additional terms are negligible, and Eq. (6.19) can be used to compute the in-target production probability for $\Delta A = 2$ fragments. The same criteria are applied in the case where the beam fragments to $\Delta A \geqslant 2$ nuclei as well, such as production of lighter nuclei like the isotopes of Be and Li. A quantitative description of both cases is discussed in detail in Appendix A.2.

6.6. Corrections to the Measured Cross Sections

The measured probabilities of the mass-changing, charge-changing and specific isotope production reactions are subject to further corrections. These corrections also introduce a systematic uncertainty in the measurement. This section describes the various corrections applied to our results.

6.6.1. Fragment Track Selection in the MTPC

The identification of the charged fragments in the MTPC is based on the energy deposit dE/dx in the detector. Consequently, the Z^2_{MTPC} is calculated from the dE/dx. Carbon tracks are selected in the range, $31.0 \leqslant Z^2_{\mathrm{MTPC}} \leqslant 44.0$. It is observed that the ^{12}C peak extends beyond this range especially beyond the lower threshold forming a rising edge. Therefore some carbon fragments below $Z^2_{\mathrm{MTPC}} < 31.0$ are lost, and must be taken into account. The number of measured ^{12}C tracks $N^{\mathrm{m}}_{12\mathrm{C}}$, and hence the mass- and charge-changing probabilities are accordingly altered due to the correction.

The number of ^{12}C required to correct $N^{\mathrm{m}}_{12\mathrm{C}}$ is determined by making a binned fit to the 1-dimensional Z^2_{MTPC} distribution in the range $31.0 \leq Z^2_{\mathrm{MTPC}} \leq 33.0$ for the three target settings PE, C, and OUT. An exponential function is used to describe the rising edge of the peak. This is shown as the green shaded region in Fig. 6.4. The fit function is extrapolated in the range $Z^2_{\mathrm{MTPC}} = 31.0$ up to $Z^2_{\mathrm{MTPC}} = 0.0$, depicted by the blue shaded region in Fig. 6.4. The integral of the blue region $\Delta N_{12\mathrm{C}}$ is used to correct for the number of ^{12}C in the cut as,

$$N^{\mathrm{true}}_{12\mathrm{C}} = \frac{N^{\mathrm{m}}_{12\mathrm{C}}}{\epsilon_{12\mathrm{C}}}. \tag{6.23}$$

Left side of Eq. (6.23) is the true number of ^{12}C after the correction. The denominator is the correction factor $\epsilon_{12\mathrm{C}}$, and is calculated using the following expression:

$$\epsilon_{12\mathrm{C}} = \frac{N^{\mathrm{m}}_{12\mathrm{C}}}{N^{\mathrm{m}}_{12\mathrm{C}} + \Delta N_{12\mathrm{C}}}. \tag{6.24}$$

The corrected number is then further used for calculating the mass-, and charge changing probabilities of ^{12}C. As can be seen from the 2-dimensional plot Fig. 5.10, ^{10}B and ^{12}C share the same x-position in the MTPC, that is, $\Delta x_{12\mathrm{C}} = \Delta x_{10\mathrm{B}} = 0.0$. Therefore, the number of ^{12}C in the tail of the carbon peak affects the number of measured ^{10}B fragments $N^{\mathrm{m}}_{10\mathrm{B}}$ as
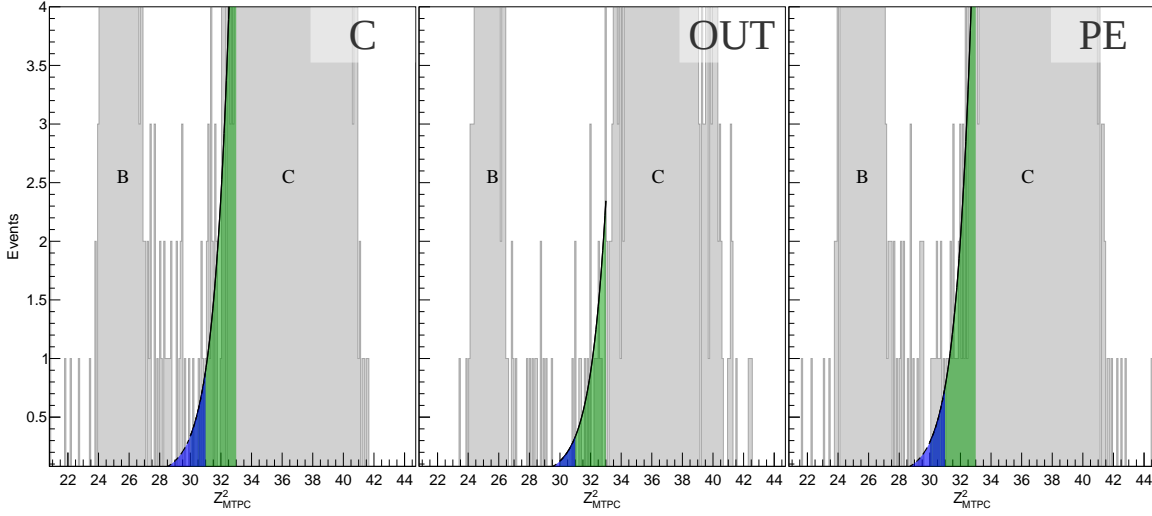
Figure 6.4.: The estimation of the events in the Z^2_{MTPC} tail lost due to the carbon selection cuts. The green shaded region denotes the fit, while the blue shaded region is the extrapolation of the fit line used to determine the number of lost events.

well. To estimate the number of ^{12}C affecting the boron distribution, the integral of the fit function is determined in the Z^2_{MTPC} range used to select boron fragments in the MTPC, which is $22.5 \leq Z^2_{\mathrm{MTPC}} \leq 27.5$. This number is denoted as $\Delta N_{10\mathrm{B}}$, and is used to determine the true number of ^{10}B. The correction factor $\epsilon_{10\mathrm{B}}$ in this case is calculated as,

$$\epsilon_{10\mathrm{B}} = \frac{N^{\mathrm{m}}_{10\mathrm{B}}}{N^{\mathrm{m}}_{10\mathrm{B}} - \Delta N_{10\mathrm{B}}}. \tag{6.25}$$

The expression for the true number of ^{10}B $N^{\mathrm{true}}_{10\mathrm{B}}$ is similar to Eq. (6.23), and is written as,

$$N^{\mathrm{true}}_{10\mathrm{B}} = \frac{N^{\mathrm{m}}_{10\mathrm{B}}}{\epsilon_{10\mathrm{B}}}. \tag{6.26}$$

Correction factors $\epsilon_{12\mathrm{C}}$ and $\epsilon_{10\mathrm{B}}$ for the three target settings are tabulated in Tab. 6.2. Correction factor for accounting the loss of ^{10}B from the boron selection cuts was determined to be negligibly small ($< 0.01\%$), and hence its impact on the cross section is insignificant compared to other corrections that will discussed in the following sections.

The systematic uncertainty arising from this correction is calculated from the statistical uncertainty on $\Delta N_{12\mathrm{C}}$. The individual corrections to the mass changing cross sections of ^{12}C and the systematic uncertainties are tabulated in Tab. 6.3.

Table 6.2.: Correction factors for ^{12}C and ^{10}B calculated as per Eq. (6.24) and Eq. (6.25) respectively.

Target	ϵ_{12C}	ϵ_{10B}
PE	0.999934	1.000905
C	0.999914	1.001502
OUT	0.999901	1.004184

Table 6.3.: The correction $\Delta\sigma$ for mass-changing, charge changing, and ^{10}B production cross sections from the track selection cuts along with the corresponding systematic uncertainty $\delta\sigma$.

Reaction	Mass-changing		Charge-changing		^{10}B production	
	$\Delta\sigma$ (mb)	$\delta\sigma$ (mb)	$\Delta\sigma$ (mb)	$\delta\sigma$ (mb)	$\Delta\sigma$ (mb)	$\delta\sigma$ (mb)
^{12}C+PE	+0.55	±0.60	+0.56	±0.57	+0.04	±0.15
^{12}C+C	+0.13	±0.32	+0.14	±0.33	+0.02	±0.09
^{12}C+p	+0.21	±0.13	+0.21	±0.12	+0.01	±0.04

6.6.2. Feed-down due to Beam Impurities

The purity of the beam is defined as the ratio of the number of wanted nuclei, which in this case is ^{12}C, to the total number of particles selected in the upstream cuts. Hence, other neighboring nuclei like ^{14}N, ^{15}N, ^{13}C, etc. are the beam impurities that can fragment into the lighter nuclei. Their feed-down to relevant isotopes of interest like ^{11}C needs to be calculated and corrected in the final computation of the production cross-section. The impact of these beam impurities depends on the fraction of number of events after the upstream selection. The upstream cut described in Sec. 5.1.1 is optimized such as to select ^{12}C as the primary beam particle. Nevertheless, the shape of the fragment distribution in the *tof* vs Z_{S1}^2 plot allows the neighboring isotopes to pass the selection cut. These nuclei along with ^{12}C constitute the composite beam and interact with the target material generating additional feed-down to the fragments of interest.

Let N_b be the total number of particles in the composite beam. Then N_{12C} represents the number of ^{12}C nuclei present in the beam composition, after the upstream selection procedure is performed. The number corresponding to impurity beam particle 'i' is determined from the fit performed to the upstream distribution of fragments Fig. 4.1. The fraction of ^{12}C nuclei in the upstream cut is given by $f_{12C} = \frac{N_{12C}}{N_b}$, and the fraction of 'i',

neighboring ^{12}C is given by, $f_i = \frac{N_i}{N_b}$. Then it immediately follows that,

$$N_{12C} + \sum_i N_i = N_b \tag{6.27a}$$

$$f_{12C} + \sum_i f_i = 1 \tag{6.27b}$$

Let N_f^m be the total number of fragments of type 'f' produced in the beam-target interaction and as measured in the MTPC. Then it can be expressed as a sum of nuclei 'f' produced from the fragmentation of ^{12}C, and the contribution from the feed-down of all the impurity nuclei 'i', as,

$$N_f^m = N_{12C \to f} + \sum_i N_{i \to f}. \tag{6.28}$$

The quantity $N_{i \to f}$ is the number of nuclei 'f' produced as a result of the fragmentation of the impurity nucleus 'i'. It is determined by counting the number of 'f' tracks in the MTPC by the auxiliary measurement of the impurity nuclei. In that case, the corresponding production probability is written exactly in the form of Eq. (6.1), as, $P_{i \to f} = N_{i \to f}/N_i$. Thus we can divide Eq. (6.28) on both sides by the total number of beam particles, N_b to obtain the measured production probability P_f^m, as,

$$P_f^m = \frac{N_f^m}{N_b} = \left(\frac{N_{12C} P_{12C \to f}^{true} + \sum_i N_i P_{i \to f}}{N_b} \right) \tag{6.29}$$

The probability $P_{12C \to f}^{true}$ on the right side of Eq. (6.29) is the true production probability of nucleus 'f' from ^{12}C+T interactions. Therefore, making the necessary substitutions for the fraction of beam nuclei, and solving Eq. (6.29) for the true probability, we obtain the final expression as,

$$P_{12C \to f}^{true,T} = \left(\frac{P_f^m - \sum_i f_i P_{i \to f}}{f_{12C}} \right) \tag{6.30}$$

The auxiliary probabilities are calculated from the number of measured beam and fragments tracks in the MTPC-L tabulated in Appendix A.3. The equation derived above is employed to correct for and measure the isotope production cross sections, studied in this analysis. For applying this correction to the mass-, and charge-changing probabilities,

Table 6.4.: Relative fractions of neighboring impurity nuclei for the optimized upstream selection of ^{12}C described in Sec. 5.1.1.

Impurity (i)	fraction (f_i, %)
^{15}N	7×10^{-2}
^{14}N	2×10^{-1}
^{13}C	8×10^{-4}
^{11}C	2×10^{-1}
^{11}B	7×10^{-3}
	$\sum_i f_i = 5 \times 10^{-1}$

Eq. (6.30) get modified with additional terms quantifying the feed-down of impurity nuclei 'i' to ^{12}C. These will cause a surplus in the number of ^{12}C tracks as measured in the MTPC-L, thereby altering the cross section value. It can be written in the form similar to that of Eq. (6.28) as follows:

$$N_{12C}^{m} = N_{12C}^{true} + \sum_i N_{i \to 12C}^{m}. \tag{6.31}$$

The number of MTPC measured ^{12}C can be replaced by the product of the corresponding probabilities and the number of nuclei 'i' in the beam composition. Since the first term is the true number of ^{12}C that reach the MTPC, it will be expressed in terms of the survival probability, $P_{12C \to 12C}^{true}$, while the the second term will contain the feed-down probabilities $P_{i \to 12C}$. Furthermore, on dividing Eq. (6.31) by the total number of beam particles N_b results in the survival probability of ^{12}C, written as,

$$P_{12C \to 12C}^{m} = \left(\frac{N_{12C} P_{12 \to 12C}^{true} + \sum_i N_i P_{i \to 12C}}{N_b} \right). \tag{6.32}$$

The quantities N_{12C} and N_i are the number of ^{12}C and nuclei 'i', present in the beam composition. After re-substituting and re-arranging the terms in Eq. (6.32), the final expression for the corrected mass or charge-changing probability can be written in the

Table 6.5.: Correction $\Delta\sigma$ to the mass-, and charge-changing cross sections from feed-down due to beam impurities. The corresponding systematic uncertainty $\delta\sigma$ is given in the columns adjacent to the correction.

Reaction	Mass-changing		Charge-changing	
	$\Delta\sigma$ (mb)	$\delta\sigma$ (mb)	$\Delta\sigma$ (mb)	$\delta\sigma$ (mb)
^{12}C+PE	+0.15	±0.03	+0.37	±0.13
^{12}C+C	+0.09	±0.04	+0.23	±0.12
^{12}C+p	+0.03	±0.01	+0.07	±0.01

form of Eq. (6.30) as follows:

$$
P^{\text{true}}_{^{12}\text{C}\rightarrow^{12}\text{C}} = \left(\frac{P^{\text{m}}_{^{12}\text{C}\rightarrow^{12}\text{C}} - \sum_i f_i P_{i\rightarrow^{12}\text{C}}}{f_{^{12}\text{C}}} \right)
\tag{6.33}
$$

This correction introduces a systematic uncertainty on the measurement. It is calculated from the statistical uncertainty of the auxiliary measurements. The correction factors and the resultant systematic uncertainties are for the mass-changing and charge cross sections are tabulated in Tab. 6.5, and similarly for the individual isotope production measurements in Tab. 6.6.

6.6.3. Re-interaction inside the Target

The nuclear interaction length λ of the fragments produced in the beam-target interaction is ~10% of the target thickness d_{T}. Therefore, there is a small yet finite probability that the nuclear fragments produced inside the target can inelastically re-interact with the target itself. This leads to the underestimation of the number of produced fragment nuclei as measured in the MTPC, altering the final production cross-section. In this case, the

Table 6.6.: Same as Tab. 6.5 for isotope production.

Reaction	^{11}C		^{11}B		^{10}B	
	$\Delta\sigma$ (mb)	$\delta\sigma$ (mb)	$\Delta\sigma$ (mb)	$\delta\sigma$ (mb)	$\Delta\sigma$ (mb)	$\delta\sigma$ (mb)
^{12}C+PE	+0.37	±1.10	+0.35	±1.19	+0.18	±0.96
^{12}C+C	+0.17	±0.64	+0.16	±0.70	+0.08	±0.55
^{12}C+p	+0.09	±0.22	+0.10	±0.25	+0.04	±0.20

measured interaction probability corresponds to two consecutive interactions for the reaction sequence, $b + T \rightarrow f$ & $f + T \rightarrow X$ and can be mathematically expressed as a convolution of the two interaction probabilities. Consider a beam composed of a single
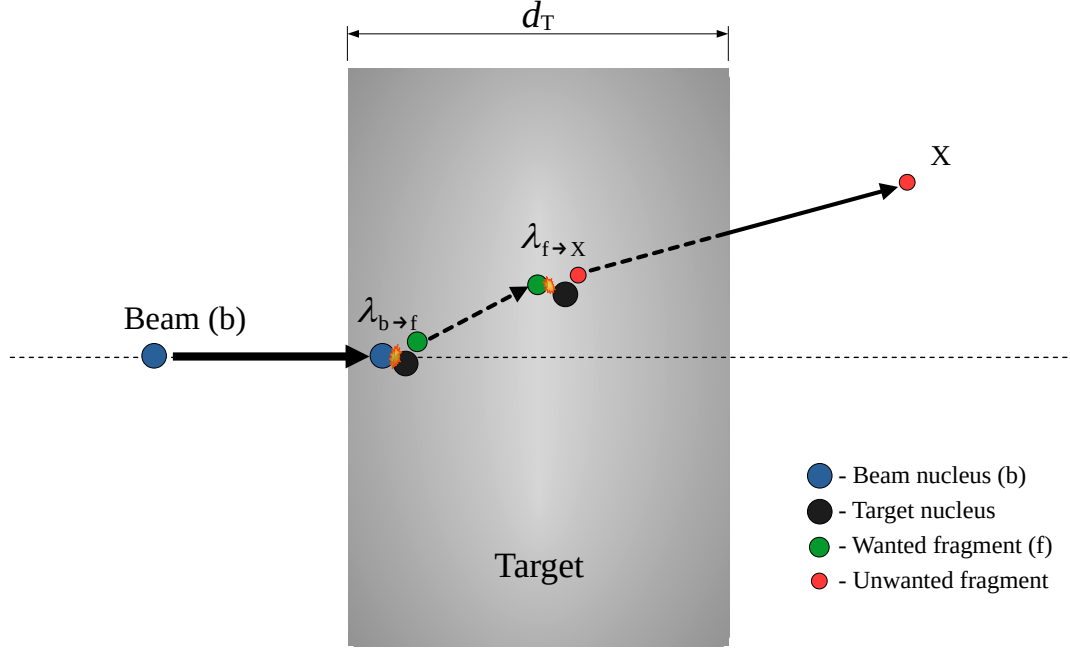

Figure 6.5.: An illustration of the beam nucleus fragmenting to the nucleus of interest (wanted nucleus), which then further interacts inside the target.

type of nucleus, 'b' ‚, and let N_b be the total number of beam particles incident on the target (T) of thickness d_T. Then the rate of inelastic interactions per unit length interval dx of the target is given by,

$$\frac{dN_b(x)}{dx} = -\frac{N_b(x)}{\lambda_{b \rightarrow X}}, \tag{6.34}$$

where λ_b is the interaction length of nucleus 'b' for a given target material and the negative sign denotes the destruction of particles. If nucleus 'b' fragments to 'f', then the differential equation describing the production and destruction of nucleus type 'f' in a length interval dx is given by,

$$\frac{dN_f(x)}{dx} = \frac{N_b(x)}{\lambda_{b \rightarrow f}} - \frac{N_f(x)}{\lambda_f} \tag{6.35}$$

The second term denotes the inelastic interaction of nucleus 'f' inside the target, and hence additional measurements of nucleus 'f' as primary beam particles are required for this

calculation. This is an implicit assumption and is provided by the auxillary measurements. For a composite beam with more than one type of nucleus, Eq. (6.35) can be written in vector notation as,

$$\frac{d\vec{N}(x)}{dx} = M\vec{N}(x) \tag{6.36}$$

Here, $\vec{N}(x)$ is a vector of the number of particles at any given distance x inside the target. For convenience of notation, we introduce a matrix M comprising of the inverse of the interaction lengths relevant for the production of a given nuclei 'f', based on the matrix formulation given in Ref. [6], adopted from the works of [80] (from Eq.(10) onwards). The matrix M for the reaction b→f is a lower triangular matrix expressed as,

$$M = \begin{pmatrix} 1/\lambda_{b\to b} & 0 \\ 1/\lambda_{b\to f} & -1/\lambda_{f\to f} \end{pmatrix}. \tag{6.37}$$

Then the solution to the first order linear differential equations gives the number of particles N_b and N_f respectively, at a given distance x inside the target, and is written as,

$$\vec{N}(x) = \vec{N}(0)\exp(Mx). \tag{6.38}$$

Here vector $\vec{N}(x)$ corresponds to the number of particles at a distance x along the length of the target and $\vec{N}(0)$ is the number of particles incident on the surface of the target, at $x = 0$. For an inelastic interaction of a nucleus 'b' inside the target of thickness d_T, the matrix M contains a single element $M_{b\to b} = -1/\lambda_{b\to b}$ corresponding to the interaction length of nucleus 'b'. Hence Eq. (6.38) reduces to the following form,

$$-\frac{1}{\lambda_{b\to b}} = M_{b\to b} = \frac{1}{x}\ln\frac{N_b(x)}{N_b(0)}, \tag{6.39}$$

Let us consider the reaction b→f concerning the production of 'f' from nucleus 'b' interacting inside the target material. In this case, the matrix M is a lower triangular matrix containing the inelastic interaction lengths of nuclei 'b' and 'f', the interaction length leading to the production of 'f' from 'b', $\lambda_{b\to f}$. Therefore, Eq. (6.38) can be written as,

$$\begin{pmatrix} N_b(x) \\ N_f(x) \end{pmatrix} = \exp\begin{pmatrix} -1/\lambda_b & 0 \\ 1/\lambda_{b\to f} & -1/\lambda_f \end{pmatrix}\begin{pmatrix} N_b(0) \\ 0 \end{pmatrix}. \tag{6.40}$$

The left-hand side in the equation above represents the matrix of the number of nuclear particles 'b' and 'f' at a distance x inside the target, whereas the beam composition is represented by the column matrix on the right. We have assumed a pure beam consisting of only a single type of nucleus 'b', the initial number of which is $N_b(0)$, while in principle, the presence of beam impurities is inevitable. The quantity of interest for our measurement is $\lambda_{b\to f}$ which can be determined by evaluating the exact solution of the exponential form of the matrix M and is written as,

$$\frac{1}{\lambda_{b\to f}} = \frac{M_{f\to f} - M_{b\to b}}{\exp(x \cdot M_{f\to f}) - \exp(x \cdot M_{b\to b})} \left(\frac{N_f(x)}{N_b(0)}\right). \tag{6.41}$$

This equation gives the true in-target interaction length for the production of nucleus 'f'. It is further used to correct the calculated production cross-section of the isotopes, where f=^{11}C, ^{11}B and ^{10}B. The expression for $\lambda_{b\to f}$ derived above requires additional measurement of the inelastic interaction probability of nucleus 'f'.

The ratio $N_f(x)/N_b(0)$ is essentially the measured probability of production of the nucleus 'f' inside the target T, and is written as $P_{b\to f}^{\text{meas.,T}}$. It is the same as the production probability $P_{b\to f}^{T}$ given in Eq. (6.19). In addition to that, two other inputs required for this correction are the mass-changing interaction probabilities, or rather the total survival probability of the beam 'b' and the fragment nucleus 'f' represented by the matrix elements $M_{b\to b}$ and $M_{f\to f}$ respectively. These probabilities are measured using Eq. (6.4). Substituting the interaction length in Eq. (6.41) as $\lambda_{b\to f} = n_T \sigma_{b\to f}^{\text{true,T}}$ gives the following equation:

$$\sigma_{b\to f}^{\text{true,T}} = \frac{1}{n_T d_T} \left(\frac{\ln P_{f\to f}^{T} - \ln P_{b\to b}^{T}}{P_{f\to f}^{T} - P_{b\to b}^{T}}\right) P_{b\to f}^{\text{meas.,T}}. \tag{6.42}$$

Substituting the required probabilities in the expression above results in the corrected production cross section of nucleus 'f' before it undergoes an inelastic interaction inside the target. Analogous to the previous correction described previously in Sec. 6.6.2, the systematic uncertainty resulting from this correction is facilitated by the auxiliary measurements of nucleus 'b' and 'f'. It is calculated from the statistical uncertainty in the measured values of $P_{b\to b}^{T}$ and $P_{f\to f}^{T}$.

Table 6.7.: Correction $\Delta\sigma$ with the systematic uncertainty $\delta\sigma$ due to inelastic interaction of the wanted nuclei inside the target.

Reaction	^{11}C		^{11}B		^{10}B	
	$\Delta\sigma$ (mb)	$\delta\sigma$ (mb)	$\Delta\sigma$ (mb)	$\delta\sigma$ (mb)	$\Delta\sigma$ (mb)	$\delta\sigma$ (mb)
^{12}C+PE	+6.68	±0.51	+9.29	±1.25	+4.47	±0.41
^{12}C+C	+2.72	±0.22	+2.75	±0.52	+1.62	±0.18
^{12}C+p	+1.98	±0.14	+3.26	±0.37	+1.42	±0.12

Table 6.8.: The uncertainty in the measured mass-changing, and charge-changing and production cross sections due to uncertainty in the target density.

Reaction	Mass-changing	Charge-changing	^{11}C	^{11}B	^{10}B
	$\delta\sigma$ (mb)	$\delta\sigma$ (mb)	$\delta\sigma$ (mb)	$\delta\sigma$ (mb)	$\delta\sigma$ (mb)
^{12}C+PE	±1.23	±1.11	±0.10	±0.10	±0.05
^{12}C+C	±4.86	±4.52	±0.27	±0.29	±0.13
^{12}C+p	±2.51	±2.33	±0.14	±0.15	±0.07

6.6.4. Target Density Uncertainty

The cross section depends on the mass density ρ of the target material. Therefore, uncertainty in the mass densities of both the targets, PE and C, contribute to the total systematic of the measurement and needs to be taken into account for calculating the individual cross section values. The graphite target (C) is a replica of the T2K thin target with a known mass density of $\rho_C = 1.840 \, \text{g/cm}^3$. The uncertainty in the density of the C target is $\delta\rho_C = 0.65\%$ [81].

Similarly, for the polyethylene target with density $\rho_{PE} = 0.924 \, \text{g/cm}^3$, the corresponding uncertainty is $\delta\rho_{PE} = 0.1\%$. It is calculated as the average from the measurements of the mass and the dimensions of the target [82]. These uncertainties are propagated in Eq. (6.21) to compute its effect on the measured cross sections. Uncertainties for the mass-,charge-changing and the isotope production for all three reactions are tabulated in Tab. 6.8.

7. Cross Section Results

The cross section values for the ^{12}C mass-, charge-changing, and production of carbon and boron isotopes are calculated according to the analysis formalism developed in Ch. 6.

Results from the calculation of the ^{12}C mass-, charge-changing and the production cross section of the isotopes ^{11}C, ^{11}B, and ^{10}B for the three targets, namely PE, C and proton (p), are discussed in this chapter. A summary of the measurements with the correction and systematic uncertainties as derived in Sec. 6.6 is tabulated for each of reaction in the subsequent sections.

7.1. Mass- and Charge-changing Cross Sections

The mass- and charge-changing results measured in this analysis, including contributions from the calculated corrections and systematic uncertainties are summarized in Tab. 7.1 and Tab. 7.2, respectively. The results for the ^{12}C+p mass-changing cross section is shown in Fig. 7.1, and that for ^{12}C+PE and ^{12}C+C reactions are shown in Fig. 7.2. The charge-changing results are also shown on the plot, along with previously measured values of the cross-sections. Results obtained in this analysis are in good agreement with previous studies and the model lines. Previous measurements of the charge-changing cross sections (open circles), and the mass-changing cross sections (open squares) at lower momenta are shown as well [83–87]. Abundance of data at lower momenta ($p \leq 1A\,\mathrm{GeV}/c$) is mainly attributed to its application in radiation therapy at clinical centers. It is interesting to note that, unlike the ^{12}C mass-changing cross sections, there are no available charge-changing measurements for $p > 10A\,\mathrm{GeV}/c$, apart from the cross section result from this analysis.

The total reaction cross section along with the charge-changing cross section of the C nucleus has been the focus of numerous previous studies. Proton-nucleus inelastic interaction cross section has been measured by many groups ([42, 88–90]) including NA61. These measurements were performed at different beam momenta, using a proton beam

impinging on a fixed graphite target. The primary interest in studying these nuclear reactions was to understand the propagation of Galactic cosmic rays and transport of protons in the atmosphere and also to study the irradiation effects on matter. The data shows a momentum dependence of the cross section at momentum $p_A < 2\,\text{GeV}/c$, while at higher momenta ($p_A > 10\,\text{GeV}/c$) the behavior is approximately asymptotic. Previous NA61 measurements using a proton beam on a graphite target were performed at $31A\,\text{GeV}/c$, $60A\,\text{GeV}/c$, and $120A\,\text{GeV}/c$ beam momenta.

The superimposing lines in Fig. 7.1 correspond to parameterization function modeling the momentum dependence of the cross section at low as well as high energies, taken from Ref. [91] (Letaw+83), and Ref. [92] (Wellisch+96), and Ref. [93] (Barashenkov+94). Cross section parameterization of lighter nuclei starting from $p \approx 10\,\text{MeV}/c$, are studied in the works of [91]. The model lines shown in Fig. 7.2 correspond to different cross-section parameterization formula as described in Refs. [94–96] and is adapted from Ref. [97].

The measurement is dominated by the statistical uncertainty at $\sim 3 - 5\%$ of the derived cross section values. Systematic uncertainties arising from various corrections are calculated as described in Sec. 6.6, the maximum of which comes from the uncertainty in the target density. It is estimated to be approximately $10 - 20\%$ of the statistical uncertainty. As in the case of the mass-changing cross section, the ^{12}C charge-changing measurement is dominated by statistics, while the largest systematic uncertainty is due to the uncertainty in the target density.

Table 7.1.: Summary of the mass-changing cross section of ^{12}C including the corrections and their systematic uncertainties as described and computed in Sec. 6.6.

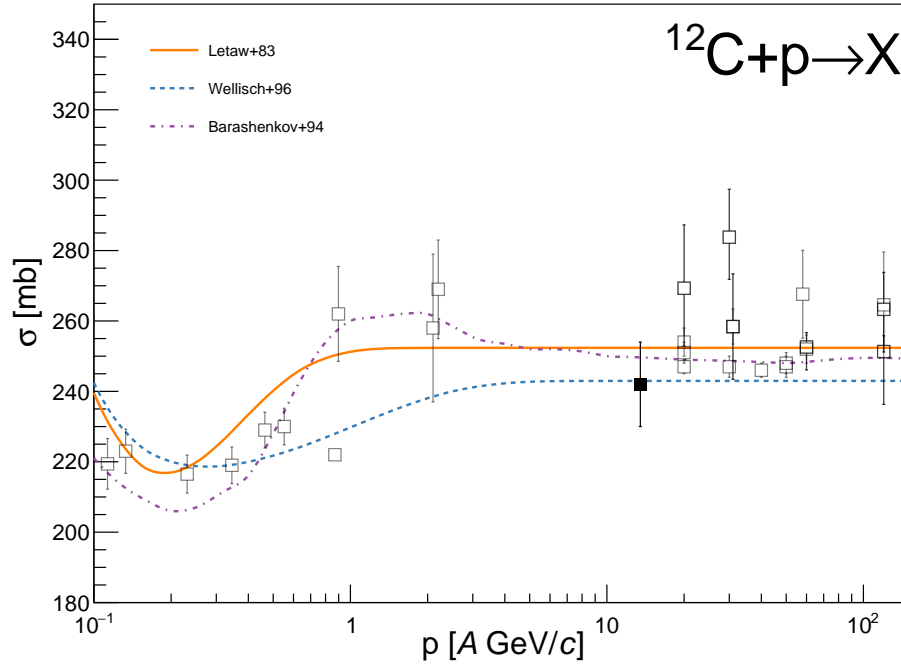|	^{12}C+PE		^{12}C+C		^{12}C+p	
Uncorrected σ (mb)	1230.7 ± 35.8		746.6 ± 23.4		242.1 ± 12.8	
	$\Delta\sigma$ (mb)	$\delta\sigma^{\text{syst.}}$ (mb)	$\Delta\sigma$ (mb)	$\delta\sigma^{\text{syst.}}$ (mb)	$\Delta\sigma$ (mb)	$\delta\sigma^{\text{syst.}}$ (mb)
Carbon Selection	+0.6	±0.6	+0.1	+0.3	+0.2	±0.1
Beam Impurity	+0.2	±0.0	+0.1	±0.0	+0.0	±0.0
Target density	-	±1.2	-	±4.9	-	±2.5
Corrected σ (mb)	$1232 \pm 36 \pm 1$		$747 \pm 23 \pm 5$		$242 \pm 13 \pm 3$	

Figure 7.1.: The ^{12}C+p mass-changing cross-section computed in this analysis (solid square) along with previously reported values (open squares). The lines represent various momentum-dependent parameterizations of the cross-section take n from [91–93].

Table 7.2.: Same as Tab. 7.1 for the total charge-changing cross section of ^{12}C.

	^{12}C+PE		^{12}C+C		^{12}C+p	
Uncorrected σ (mb)	1116.4 ± 35.5		694.1 ± 23.2		211.1 ± 12.5	
	$\Delta\sigma$ (mb)	$\delta\sigma^{\text{syst.}}$ (mb)	$\Delta\sigma$ (mb)	$\delta\sigma^{\text{syst.}}$ (mb)	$\Delta\sigma$ (mb)	$\delta\sigma^{\text{syst.}}$ (mb)
Carbon Selection	+0.6	±0.6	+0.1	+0.3	+0.2	±0.1
Beam Impurity	+0.4	±0.1	+0.2	±0.1	+0.1	±0.0
Target density	-	±1.1	-	±4.5	-	±2.3
Corrected σ (mb)	1117 ± 36 ± 1		695 ± 23 ± 5		211 ± 13 ± 2	

7.2. Isotope Production Cross Sections

Cross sections of the production of carbon and boron isotopes measured in this analysis are summarized in Tab. 7.3 for ^{11}C, in Tab. 7.4 for ^{11}B, and in Tab. 7.5 for ^{10}B. The individual corrections and the systematic uncertainty related to it as calculated in Sec. 6.6 are listed in the tables. Similar to mass-, and charge changing results discussed in the previous sections, the isotope production cross sections are too, dominated by the statistical uncertainty, at approximately 10% of the measurement. whereas the total systematic uncertainty is $\simeq 1\%$
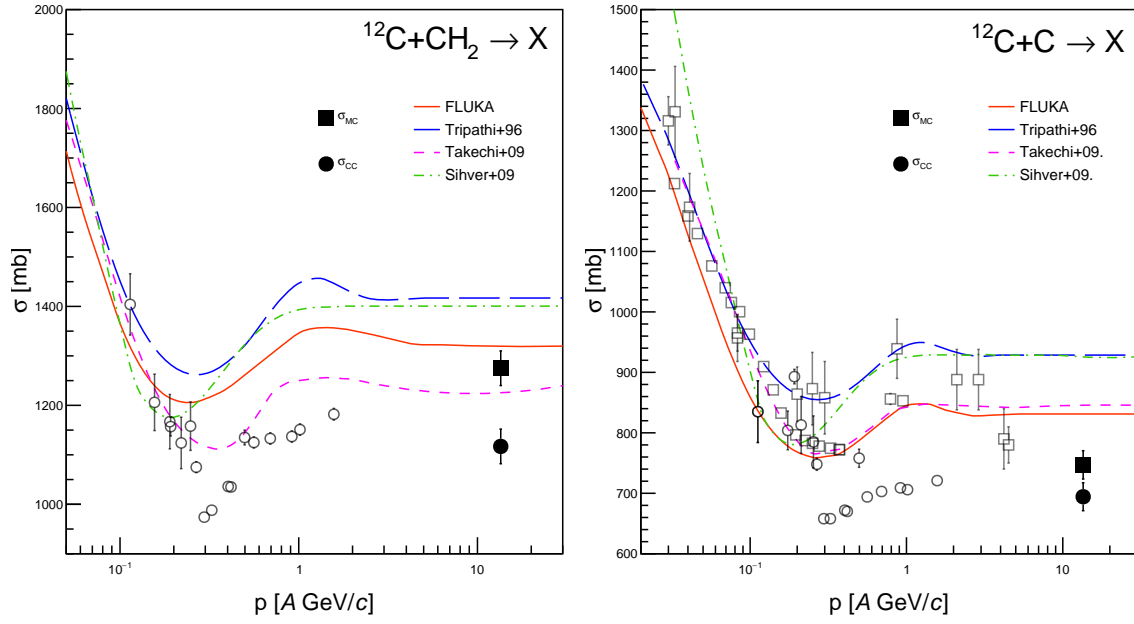
Figure 7.2.: The measured ^{12}C charge-changing (σ_{CC}, solid circle) and mass-changing (σ_{MC}, solid square) cross-section result from this work, on CH_2 (left) and C (right) targets, with previous measurements of charge-changing (open circles), and mass-changing cross sections (open squares). Four model lines are shown for the mass-changing cross section (see text).

of the derived cross section values. Largest contribution to the systematic uncertainty for ^{11}C and ^{10}B is due to feed-down of the beam impurity nuclei, while that for ^{11}B is related to the in-target annihilation correction of the produced fragment nuclei. Since these uncertainties are calculated from auxiliary measurements of the mass-changing cross sections of the respective isotopes, they are limited by the low statistics available in the data.

Corrected cross sections are displayed with previous measurements in Fig. 7.3. The lines represent cross section parameterization with respect to p_A, and correspond to the models GALPROP12, abbreviated as GP12, developed by [98], WKS98 from the authors of Refs. [99–101], and Evoli+19, as given in [102]. In the approximation that the cross section dependence on p_A reaches an asymptotic value at higher momentum, the results computed in this analysis are consistent with the model lines.

It is intriguing to note that, there is only a single measurement of the isotopic production cross section of ^{11}C at $p > 10A\,\text{GeV}/c$. The study was undertaken by J. Cummings at Brookhaven AGS [103]. The production of ^{11}C was measured in p+ ^{12}C interactions, by irradiating a plastic scintillator target with a proton beam at $p = 28A\,\text{GeV}/c$. The ^{11}C

radioactivity was then measured by studying the internal scintillation to determine the yield and calculate the cross section. A similar high energy measurement was performed in the case of production of boron isotopes from spallation of ^{12}C by protons at $p = 25A\,\mathrm{GeV}/c$ [49]. The measured cross section of the ^{11}B is $(59 \pm 12)\,\mathrm{mb}$ and that for ^{10}B is $(20 \pm 3)\,\mathrm{mb}$. Nevertheless, the reported values correspond to the cumulative cross-sections, including contributions from the decay of ^{11}C and ^{10}C nuclei, and hence are indirect production cross sections, unlike the value reported in this work. Therefore, they are not shown in Fig. 7.3. Combining the production of boron isotopes and the radioactive isotope ^{11}C gives an estimate on the total boron production cross section in ^{12}C+p reactions at momentum $p > 10\,A\,\mathrm{GeV}/c$. The sum of the cross sections measured in this analysis is,

$$\sigma^{\mathrm{total\ B}}_{\mathrm{12C+p}\rightarrow\mathrm{11C,11B,10B}} = (77 \pm 5)\ \mathrm{mb}. \tag{7.1}$$

This value is the total boron production, from ^{12}C+p interaction, including the contribution from the radionuclide ^{11}C. The quoted uncertainty in Eq. (7.1) is the total uncertainty, combining those of the statistical and systematic uncertainty from each measurement. The sum of boron isotope production measurement from [49] is $(79 \pm 12)\,\mathrm{mb}$. Assuming that the correction from the production of ^{10}C is small, this is in good agreement with the cross section computed in this analysis. This pilot measurement, thus, improved the precision of the asymptotic ^{12}C$\rightarrow$B cross section at p_{A} >10$A\,\mathrm{GeV}/c$. The sum of B production in the models used for CR propagation at $13.5A\,\mathrm{GeV}/c$ is $73.5\,\mathrm{mb}$, $68.91\,\mathrm{mb}$, and $69.37\,\mathrm{mb}$ for WKS98, GP12, and Evoli+19, respectively. Therefore, all these models are in reasonable agreement with the results of this analysis.

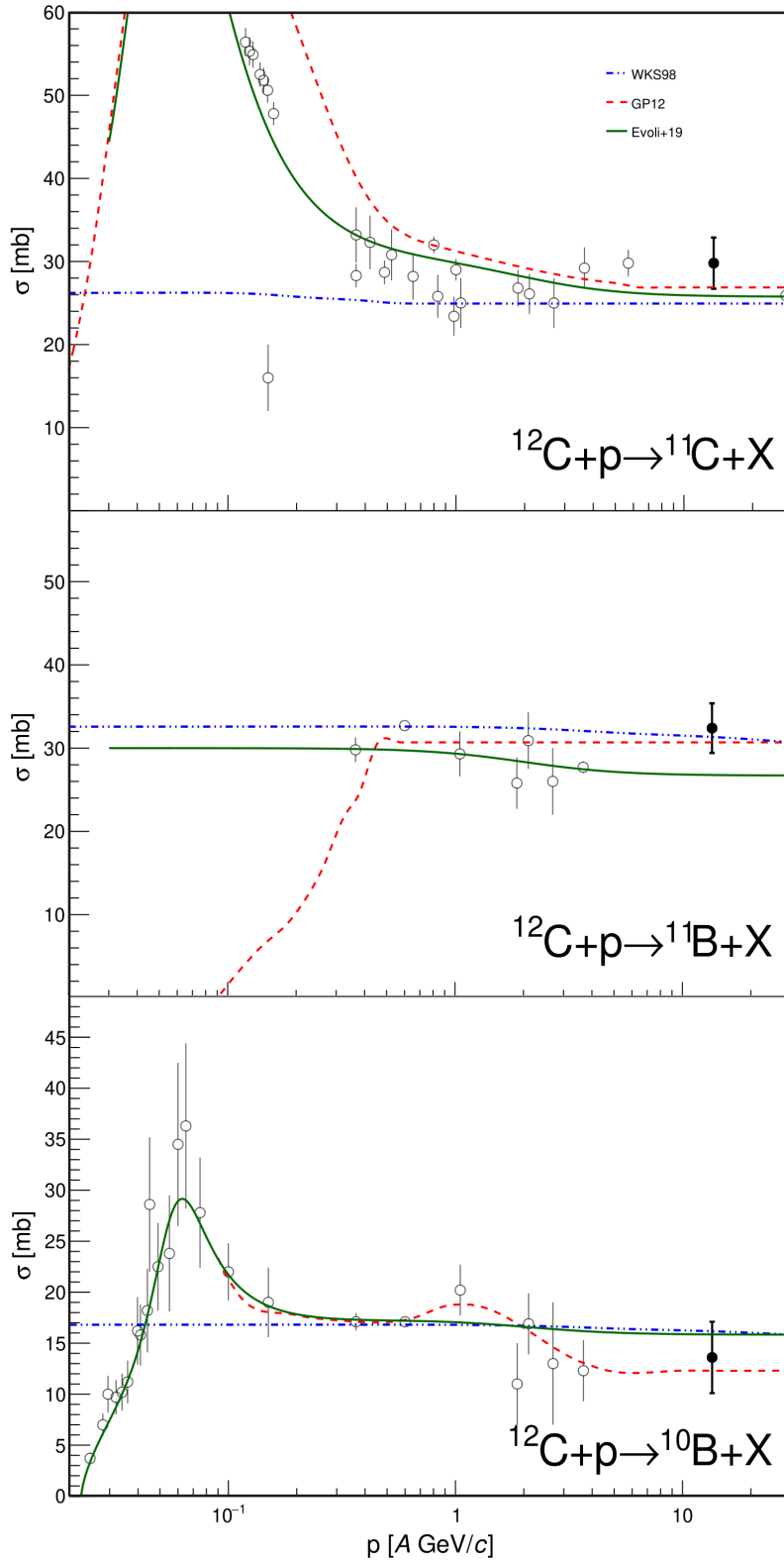Figure 7.3.: The isotope production cross-section of ^{11}C, ^{11}B, and ^{10}B fragment as measured in ^{12}C+p reaction, compared to previous measurements [49, 104–107]. The lines represent the parameterization of the cross section used in calculations of CR transport in the Galaxy [98–102].

Table 7.3.: A summary of the measurement of ^{11}C production in interaction of ^{12}C with PE, C, and proton. The corrections are denoted $\Delta\sigma$ and the systematic uncertainty as $\delta\sigma^{\text{syst.}}$, whereas the statistical uncertainty is quoted with the uncorrected cross section.

	^{12}C+PE		^{12}C+C		^{12}C+p	
Uncorrected σ (mb)	96.8 ± 4.7		41.9 ± 2.8		27.4 ± 2.7	
	$\Delta\sigma$ (mb)	$\delta\sigma^{\text{syst.}}$ (mb)	$\Delta\sigma$ (mb)	$\delta\sigma^{\text{syst.}}$ (mb)	$\Delta\sigma$ (mb)	$\delta\sigma^{\text{syst.}}$ (mb)
Beam Impurity	+0.4	±1.1	+0.2	±0.6	+0.1	±0.2
Target Re-Int.	+6.7	±0.5	+2.7	±0.2	+2.0	±0.1
Target density	-	±0.1	-	±0.3	-	±0.1
Corrected σ (mb)	$104 \pm 5 \pm 1$		$45 \pm 3 \pm 1$		$30 \pm 3 \pm 0$	

Table 7.4.: Same as Tab. 7.3 for the production of ^{11}B.

	^{12}C+PE		^{12}C+C		^{12}C+p	
Uncorrected σ (mb)	103.5 ± 4.7		44.8 ± 2.7		29.4 ± 2.7	
	$\Delta\sigma$ (mb)	$\delta\sigma^{\text{syst.}}$ (mb)	$\Delta\sigma$ (mb)	$\delta\sigma^{\text{syst.}}$ (mb)	$\Delta\sigma$ (mb)	$\delta\sigma^{\text{syst.}}$ (mb)
Beam Impurity	+0.4	±1.2	+0.2	±0.7	+0.1	±0.3
Target Re-Int.	+9.4	±1.3	+2.8	±0.5	+3.4	±0.4
Target density	-	±0.1	-	±0.3	-	±0.2
Corrected σ (mb)	$113 \pm 5 \pm 2$		$48 \pm 3 \pm 1$		$33 \pm 3 \pm 1$	

Table 7.5.: Same as Tab. 7.3 for the production of ^{10}B

	^{12}C+PE		^{12}C+C		^{12}C+p	
Uncorrected σ (mb)	46.6 ± 4.5		20.4 ± 2.8		13.1 ± 2.7	
	$\Delta\sigma$ (mb)	$\delta\sigma^{\text{syst.}}$ (mb)	$\Delta\sigma$ (mb)	$\delta\sigma^{\text{syst.}}$ (mb)	$\Delta\sigma$ (mb)	$\delta\sigma^{\text{syst.}}$ (mb)
Track Selection	+0.0	±0.2	+0.0	±0.1	+0.0	±0.0
Beam Impurity	+0.2	±1.0	+0.1	±0.6	+0.0	±0.2
Target Re-Int.	+4.5	±0.4	+1.6	±0.2	+1.4	±0.1
Target density	-	±0.0	-	±0.1	-	±0.1
Corrected σ (mb)	$56 \pm 4 \pm 1$		$22 \pm 3 \pm 1$		$15 \pm 3 \pm 0$	

8. Summary and Outlook

In this thesis, a measurement of the mass-changing, charge-changing and isotope production cross sections of the nuclear fragments ^{11}C, ^{11}B and ^{10}B in ^{12}C+p interactions at momentum 13.5A GeV/c is presented. The cross sections are determined from the data recorded during a pilot run at NA61/SHINE facility at CERN. The secondary ^{12}C ion beam was produced by fragmenting ^{208}Pb ions from the SPS on a beryllium target and was delivered to the experimental facility via the H2 beamline. The beamline spectrometers were tuned to select $A/Z = 2$ particles to be transported to NA61/SHINE. The online trigger based on dE/dx in the scintillator S1 is used to select carbon particles, and the time-of-flight measured between two scintillators is used to distinguish between the carbon isotopes and make a fit-based offline selection of ^{12}C. A total of 3.2×10^5 events with ^{12}C projectiles were selected for this purpose.

Two thin targets, namely polyethylene (PE) and graphite (C) were employed to determine the fragmentation cross section of the ^{12}C on a proton target. To understand the beam interactions in the experimental setup, $\approx$ 10% of the events were recorded with an empty target holder. Fragment tracks produced in the beam-target interaction are measured in the Time Projection Chamber detectors called the MTPC. Tracks corresponding to different elements are selected based on the charge equivalent energy deposit in the TPCs and the deflection of the fragments in the magnetic fields of the superconducting vertex magnets. To determine the yield of carbon and boron fragments as measured in the MTPC, a binned Poisson log-likelihood fit is performed on the distribution of fragments in the MTPC. The formalism for calculating cross sections is based on the in-target interaction probabilities which are calculated from the measured number of tracks and the number of incident beam particles, for each target setting PE, C, and OUT. Additional corrections were applied to the derived cross sections. These corrections are pertaining to the track selection efficiency, beam particle selection efficiency involving feed down from impurity nuclei in the cut, and loss of the fragment due to interaction in the target. These corrections were calculated

for ^{12}C+PE, ^{12}C and the derived ^{12}C+p cross section for ^{11}C, ^{11}B, and ^{10}C. Moreover, the systematic uncertainties were also calculated in this analysis. The total uncertainty of the measurements presented here is dominated by the statistical uncertainty. The main result of this analysis is the total boron production cross section which was measured to be

$$\sigma^{\text{tot.B}} = \sigma_{12C+p \to (11C+11B+10B)} = (77 \pm 5)\,\text{mb}.$$

This result is in good agreement with a previous measurement at high energy $(79 \pm 12)\,\text{mb}$, but the uncertainty achieved here is approximately less than half as compared to the one in the previous measurement. The predictions of fragmentation models used to interpret cosmic ray data show a reasonable agreement with our measurement within 1.4σ. A preliminary look into the production of Li and Be isotopes demonstrated the feasibility of measuring low mass fragments as well. Furthermore, in addition to the derived cross sections on proton, which is of major interest for cosmic-ray physics, this thesis also provided new measurements on mass- and charge changing cross-sections on carbon and polyethylene targets, which are of potential relevance to particle therapy in medical physics and to space radiation protection.

Given that the aim of the pilot run in 2018 was to test the feasibility of performing nuclear fragmentation studies at NA61/SHINE, the results presented in this thesis demonstrate that, indeed such studies can be performed with the NA61/SHINE facility. A part of the doctorate was spent at CERN to participate in the deployment of new front-end electronic boards for the TPCs as part of the upgrade of the NA61/SHINE detector. This upgrade was successfully finished in 2022 boosting the read out rate from $\approx 100\,\text{Hz}$ to $\approx 1\,\text{kHz}$. Another week of data taking with fragmented beam was planned for 2023 but is now scheduled for the end of this year. With the help of the upgraded data acquisition and an interaction trigger, we can acquire the event statistics for different projectiles such as C, N, O, and Si, required for a precise understanding of light $(A < 28)$ cosmic ray secondaries produced in our Galaxy.

References

[1] O. Adriani et al. In: *The Astrophysical Journal* 791.2, 93 (2014), p. 93. DOI: `10.1088/0004-637X/791/2/93`.

[2] M. Aguilar. In: *Phys. Rev. Lett.* 117 (23 2016), p. 231102. DOI: `10.1103/PhysRevLett.117.231102`.

[3] DAMPE Collaboration. In: *Science Bulletin* 67.21 (2022), pp. 2162–2166. DOI: `10.1016/j.scib.2022.10.002`.

[4] O. Adriani et al. In: *Phys. Rev. Lett.* 129 (25 2022), p. 251103. DOI: `10.1103/PhysRevLett.129.251103`.

[5] M. J. Boschini et al. In: *Astrophys. J. Suppl.* 250.2 (2020), p. 27. DOI: `10.3847/1538-4365/aba901`.

[6] J. Bennemann. MA thesis. Karlsruher Institut für Technologie (KIT), 2023. DOI: `10.5445/IR/1000164132`.

[7] C. Evoli. Dec. 2020. DOI: `10.5281/zenodo.4396125`.

[8] T. Antoni. In: *Astroparticle Physics* 24.1 (2005), pp. 1–25. DOI: `10.1016/j.astropartphys.2005.04.001`.

[9] K.-H. Kampert and M. Unger. In: *Astroparticle Physics* 35.10 (2012), pp. 660–678. DOI: `https://doi.org/10.1016/j.astropartphys.2012.02.004`.

[10] J. R. Hörandel. In: *Journal of Physics: Conference Series* 47.1 (2006), p. 41. DOI: `10.1088/1742-6596/47/1/005`.

[11] D. J. Bird et al. In: *Phys. Rev. Lett.* 71 (21 1993), pp. 3401–3404. DOI: `10.1103/PhysRevLett.71.3401`.

[12] R. U. Abbasi et al. In: *Phys. Rev. Lett.* 100 (10 2008), p. 101101. DOI: `10.1103/PhysRevLett.100.101101`.

[13] J. Abraham. In: *Physics Letters B* 685.4 (2010), pp. 239–246. DOI: https://doi.org/10.1016/j.physletb.2010.02.013.

[14] P. O. Lagage and C. J. Cesarsky. In: *Astronomy & Astrophysics* 125 (1983), pp. 249–257.

[15] J. Abraham. In: *Phys. Rev. Lett.* 101 (6 2008), p. 061101. DOI: 10.1103/PhysRevLett.101.061101.

[16] K. Greisen. In: *Phys. Rev. Lett.* 16 (17 1966), pp. 748–750. DOI: 10.1103/PhysRevLett.16.748.

[17] G. T. Zatsepin and V. A. Kuz'min. In: *Soviet Journal of Experimental and Theoretical Physics Letters* 4 (Aug. 1966), p. 78.

[18] M. Aguilar et al. In: *Phys. Rev. Lett.* 115 (21 2015), p. 211101. DOI: 10.1103/PhysRevLett.115.211101.

[19] M. Aguilar et al. In: *Phys. Rev. Lett.* 119 (25 2017), p. 251101. DOI: 10.1103/PhysRevLett.119.251101.

[20] K. A. Lave et al. In: *The Astrophysical Journal* 770.2 (2013), p. 117. DOI: 10.1088/0004-637X/770/2/117.

[21] The AMS-01 Collaboration. In: *arXiv e-prints* (Aug. 2010). DOI: 10.48550/arXiv.1008.5051.

[22] R. P. Murphy et al. In: *The Astrophysical Journal* 831.2 (2016), p. 148. DOI: 10.3847/0004-637X/831/2/148.

[23] B. F. Rauch et al. In: *The Astrophysical Journal* 697.2 (2009), p. 2083. DOI: 10.1088/0004-637X/697/2/2083.

[24] J. J. Beatty, J. Matthews, and S. P. Wakely. https://pdg.lbl.gov/2022/reviews/rpp2022-rev-cosmic-rays.pdf. 2019.

[25] N. Lund. In: *Advances in Space Research* 4.2 (1984), pp. 5–14. DOI: https://doi.org/10.1016/0273-1177(84)90287-4.

[26] K. Ptitsyna and S. V. Troitsky. In: *Physics-Uspekhi* 53.7 (2010), p. 691. DOI: 10.3367/UFNe.0180.201007c.0723.

[27] A. M. Hillas. In: *Annual Review of Astronomy and Astrophysics* 22.Volume 22, 1984 (1984), pp. 425–444. DOI: 10.1146/annurev.aa.22.090184.002233.

[28] T. K. Gaisser, R. Engel, and E. Resconi. *Cosmic Rays and Particle Physics*. 2016.

[29] E. Fermi. "On the Origin of the Cosmic Radiation". In: *Phys. Rev.* 75 (8 1949), pp. 1169–1174. DOI: `10.1103/PhysRev.75.1169`.

[30] W. I. Axford, E. Leer, and G. Skadron. In: *International Cosmic Ray Conference*. Vol. 11. International Cosmic Ray Conference. 1977, p. 132.

[31] G. F. Krymskii. In: *Akademiia Nauk SSSR Doklady* 234 (1977), pp. 1306–1308.

[32] A. R. Bell. In: *MNRAS* 182 (1978), pp. 147–156. DOI: `10.1093/mnras/182.2.147`.

[33] R. D. Blandford and J. P. Ostriker. In: *The Astrophysical Journal* 221 (1978), pp. L29–L32. DOI: `10.1086/182658`.

[34] M. Longair. *High Energy Astrophysics 3rd Edition*. 1981. DOI: `10.1017/CBO9780511778346`.

[35] V. S. Berezinskii et al. *Astrophysics of Cosmic Rays*.

[36] M. Garcia-Munoz et al. In: *Astrophysics Journal* 64 (May 1987), p. 269. DOI: `10.1086/191197`.

[37] I. V. Moskalenko et al. In: *The Astrophysical Journal* 586.2 (2003), p. 1050. DOI: `10.1086/367697`.

[38] F. Donato, D. Maurin, and R. Taillet. In: *Astronomy & Astrophysics* 381 (Jan. 2002), pp. 539–559. DOI: `10.1051/0004-6361:20011447`.

[39] F. Sutter. "Messung der Fragmentation von Kohlenstoff zu Bor bei einer Energie von 13.5A GeV/c". Masterarbeit. Karlsruher Institute für Technologie, 2019. 2019.

[40] L. W. Townsend and J. W. Wilson. `https://www.osti.gov/biblio/6857597`.

[41] R. Glauber. 1959. DOI: `https://archive.org/details/in.ernet.dli.2015.177153/page/n325/mode/2up`.

[42] S. Denisov et al. In: *Nucl. Phys.* B61 (1973), p. 62. DOI: `10.1016/0550-3213(73)90351-9`.

[43] G. D. Westfall et al. In: *Phys. Rev. C* 19 (4 1979), pp. 1309–1323. DOI: `10.1103/PhysRevC.19.1309`.

[44] G Tibell. *High-energy physics and nuclear structure. Proceedings of the fifth international conference, Uppsala, Sweden, June 18–22, 1973*. `https://www.osti.gov/biblio/4282442`.

[45] H. Feshbach and K. Huang. In: *Physics Letters B* 47.4 (1973), pp. 300–302. DOI: https://doi.org/10.1016/0370-2693(73)90607-2.

[46] A. Goldhaber. In: *Physics Letters B* 53.4 (1974), pp. 306–308. DOI: https://doi.org/10.1016/0370-2693(74)90388-8.

[47] C. Evoli et al. In: *Phys. Rev. D* 101 (2 2020), p. 023013. DOI: 10.1103/PhysRevD.101.023013.

[48] Y. Génolini et al. In: *Phys. Rev. C* 98 (3 2018), p. 034611. DOI: 10.1103/PhysRevC.98.034611.

[49] P. Fontes. In: *Phys. Rev. C* 15 (6 1977), pp. 2159–2168. DOI: 10.1103/PhysRevC.15.2159.

[50] Y. Génolini et al. In: *arXiv e-prints* (2023), arXiv:2307.06798. DOI: 10.48550/arXiv.2307.06798.

[51] M. Aguilar. In: *Phys. Rev. Lett.* 126 (8 2021), p. 081102. DOI: 10.1103/PhysRevLett.126.081102.

[52] M.-J. Zhao, X.-J. Bi, and K. Fang. In: *Phys. Rev. D* 107.6, 063020 (2023), p. 063020. DOI: 10.1103/PhysRevD.107.063020. arXiv: 2209.03799 [astro-ph.HE].

[53] D. Maurin et al. In: *Astronomy & Astrophysics* 668, A7 (2022), A7. DOI: 10.1051/0004-6361/202243446.

[54] E. F. Bueno et al. In: *arXiv e-prints* (2022). DOI: 10.48550/arXiv.2208.01337. eprint: 2208.01337.

[55] N. Weinrich et al. In: *Astron. Astrophys.* 639 (2020), A131. DOI: 10.1051/0004-6361/202037875.

[56] A. W. Strong and I. V. Moskalenko. In: *The Astrophysical Journal* 509.1 (1998), pp. 212–228. DOI: 10.1086/306470.

[57] W. R. Webber and A. Soutoul. In: *The Astrophysical Journal* 506.1 (1998), p. 335. DOI: 10.1086/306224.

[58] P. Lipari. In: (2022). DOI: https://doi.org/10.48550/arXiv.2204.13085. arXiv: 13085 [astro-ph.HE].

[59] O. Adriani et al. In: *Nature* 458 (2009), pp. 607–609. DOI: 10.1038/nature07942. arXiv: 0810.4995 [astro-ph].

[60] M. t. Ackermann. In: *Phys. Rev. Lett.* 108 (1 2012), p. 011103. DOI: `10.1103/PhysRevLett.108.011103`.

[61] L. Accardo. In: *Phys. Rev. Lett.* 113 (12 2014), p. 121101. DOI: `10.1103/PhysRevLett.113.121101`.

[62] C. M. Karwin et al. In: *The Astrophysical Journal* 880.2 (2019), p. 95. DOI: `10.3847/1538-4357/ab2880`.

[63] C. M. Karwin et al. In: *Phys. Rev. D* 103.2, 023027 (2021), p. 023027. DOI: `10.1103/PhysRevD.103.023027`. arXiv: `2010.08563 [astro-ph.HE]`.

[64] A.-K. Burns et al. In: *Phys. Rev. D* 103.6, 063023 (2021), p. 063023. DOI: `10.1103/PhysRevD.103.063023`. arXiv: `2010.11650 [astro-ph.HE]`.

[65] M. Aguilar et al. In: *Phys. Rev. Lett.* 117 (9 2016), p. 091103. DOI: `10.1103/PhysRevLett.117.091103`.

[66] N. Abgrall et al. In: *JINST* 9 (2014), P06005. DOI: `10.1088/1748-0221/9/06/P06005`. arXiv: `1401.4699 [physics.ins-det]`.

[67] E. Lopienska. In: (2022). General Photo. DOI: `https://cds.cern.ch/record/2800984`.

[68] S. Afanasev et al. "The NA49 large acceptance hadron detector". In: *Nucl.Instrum.Meth.* A430 (1999), pp. 210–244. DOI: `10.1016/S0168-9002(99)00239-9`.

[69] R. Sipos et al. In: *J.Phys.Conf.Ser.* 396 (2012), p. 022045. DOI: `10.1088/1742-6596/396/2/022045`.

[70] B. T. Rumberger. *Hadron Production in 120 GeV/c Proton-Carbon Interactions.* `https://cds.cern.ch/record/2842449`. Presented 13 May 2021. 2021.

[71] A. László et al. In: *Nuclear Instruments and Methods in Physics Research Section A: Accelerators, Spectrometers, Detectors and Associated Equipment* 798 (2015), pp. 1–11. DOI: `https://doi.org/10.1016/j.nima.2015.07.011`.

[72] A. Rybicki and A. D. Marino. Tech. rep. CERN-SPSC-2022-034, SPSC-SR-319. Geneva: CERN, 2022.

[73] . NA61/SHINE Technical Reports. 2020. DOI: `https://edms.cern.ch/document/2422986/1`.

[74] A. Laszlo et al. 2024. arXiv: `2405.01285 [physics.ins-det]`.

[75] D. Tefelski. In: *Acta Phys. Pol. B Proc. Suppl.* 14.3 (2021), pp. 579–582. DOI: 10.5506/APhysPolBSupp.14.579.

[76] A. Aduszkiewicz. Tech. rep. CERN-SPSC-2017-035. SPSC-P-330-ADD-9. CERN, 2017.

[77] M Buénerd and I Efthymiopoulos. https://cds.cern.ch/record/622246. Geneva, 2003.

[78] F James and M Roos. In: *Comput. Phys. Commun.* 10.6 (1975), pp. 343–67. DOI: 10.1016/0010-4655(75)90039-9.

[79] S. Baker and R. D. Cousins. In: *Nuclear Instruments and Methods in Physics Research* 221.2 (1984), pp. 437–442. DOI: 10.1016/0167-5087(84)90016-4.

[80] G. D. Westfall et al. In: *Phys. Rev. C* 19 (4 1979), pp. 1309–1323. DOI: 10.1103/PhysRevC.19.1309.

[81] Y. Nagai. https://indico.cern.ch/event/831594/contributions/3483307/attachments/1877683/3092592/2016data_nagai.pdf. 2019.

[82] Michael Riegel, *private communication*.

[83] P. Ferrando et al. In: *Phys. Rev. C* 37 (4 1988), pp. 1490–1501. DOI: 10.1103/PhysRevC.37.1490.

[84] A. N. Golovchenko et al. In: *Phys. Rev. C* 66 (1 2002), p. 014609. DOI: 10.1103/PhysRevC.66.014609.

[85] W. R. Webber, J. C. Kish, and D. A. Schrier. In: *Phys. Rev. C* 41 (2 1990), pp. 520–532. DOI: 10.1103/PhysRevC.41.520.

[86] I. Schall et al. In: *Nuclear Instruments and Methods in Physics Research Section B: Beam Interactions with Materials and Atoms* 117.3 (1996), pp. 221–234. DOI: 10.1016/0168-583X(96)00325-4.

[87] L. Chulkov et al. In: *Nuclear Physics A* 674.3 (2000), pp. 330–342. DOI: 10.1016/S0375-9474(00)00168-8.

[88] G. Bellettini. In: *Nucl. Phys.* 79 (1966), p. 609. DOI: 10.1016/0029-5582(66)90267-7.

[89] A. Carroll et al. In: *Phys. Lett.* B80 (1979), p. 319. DOI: 10.1016/0370-2693(79)90226-0.

[90] S. Mahajan and R. Raja. In: *arXiv e-prints* (Nov. 2013). DOI: 10.48550/arXiv.1311. 2258.

[91] J.R. Letaw, R. Silerberg, and C.H. Tsao. In: *Astrophys. J. Suppl. Ser.* 51, 271 (1983). DOI: 10.1086/190849.

[92] H.P. Wellisch and D. Axen. In: *Phys. Rev.* C54, 1329 (1996). DOI: 10.1103/PhysRevC. 54.1329.

[93] V.S. Barashenkov and A. Polanski. Tech. rep. JINR-E2-94-417. 1994.

[94] R. Tripathi, F. A. Cucinotta, and J. W. Wilson. In: 117.4 (1996), pp. 347–349. DOI: 10.1016/0168-583X(96)00331-X.

[95] M. Takechi et al. In: *Phys. Rev. C* 79 (6 2009), p. 061601. DOI: 10.1103/PhysRevC.79. 061601.

[96] L. Sihver et al. In: *2010 IEEE Aerospace Conference.* 2010, pp. 1–9. DOI: 10.1109/ AERO.2010.5447011.

[97] L. Sihver et al. In: *Advances in Space Research* 49.4 (2012), pp. 812–819. DOI: https: //doi.org/10.1016/j.asr.2011.11.029.

[98] W. R. Webber, J. C. Kish, and D. A. Schrier. In: *Phys. Rev. C* 41 (2 1990), pp. 566–571. DOI: 10.1103/PhysRevC.41.566.

[99] W. R. Webber et al. In: *Phys. Rev. C* 58 (6 1998), pp. 3539–3552. DOI: 10.1103/ PhysRevC.58.3539.

[100] W. R. Webber et al. In: *The Astrophysical Journal* 508.2 (1998), p. 940. DOI: 10.1086/ 306445.

[101] W. R. Webber et al. In: *The Astrophysical Journal* 508.2 (1998), p. 949. DOI: 10.1086/ 306446.

[102] C. Evoli, R. Aloisio, and P. Blasi. In: *Phys. Rev. D* 99 (10 2019), p. 103023. DOI: 10.1103/PhysRevD.99.103023.

[103] J. B. Cumming, G. Friedlander, and S. Katcoff. In: *Phys. Rev.* 125 (6 1962), pp. 2078– 2081. DOI: 10.1103/PhysRev.125.2078.

[104] A. Korejwo. In: *26th International Cosmic Ray Conference (ICRC26), Volume 4.* Vol. 4. International Cosmic Ray Conference. Jan. 1999, p. 267.

[105]   A Korejwo et al. In: *Journal of Physics G: Nuclear and Particle Physics* 28.6 (2002), p. 1199. DOI: 10.1088/0954-3899/28/6/304.

[106]   D. L. Olson et al. In: *Phys. Rev. C* 28 (4 1983), pp. 1602–1613. DOI: 10.1103/PhysRevC.28.1602.

[107]   W. R. Webber. In: *AIP Conference Proceedings* 2023.1 (1990), 294–298. DOI: 10.1063/1.39166.

A. Appendix

A.1. Interaction of the Beam Upstream of the Target

The various detectors placed on the beamline are always a subject of concern to minimize the material budget before the beam particles interact with the target itself. Beam line detectors placed before the target constitute the upstream region of the experiment, from the scintillator S1 up to BPD-3, and are used for characterizing and studying the properties of the beam. The counting detector S1 is an organic scintillator made from polyvinyl toluene, with a density, $\rho = 1.03\,\text{g/cm}^3$. The scintillator has dimensions $L \times B \times T = 6.0 \times 6.0 \times 0.5\,\text{cm}^3$. Its physical properties are similar to the PE target and has the highest upstream material budget compared to the BPDs and air. The S1 is crucial for defining the trigger logic for online tagging of carbon particles and hence cannot be excluded from the beam line. Therefore, the incoming beam nuclei can interact with S1, which is to say that the upstream survival probability of a beam nucleus 'b', $P^{\text{up}}_{b \to b} \neq 1$. However, since we can measure the mass-changing probability of any nucleus interacting with the PE and C targets, we can utilize these values to compute the interaction probability with S1, or conversely the survival probability of any beam nuclei.

Following the analysis detailed in Sec. 6.2, the mass-changing cross-section ($\sigma^{\text{T}}_{b \to X}$) on a proton target for a nucleus 'b' can be computed. Similar to the case of polyethylene, given that the carbon-to-hydrogen ratio for each polymer cell in vinyl toluene is known to be C : H = 1 : 1.1, the mass-changing cross-section of 'b' interacting with S1 can be computed with the following formula:

$$\sigma^{\text{S1}}_{b \to X} = \sigma^{\text{C}}_{b \to X} + 1.1\sigma^{\text{P}}_{b \to X}. \tag{A.1}$$

In general, the survival probability of the nucleus 'b' for a target T is written as, $P^{\text{T}}_{b \to b} = (1 - P^{\text{T}}_{b \to X})$ and the interaction probability is expressed in terms of the cross-sections

Label	Beam (i)	$\sigma_{i\to X}^{C}$ [mb]	$\sigma_{i\to X}^{p}$ [mb]	$\sigma_{i\to X}^{S1}$ [mb]	$P_{i\to i}^{S1}$	$\frac{P_{i\to i}^{S1}(B)}{P_{i\to i}^{S1}(A)}$
A	^{12}C	746.6 ± 23.4	242.6 ± 21.4	1013.5 ± 33.2	0.976 ± 0.001	
B	^{11}C	635.8 ± 65.2	271.9 ± 60.0	934.9 ± 92.8	0.978 ± 0.002	1.002 ± 0.002
	^{11}B	582.0 ± 211.0	611.3 ± 198.7	1254.5 ± 303.8	0.971 ± 0.007	0.995 ± 0.007
	^{10}B	912.0 ± 152.2	517.0 ± 140.9	1480.7 ± 217.2	0.966 ± 0.005	0.990 ± 0.005

Table A.1.: The mass-changing cross-section of the primary ^{11}C, ^{11}B, and ^{10}B nucleus on the C and p target. The cross-section on S1 is calculated as per Eq. (A.1).

and target parameters as, $P_{b\to X}^{T} = 1 - \exp\left(-d_T n_T \sigma_{b\to X}^{T}\right)$, where d_T is the target thickness and n_T is the number density of the target. For exponent values $y \ll 1$, the expression $f(y) = 1 - \exp(-y) \approx y$. With this approximation, we get $P_{b\to X}^{T} \approx d_T n_T \sigma_{b\to X}^{T}$ implying that $P_{b\to b}^{T} \approx (1 - d_T n_T \sigma_{b\to X}^{T})$. This enables us to re-substitute for the ratio of the upstream survival probabilities of the 'f' and 'b' nuclei in Eq. (6.19).

In the case ^{11}C production, the interaction cross-sections of the primary ^{11}C and ^{12}C are required. Since these nuclei are present in the data, the corresponding in-target mass-changing probabilities are a measured quantity. The computed cross-section values and the corresponding survival probabilities of the two nuclei are given in Tab. A.1. The same technique is applied for the analysis of boron isotopes as well. The last column of Tab. A.1 gives the ratio of the upstream survival probabilities nucleus 'f' $=\{^{11}$C, ^{11}B, ^{10}B$\}$ and 'b' $=^{12}$C, which is very close to 1, hence simplifying the formalism as expressed in Eq. (6.19)

The second term however, is the ratio $\left(\frac{P_{b\to f}^{up}}{P_{b\to b}^{up}}\right)$ containing the probability, $P_{b\to f}^{up}$. It quantifies the fragmentation of the beam nucleus 'b' into nucleus 'f' upon undergoing and interaction in the upstream region. Analogous to the explanation with the upstream survival of a nucleus, we associate the upstream production of 'f' to the interaction b+S1, which can then be calculated by using Eq. (A.1) for the production cross-section of 'f'. Alternatively, to determine the ratio, the quantity $P_{b\to f}^{up}$ can be substituted by the total measured production probability of nucleus 'f' with the PE target, $P_{b\to f}^{PE}$ (calculated and given in Tab. 5.5). Then the ratio term is expressed in terms of known quantities as $P_{b\to f}^{PE}/P_{b\to b}^{S1}$, and is given in Tab. A.2. The denominator corresponds to upstream survival of ^{12}C and is calculated in Tab. A.1.

The ratio of the two quantities is $O(10^{-3})$. Moreover, the two target survival probabilities in Eq. (6.19) are calculated using Eq. (6.4). Their values are of the same order, that is, $P_{f\to f}^{T} \approx$

Fragment (f)	$P^{\text{PE}}_{^{12}\text{C}\to\text{f}}$	$P^{\text{S1}}_{^{12}\text{C}\to^{12}\text{C}}$	$\left(\dfrac{P^{\text{S1}}_{^{12}\text{C}\to\text{f}}}{P^{\text{S1}}_{^{12}\text{C}\to^{12}\text{C}}}\right)^{\dagger}\times 10^{-3}$
^{11}C	0.0060 ± 0.0002		0.0061 ± 0.0002
^{11}B	0.0058 ± 0.0006	0.976 ± 0.001	0.0059 ± 0.0006
^{10}B	0.0036 ± 0.0002		0.0037 ± 0.0002

Table A.2.: The in-target production probability of the ^{11}C, ^{11}B, and ^{10}B nuclei from fragmentation of the ^{12}C. †: The denominator in this ratio is the same as the $P^{\text{S1}}_{\text{i}\to\text{i}}$ for ^{12}C given in Tab. A.1.

$P^{\text{T}}_{\text{b}\to\text{b}}$, for the PE and C targets. Therefore, their difference is $\approx O(10^{-3})$, significantly reducing the total contribution of the second term significantly to $\sim O(10^{-5})$.

A.2. Production of Lighter Fragments

In this section, the impact of the indirect channels in the production of particular light nuclear fragments is investigated. The emphasis is on the production ^{10}C, ^{10}B and the Be and Li isotopes from the interaction of ^{12}C nucleus with the target.

A.2.1. Carbon and Boron Fragments

The production of ^{10}B and ^{10}C from $^{12}\text{C}+\text{T}$ interaction proceeds analogous to the analysis described for ^{11}C and ^{11}B in Sec. 6.4, with additional terms for more than one consecutive interactions, leading to production of the fragment of intereset.

In principle, the upstream interaction probability for the ^{12}C nucleus is finite and $P^{\text{up}}_{^{12}\text{C}\to\text{X}} \neq 0$, thereby leading to production of ^{11}C or a ^{11}B fragments. These fragments can further interact inelastically with the target and convert to lighter fragments like the ^{10}C or the ^{10}B nuclei. To simlify the notations, let the fragmenting ^{12}C nucleus be written as 'b', and the fragment of interest as 'f'. Then the intermediate particles, like ^{11}C are denoted as 'i'. Therefore, the total measured probability when the target is inserted (IN), is written like Eq. (6.12) with additional terms, as follows:

$$P^{\text{IN}}_{\text{b}\to\text{f}} = P^{\text{up}}_{\text{b}\to\text{f}}P^{\text{T}}_{\text{f}\to\text{f}}P^{\text{VD}}_{\text{f}\to\text{f}}P^{\text{dn}}_{\text{f}\to\text{f}} + \sum_{\text{i}} \left(P^{\text{up}}_{\text{b}\to\text{i}}P^{\text{T}}_{\text{i}\to\text{f}}\right) P^{\text{VD}}_{\text{f}\to\text{f}}P^{\text{dn}}_{\text{f}\to\text{f}}$$

$$+P^{\text{up}}_{\text{b}\to\text{b}}P^{\text{T}}_{\text{b}\to\text{f}}P^{\text{VD}}_{\text{f}\to\text{f}}P^{\text{dn}}_{\text{f}\to\text{f}} + P^{\text{up}}_{\text{b}\to\text{b}}P^{\text{T}}_{\text{b}\to\text{b}}P^{\text{VD}}_{\text{b}\to\text{f}}P^{\text{dn}}_{\text{f}\to\text{f}}.$$

(A.2)

The first, third and the last term on the right side of the equation above is exactly the same as those of Eq. (6.12). It denotes the production of 'f' from 'b' in the upstream, in-target and the VD regions respectively. Whereas the second term indicates a sum over the production probability of 'f' inside the target from the intermediate particles i={^{11}C, ^{11}B}.

The second term contains two production probabilities as opposed to the other terms containing just one. However, for a single interaction in the target, say, i→f, the corresponding production probability $P_{i\to f}^{T} \sim \mathcal{O}(10^{-3})$, and is only a fraction of the survival probabilities of 'b' or 'f' given in **??**. Therefore, in any case, the product of production probabilities, $P_{b\to i}^{up} P_{i\to f}^{T}$ in the second term for the two-step reaction is $\sim \mathcal{O}(10^{-6})$. A simple explanation for this is as follows: for any given target, the probability that a nucleus undergoes an interaction i→f is related to the nuclear interaction length as $P_{i\to f} \propto d_T/\lambda$. The typical values of λ for the PE or the C targets are $\sim 20\,\text{cm}$, while the target thickness d_T is approximately 10% of λ. Hence, the interaction probability $P_{i\to f} \ll 1 (\approx 10^{-3})$, or conversely the survival probability (terms with the subscript b→b and f→f) is large. Moreover, in the case of upstream production b→i, the the target is the even thinner S1 scintillator, with thickness $d_{S1} \approx \frac{1}{2} d_T$. Therefore, $P_{b\to i}^{up} < P_{i\to f}^{T}$. The total contribution of the second term amounts to approximately 1% of the other terms, and can be disregarded from the Eq. (6.20). Similarly, the total measured production in the case of the empty target holder (OUT) can be written exactly as Eq. (6.13).

Solving equations Eq. (6.12) and Eq. (6.13) and making the necessary substitutions from auxiliary measurements of primary ^{10}B, we obtain the final expression for the in-target production probability of ^{10}B similar to Eq. (6.19). All the terms are direct measurable quantities, except for the leading ratio of the upstream survival probabilities. It can be estimated using the same method as for the ^{11}C production probability from auxiliary measurements of primary ^{10}B beam. In this case, too it evaluates to ~ 1, simplifying the calculations.

A.2.2. Beryllium and Lithium Fragments

In the case of fragmentation of beam nucleus 'b' to the fragment nucleus 'f', such that $\Delta A = A_b - A_f \geq 2$, for instance, production of beryllium (^{9}Be, ^{7}Be) or lithium fragments (^{7}Li and ^{6}Li) from ^{12}C beam, multiple indirect reaction channels add to the total production of these lighter fragments.

Along the lines of the production of $\Delta A = 1$ fragments described in the Appendix A.2.1, the production of $\Delta A \geq 2$ fragments is eq:527 by two and three-step interactions. Such consecutive processes are quantified by introducing additional terms as given in the second term of Eq. (A.2). Consider the production of nucleus 'f' from 'b' such that $\Delta A = 3$, including all the possible reaction channels. Then, the total measured production probability for the IN case takes the form of Eq. (A.2), with additional terms for the three step interactions, and is written as,

$$
\begin{aligned}
P_{\text{b}\to\text{f}}^{\text{IN}} = {} & P_{\text{b}\to\text{f}}^{\text{up}} P_{\text{f}\to\text{f}}^{\text{T}} P_{\text{f}\to\text{f}}^{\text{VD}} P_{\text{f}\to\text{f}}^{\text{dn}} \\
& + \left(\sum_{\text{i}} \left(P_{\text{b}\to\text{i}}^{\text{up}} P_{\text{i}\to\text{f}}^{\text{T}} \right) P_{\text{f}\to\text{f}}^{\text{VD}} P_{\text{f}\to\text{f}}^{\text{dn}} + \sum_{\text{i}} \left(P_{\text{b}\to\text{i}}^{\text{up}} P_{\text{i}\to\text{j}}^{\text{T}} P_{\text{j}\to\text{f}}^{\text{VD}} \right) P_{\text{f}\to\text{f}}^{\text{dn}} \right) \\
& + P_{\text{b}\to\text{b}}^{\text{up}} P_{\text{b}\to\text{f}}^{\text{T}} P_{\text{f}\to\text{f}}^{\text{VD}} P_{\text{f}\to\text{f}}^{\text{dn}} + P_{\text{b}\to\text{b}}^{\text{up}} P_{\text{b}\to\text{b}}^{\text{T}} P_{\text{b}\to\text{f}}^{\text{VD}} P_{\text{f}\to\text{f}}^{\text{dn}}.
\end{aligned}
\tag{A.3}
$$

Except for the two terms in the bracket, the other terms corresponding to direct production of 'f' in the upstream, in-target and VD regions, are same as these in Eq. (6.12). The bracketed contains the two-step and three-step interactions b→i→j→f leading to production of 'f'. It is eq:527 by the consecutive fragmentation of the intermediate nuclei 'i' and 'j', where $A_{\text{b}} > A_{\text{i}} > A_{\text{j}} > A_{\text{f}}$.

Employing the same reasoning as discussed in Appendix A.2.1, the term with the product of the three production probabilities is a order higher than the two step reaction, and hence is significantly smaller ($\sim O(10^{-9})$). In which case, the final expression for the in-target production of 'f' given in Eq. (6.19) can be used for lighter fragments with $\Delta A \geq 2$.

A.3. Auxillary Measurements of Fragment Production

The number of fragments produced from impurity nuclei ^{14}N, ^{15}N, ^{13}C and ^{11}C are tabulated. These yields are used in to calculate the probability correction factor for the production cross section of ^{11}C, ^{11}B and ^{10}B fragments, as described in Sec. 6.6.2. The uncertainties on the numbers are assumed to be Poisson.

Table A.3.: Number of fragment tracks as measured in the MTPC-L for primary ^{14}N

Dataset	N_{beam}	N_{11B}	N_{10B}	N_{11C}
PE	1607	7	8	6
C	1383	6	6	4
OUT	349	1	1	1

Table A.4.: Same as Tab. A.3 for auxiliary measurement of ^{15}N.

Dataset	N_{beam}	N_{11B}	N_{10B}	N_{10B}
PE	1692	7	9	5
C	1292	4	5	2
OUT	315	1	1	1

Table A.5.: Same as Tab. A.3, for auxiliary measurement from primary ^{13}C.

Dataset	N_{beam}	N_{11B}	N_{10B}	N_{11C}
PE	35810	32	81	130
C	31501	12	60	100
OUT	7953	2	3	3

Table A.6.: Same as Tab. A.3, for auxiliary measurement from primary ^{13}C.

Dataset	N_{beam}	N_{10B}
PE	12300	39
C	10490	21
OUT	2669	6